



Opportunities and challenges in using particle circulation loops for concentrated solar power applications[☆]

Gilles Flamant^a, Benjamin Grange^a, John Wheelodon^b, Frédéric Siros^c, Benoît Valentin^c,
Françoise Bataille^d, Huili Zhang^e, Yimin Deng^{f,g,*}, Jan Baeyens^{b,f,g,*}

^a Processes, Materials and Solar Energy laboratory, PROMES-CNRS, 7 rue du Four solaire, 66120 Font Romeu, France

^b European Powder and Process Technology, Kettering, United Kingdom

^c EDF-R&D Solar Thermal Electric Technologies, Département Mécanique des Fluides, Energies et Environnement, 6, Quai Watier- BP 49. 78401 Chatou cedex France

^d Processes, Materials and Solar Energy laboratory, CNRS-UPVD, Perpignan University, Tecnosud, Rambla de la Thermodynamique, 66100 Perpignan, France

^e Beijing University of Chemical Technology, College of Life Science and Technology, 100029, Beijing China

^f KULeuven, Department of Chemical Engineering, Process and Environmental Technology Lab., J. De Nayerlaan, 2860 Sint-Katelijne-Waver, Belgium

^g Beijing University of Chemical Technology, Beijing Advanced Centre for Soft Matter Science and Engineering, 100029, Beijing, China

ARTICLE INFO

Keywords:

Concentrated solar power
Particle-driven solar receiver
Fluidized bed systems
High efficiency thermodynamic cycles
Particle conveying, process economy

ABSTRACT

Concentrated Solar Power (CSP) is an electricity generation technology that concentrates solar irradiance through heliostats onto a small area, the receiver, where a heat transfer medium, currently a fluid (HTF), is used as heat carrier towards the heat storage and power block. It has been under the spotlight for a decade as one of the potential or promising renewable and sustainable energy technologies.

Using gas/solid suspensions as heat transfer medium in CSP has been advocated for the first time in the 1980's and this novel concept relies on its possible application throughout the full CSP plant, i.e., in heat harvesting, conveying, storage and re-use, where it offers major advantages in comparison with the common heat transfer fluids such as water/steam, thermal fluids or molten salt. Although the particle suspension has a lower heat capacity than molten salts, the particle-driven system can operate without temperature limitation (except for the maximum allowable wall temperature of the receiver tubes), and it can also operate with higher hot-cold temperature gradients. Suspension temperatures of over 800 °C can be tolerated and achieved, with additional high efficiency thermodynamic systems being applicable. The application of high temperature particulate heat carriers moreover expands the possible thermodynamic cycles from Rankine steam cycles to Brayton gas cycles and even to combined electricity generating cycles.

This review paper deals with the development of the particle-driven CSP and assesses both its background fundamentals and its energy efficiency. Among the cited systems, batch and continuous operations with particle conveying loops are discussed. A short summary of relevant particle-related properties, and their use as heat transfer medium is included. Recent pilot plant experiments have demonstrated that a novel bubbling fluidized bed concept, the upflow bubbling fluidized bed (UBFB), recently adapted to use bubble rupture promoters and called dense upflow fluidized bed (DUFEB), offers a considerable potential for use in a solar power tower plant for its excellent heat transfer at moderate to high receiver capacities.

For all CSP applications with particle circulation, a major challenge remains the transfer of hot and colder particles among the different constituents of the CSP system (receiver to storage, power block and return loop to the top of the solar tower). Potential conveying modes are discussed and compared. Whereas in solar heat capture, bubbling fluidized beds, particle falling films, vortex and rotary furnaces, among others, seem appropriate, both moving beds and bubbling fluidized beds are recommended in the heat storage and re-use, and examined in the review.

Common to all CSP applications are the thermodynamic cycles in the power block, where different secondary working fluids can be used to feed the turbines. These thermodynamic cycles are discussed in detail and the current or future most likely selections are presented.

[☆] Flamant G. and Siros F. have equally shared the main scientific tasks, and should be considered as equal primary authors. The overall project coordination was performed by Baeyens J. and Deng Y., considered equal corresponding authors.

* Corresponding authors.

E-mail addresses: yimin.deng@kuleuven.be (Y. Deng), baeyens.j@mail.buct.edu.cn (J. Baeyens).

<https://doi.org/10.1016/j.pecs.2022.101056>

Received 25 April 2021; Received in revised form 2 October 2022; Accepted 29 October 2022

Available online 11 November 2022

0360-1285/© 2022 Elsevier Ltd. All rights reserved.

Since the use of a back up fuel is recommended for all CSP systems, the hybrid operation with the use of alternative fuel back-up is also included in the review.

The review research is concluded by scale-up data and challenges, and provides a preliminary view into the prospects and the overall economy of the system. Market prospects for both novel concentrated solar power are expected to be excellent. Although the research provided lab- and pilot-scale based design methods and equations for the key unit operations of the novel solar power tower CSP concept, there is ample scope for future development of several topics, as finally recommended.

Symbols and Acronyms

A	Cross-sectional area of the containment vessel m^2
Ar	Archimedes number -
D	Diameter of a pipe, m
D_p	Sieve size of particles μm
d_v	Volume equivalent particle diameter μm
D_{sv}	Surface-to-volume diameter of the particle μm
F_p, F_g	Particle mass flow rate and Gas mass flow rate kg/s
G	Solids circulation flux kg/m^2s
G	Gravitational acceleration m/s^2
H	Height m
h, h_{max}	Heat transfer coefficient and maximum heat transfer coefficient W/m^2K
h_{pc}	Convective particle heat transfer coefficient W/m^2K
h_{rad}	Radiation heat transfer coefficient W/m^2K
h_{conv}	Gas convective heat transfer coefficient W/m^2K
LT	Effective length of the fluidized bed, or pipe length m
Nu_{max}	Maximum Nusselt number -
P	Pressure Pa
Re	Reynolds number -
T	Temperature K
T_p, T_w	Bulk (bed) temperature and wall temperature respectively K
T_{cold}, T_{hot}	Cold and hot working fluid in heat exchanger K
T_{db}, T_{wb}	Dry bulb temperature and wet bulb temperature K
U	Superficial air velocity m/s
U_i	Interstitial gas velocity m/s
U_{ms}	Superficial gas velocity at the onset of slugging m/s
U_{mb}, U_{mf}	Minimum bubbling velocity and minimum fluidization velocity m/s
$U_{ch} U_{salt}$	Choking velocity, saltation velocity m/s
U_p	Particle velocity m/s
U_t	Particle terminal velocity m/s
U_{tf}	Gas velocity at the transition to turbulent fluidization m/s
U_{trans}	Transition velocity m/s
U_{TR}	Gas velocity at the transition to circulating fluidization mode m/s
Φ	Wadell's particle sphericity -
M	Gas viscosity Pa s

ε	Bed voidage -
$\varepsilon_s, \varepsilon_{bed}$	Emissivity of the surface and bed, respectively -
λ_g, λ_p	Thermal conductivity of gas and particles, respectively W/mK
ρ_g, ρ_p, ρ_B	Gas, particle and bed bulk density, respectively kg/m^3
σ_B	Stefan-Boltzmann constant, $5.67 \times 10^{-8} W/m^2K^4$

Acronyms

APS	Aiming point strategy
BS	Backup systems
CAPEX, OPEX	Capital expenditures, operating expenses, respectively
CFB	Circulating fluidized bed
CSP	Concentrated solar power
DLR	German aerospace center
DNI	Direct normal irradiation
DUFEB	Dense upflow fluidized bed
EPC	Engineering, management, contingencies, etc.
HEX	Heat exchanger
HRSG	Heat recovery steam generator
HTF	Heat transfer fluid
ISCC	Integrated solar combined cycle plants
LCOE	Levelized cost of electricity
LFR	Linear Fresnel reflectors
ODS	Oxide dispersion strengthened
PDC	Parabolic dish collectors
PHES	Pumped hydro energy storage
PPA	Price purchase agreement
PTC	Parabolic trough collector
PV	Photovoltaic
RC	Recompression
RE	Recuperated
RMCI	Recompression with main compression intercooling
SPT	Solar power tower
TES	Thermal energy storage
TIT/TIP/ CIT/CIP	Turbine/compressor inlet temperature/pressure, respectively
UBFB	Upflow bubbling fluidized bed
WACC	Weighted average cost of capital

1. Outlook and objectives of the review

1.1. The importance of concentrated solar power in renewable energy

In 2021, approximately 290 GW of new renewable electricity capacity were installed [1], with PV accounting for more than half of it. The total global renewable electricity capacity reached 2537 GW by the end of 2019 [2] with hydropower and wind remaining the largest sources of 1310.2 GW and 622.7 GW, respectively. Concentrated Solar Power, CSP, represented ~ 6.5 GW of the total. These statistics indicate that the CSP production capacity is still small with respect to other

renewable production sources. Moreover, PV prices have considerably been reduced in recent years, and CSP technology can no longer compete directly with PV on a simple levelized cost of electricity (LCOE) basis that does not consider the capacity of a given power plant to deliver electricity when most needed. A small capacity nevertheless does not mean a small service to the grid. In favourable regions with direct normal irradiation (DNI) equal to or exceeding about 2000 kWh/m² year [3], the built-in thermal storage capabilities of CSP plants are a decisive asset that distinguishes these plants from highly variable renewable electricity production technologies like PV or wind power. The secure development of interconnected bulk power systems based on renewables needs to respect two functions, adequacy and reliability [4].

Adequacy is the ability of the electricity system to supply the aggregate electrical demand and energy requirements of the customers at all times. Reliability is the probability of the system to perform its function adequately for an intended period and measures the capacity of the considered system to meet all consumer demands. Accounting for these two constraints, system operators are facing a new challenge with the increase of installed capacity of intermittent renewable facilities for power generation. In industrialized countries, the power generation by variable renewable energy together with the base load and flexible generation at minimum load whenever possible, exceeds the demand in specific places at many moments along the year. This leads to a restriction or even curtailment of the operation of renewable plants and to an increase of the costs of ancillary services provided by conventional power plants for balancing the system. In emerging economies, there is often a need to increase generation capacities in all timeframes at a high ramp rate, especially for covering the morning-evening peaks. Therefore, the penetration of variable renewable energy in such systems needs to be backed-up by fossil-fueled plants. Consequently, there is a need to set up new indicators based on the value –not just on the costs – of the new elements of the power system. This will result in specific requirements in terms of a significant share of dispatchable renewables in the overall renewable capacity. The dispatchability is the capacity of a power plant to vary its output at the command of the plant or the system operator. The impact of CSP plants with thermal storage was already discussed in a previous report [5].

For renewable energy supplies, electrical dispatchability refers to the source that can be programmed on demand at the request of the power grid operators, according to market needs. It can hence be expressed by the time of dispatch. Non-dispatchable renewable energy sources such as wind power and photovoltaics cannot be controlled. Several parameters determine the dispatch ability of a power plant, including mostly start-up time, ramp rate, and minimum load capacity. In function of the start-up time, the hierarchy of conventional state-of-the-art plants rates the systems as follows: grid batteries (a few milliseconds) < hydroelectric power plants (seconds to a few minutes) < open-cycle gas turbines (5–10 min) < combined cycle gas turbines (30–40 min). A hard coal fired power plant will require 80 to 150 min as response time. The indicated start-up times or the thermal plants correspond to hot start-ups, i.e., when the plant has been out of operation for less than 8 h. A particle-driven solar power plant with hot storage is expected to have a hot start-up time of around 1 hour, close to that of the state-of-the-art molten salt tower system.

In an example case of California, it was demonstrated that with a 33% share of renewable energy in the power generation mix in the short term, it was economically equivalent to remunerate 5 US cents/kWh to a new PV plant and 10 US cents/kWh to a CSP plant with storage. The value of a new generation unit is based on two components: (i) the operational value that represents the avoided costs of conventional generation at their respective dispatching times along with related ancillary service costs (savings on emission costs are also taken in to account); and (ii) the capacity value that reflects the ability to avoid the costs of building new conventional power plants in response to growing energy demands. In this context, concentrated solar power plants with 7–14 h storage capacity offer the opportunity to install a base-load power generation facility with a capacity factor of approximately 70% and a cost of heat storage in the range 40–50 €/kWh_e (for solar towers), i.e., much cheaper than battery storage. CSP can also be envisioned as a peaker power facility operating only with thermal storage as a complement to PV plants. Such CSP facilities deliver electricity during 5 to 6 h at the end of the afternoon and after sunset when PV production without storage declines to zero [6]. The two strategies are discussed in Section 7 of this paper. Consequently, the annual capacity factor decreases to about 16 to 23% but the electricity cost is only 5% higher than for similarly sized and operated natural gas plants. The conclusion of this study is that a CSP peaker (with 230 MWe net power) can provide most of the capacity and ancillary benefits of a conventional natural gas

peaker plant, however without CO₂ and pollutant emissions.

In assessing the dispatchable energy options, a comparison is difficult since greatly depending on local conditions. It is therefore likely that these specific conditions will alter the competitiveness. Examples, as given below in the Australian context, should not be extrapolated to other regions where local conditions will considerably differ.

A comparison of dispatchable renewable electricity options was prepared by ARENA in the Australian context [7]. The various technologies considered are:

- Utility-scale PV and wind generation in combination with large network connected Li-ion batteries, pumped hydro energy storage (PHES) and hydrogen storage (via electrolyzers).
- CSP with molten salt energy storage.
- Bio-energy via either anaerobic digestion combined with gas engine power generation or biomass-fired boilers with a steam turbine.
- Geothermal generation via either hot sedimentary aquifers or engineered geothermal systems.

The ARENA study shows that there is no single winner, and at each timescale, there are multiple options that fall within a general least-cost band. PV and wind plus batteries are well-adapted solutions for short duration (1–2 h) energy storage whereas PV and wind in combination with PHES can satisfy a wide range of storage hours but is the most sensitive to site constraints. Anaerobic digestion systems operating on zero cost waste and operating at 50% or a higher capacity factor, result in the cheapest dispatchable renewable generating option considered. Combustion-based bioenergy generation is also very competitive at 50% or more capacity factor, provided low-cost biomass inputs can be sourced. Geothermal sources can be competitive for continuous operation. Hydrogen-based storage with PV and wind appears not yet competitive in the time-scale (0–40 h) of the study. Concentrated solar power is competitive for a storage capacity over 6 h and its cost appears to be very similar to that of PV and wind with PHES under this condition (approximately USD 120–130/MWh for 6 h storage and 100MWe, as end of 2017 cost). In particular, there is a minimum in LCOE in the range of 15 to 20 h of storage, even if CSP generation in peak periods may be preferred. This latter finding is in complete agreement with the results of NREL's report [8] concluding that, in 2025, three hours of PV storage tends to produce a lower projected LCOE than CSP. For nine hours of storage, CSP tends to have a lower projected LCOE than PV + batteries. The report demonstrates the significant remaining uncertainty in this kind of cost projection (period 2015–2030). It should moreover be considered that the economic analysis for batteries does not consider the full life-cycle emissions of batteries, which is far from carbon-neutral at present. From an environmental point of view, the CSP versus PV with batteries concepts are environmentally far from equivalent, especially regarding their respective manufacturing processes and Life Cycle considerations. LCA studies on particle-driven CSP applications have not yet been published since still at pilot-scale development. Important facts and data were however published for photovoltaic power plants [9,10] and for battery power storage [9–12].

Previous considerations illustrate the key role of thermal storage in the future deployment of solar thermal power generation. State-of-the-art CSP thermal storage at commercial scale is based on molten salt, a mixture of sodium and potassium nitrates (60/40 wt%) that solidifies at 221 °C and can be used without significant decomposition up to approximately 600 °C. Consequently, it is currently used at a 565 °C bulk temperature. Sensible thermal heat storage is used in parabolic troughs and central receiver (solar towers) CSP plants under different operating conditions. For parabolic troughs (linear concentrating systems) operating at 390 °C with synthetic oil as heat transfer fluid, the temperature difference between hot and cold storage tanks is 90 °C whereas for a central receiver point focusing facility the temperature difference is about three times this value. Consequently, considering the higher conversion efficiency, the storage of one kWh_e needs at least three times

less molten salt in central receiver (solar tower) CSP. Implementing thermal energy storage (TES) in CSP results in an increase of the plant capacity factor with respect to variable renewable energy without storage. The capacity factor is the ratio between what a generation unit is capable of generating at maximum output versus the unit's actual generation output over a period of time. The global weighted average capacity factors for PV, onshore wind and CSP were 18%, 35.6% and 45.2% respectively in 2019 [13]. The same report points out that LCOE of CSP plants fell by 47% between 2010 and 2019 and that a recent auction and price purchase agreement (PPA) indicates a cost in the range of USD 70–80/MWh. This case was analysed in [14]. In particular, for the DEWA IV project in Dubai (700 MWe total, 3×200 MWe parabolic trough plants with 10 h storage and 1×100 MWe solar tower with 15 h storage), a key factor is its extraordinarily long PPA duration (35 years), combined probably with very low financing costs. The weighted average cost of capital (WACC) is estimated to be equal or less than 3% to reach this LCOE. Despite this remark, the authors conclude that low costs are both feasible and sustainable and may be generalized to other places pushing concentrating solar power as a commercially viable technology for dispatchable renewable electricity.

The molten salt working temperature in a central receiver CSP results in a heat-to-electricity efficiency of approximately 42%. Higher efficiencies (~48% and more) are attainable at 650–670 °C with advanced supercritical steam cycles [15], with supercritical carbon dioxide (sCO₂) cycles at 700–750 °C [16], and at approximately 850 °C with hot air turbines operated in externally heated combined cycle gas turbines [17]. Such high operating temperatures result in great challenges on the solar receiver and power plant design, construction materials and heat transfer fluids. In the field, possible options are high-pressure gasses, high temperature molten salt, liquid metals and particle suspensions [18,19]. Accounting for the technical problems linked to high-pressure and high-temperature solar receiver development, critical issues related to corrosion and freezing temperature of high temperature molten salts, and corrosion and safety issues of processes using liquid metals foster, the development of the particle option received a wide interest at the international level.

1.2. CSP technologies and solar towers

Concentrated Solar Power (CSP) is an electricity generation technology that concentrates solar irradiation through concave mirrors onto a small area, the receiver, where a heat transfer fluid (HTF) is used as heat carrier to capture and convey the heat to a heat storage and ultimately a power block. It is particularly promising in regions with high direct normal irradiance (DNI). CSP plants are gaining increasing interest, mostly by using Parabolic Trough Collectors (PTC) and Solar Power Tower (SPT) systems, the latter progressively occupying a significant market position due to their advantages of higher efficiency, lower operating costs and good scale-up potential. The large-scale SPT technology was successfully demonstrated, by e.g., Torresol in the Spanish Gemasolar project on a 19.9 MWe_{el}-scale [20] and at Ivanpah (USA) at a scale of 370 MWe_{el} (3 towers) [21]. According to IEA [22], CSP installed capacity can reach between 9 and 13 GW in 2025 and produce at least 27 TWh.

At present, there are four major CSP technologies: Parabolic Trough Collectors (PTC), Solar Power Towers (SPT), Linear Fresnel Reflectors (LFR) and Parabolic Dish Collectors (PDC). Concentrated Solar Thermoelectrics has also been reported [23], but requires further fundamental and applied research: the cost of thermo-electric materials hampers their widespread use in the CSP concept. The current CSP technologies are of medium (PDC, LFR) to large-scale size (SPT, PTC), with operations mostly located in Spain, Morocco, China, Australia, South Africa, the USA and the Middle East. Parabolic trough collector technology is the most mature CSP design, while the SPT now occupies the second place however with increasing importance because of its advantages and ongoing improvements. A full description of different CSP technologies

is given in [24]. Whereas PTC and SPT can operate at capacities above 100 MWe_{el}, the power of Linear Fresnel Reflector plants are generally in the range 10–50 MWe except the Dhursar plant (India) that reaches 125 MWe [25]. Parabolic dish collector plants operate generally at 10 to 30 kW_e capacity per dish: large scale plants require hundreds to thousands of parabolic dish collector units.

Solar power towers use a field of heliostats, i.e., sun tracking mirrors that reflect and concentrate the sunrays onto a central receiver placed at the top of a fixed tower. In the central receiver, heat is absorbed by a heat transfer fluid, which then transfers its heat to a secondary fluid that powers a thermodynamic cycle turbine. A sensible heat storage is also generally included. Commercial tower plants now in operation use either direct steam generation or mostly molten salts. The concentrating tower can achieve high temperatures, thereby increasing the efficiency at which heat is converted into electricity, and reducing the cost of thermal energy storage. As stated above, the CSP potential can be enhanced by the incorporation of two concepts in order to improve the competitiveness towards conventional power generation systems, i.e., Thermal Energy Storage (TES) and Backup Systems (BS). Both systems offer the possibility of a successful year-round operation, providing a stable energy supply in response to electricity grid demands.

Thermal energy storage systems apply a simple principle: heat collected in the solar receiver is stored by the heat transfer fluid into a hot storage tank. When needed, the hot heat transfer medium can be used and sent to the power block. Storage duration at full power can reach 15 h [20]. CSP plants, with or without storage, are moreover commonly equipped with a fuel backup system (BS), that helps to manage start-up phases, to regulate the production and to guarantee a nearly constant generation capacity, especially in peak periods. CSP plants equipped with backup systems are called hybrid plants. Fossil fuel burners or biomass combustion can provide energy to the heat transfer fluid, to the storage medium, or directly to the power block. The integration of the BS can moreover reduce investments in extra solar field and storage capacity. CSP can also be used in a hybrid mode by adding a small solar field to a fossil fuel or biomass fired power plant. These systems are called Integrated Solar Combined Cycle plants (ISCC), and two case studies were examined by Zhang et al. for the integration with either a coal fired power plant of Southern Croatia [26] or a biomass fired power plant in Lleida (Spain) [27]. Such hybridization targets the reduction of fossil fuel use. A positive aspect of solar fuel savers is their relatively low cost: with the steam cycle and turbine already in place, only components specific to the CSP require additional investment.

The solar power tower concept is flexible as it allows a choice from a wide variety of heliostats, receivers and heat transfer media. Some plants can have several towers (multi-tower concept) to feed a single power block. The next paragraph examines the potential improvements of the solar power tower concept.

1.3. Using particles to raise the operating temperatures of the solar power tower

The main reasons for the enhanced development of novel heat transfer fluids are related to overcoming the specific and overall drawbacks of molten salts, relating to their solidification temperature (~220 °C) and temperature of decomposition of the salts (>600 °C). The use of gas/solid suspensions, i.e., powders, as heat transfer media has been advocated for the first time in the 1980's [28]. Powders have been widely applied in fluidized bed reactors for pyrolysis, gasification or combustion of, e.g., coal, biomass, and plastic and refuse-derived solid waste [29,30]. In such reactors, the powder acts as mixing and isothermal reaction medium, with in-bed or wall-mounted heat exchangers used to generate steam for further use in either a power generation or an in-plant steam network. A novel application of powders in renewable energy relies on their use as heat transfer medium for heat capture, conveying and storage. As explained in Section 3, various particle solar receiver concepts have been developed as a function of the

solid size from few micrometres to millimetres.

The use of gas/solid systems, or powder suspensions, as heat carrier to transfer solar heat from the receiver to the energy conversion process offers major advantages in comparison with water/steam, thermal fluids or molten salts. Since the powder has a heat capacity similar to that of molten salts, without temperature limitation except for the maximum allowable wall temperature of the receiver, a suspension temperature in excess of 1000 °C can be achieved, especially in refractory-lined solar receivers as reported by Rafique et al. [31,32]. These high temperatures offer new opportunities for highly efficient thermodynamic cycles such as obtained when using supercritical steam or CO₂. Moving into higher temperature heat transfer media, a cascade of effects is noteworthy, as illustrated in Fig. 1 and assessed by, e.g., Dunham and Iverson [33].

A higher temperature operation will increase the power cycle efficiency as well as the temperature range over which the storage operates, thus enhancing the thermal energy storage density. The increased efficiency of the power cycle also reduces the thermal power demand from the receiver, which allows a smaller heliostat field to be used and more electricity to be generated per unit of stored thermal energy. The increase in storage density and capacity will reduce investments, despite the use of more expensive construction materials. The increasing technology risk reflects the effects on the other components of the CSP plant, which are more difficult to predict since higher temperatures might increase the cost of the receiver and of the power cycle as well. If the new particle-based high-temperature heat transfer medium is to improve the economics of the CSP, the cost reduction of the solar field and storage must outweigh the cost increases of the receiver and power block.

The higher operating temperature of the powder circulation loop allows advanced power cycle configurations to be used, though not yet exploited in current CSP plants. Typical operating conditions of CSP and fossil fuel power plants [34,35] are shown in Table 1 and Fig. 2, in terms of the operating temperatures and steam pressures, along with typical efficiency values. Parabolic trough collector plants are limited to a steam temperature of 365 °C by their thermal oil heat transfer fluid, and molten salt solar power tower plants are limited to temperatures below 560 °C [36]. Both parabolic trough collector and the molten salt solar power towers operate at temperatures and pressures far below the corresponding state-of-technology fossil fuel power plants, resulting in lower efficiencies. The particle receiver can have a nominal outlet temperature exceeding 850 °C, as discussed in this review paper, thus leading to the potential applications of highly efficient thermodynamic cycles (as detailed in Section 6).

Supercritical Rankine cycles in associated steam turbines are commonly designed for large power outputs (~800 MW_e) [34], and will need to be scaled-down for solar power tower plants by a redesign in order to cope with the low volumetric flow rates and the resulting small blade sizes, although solutions using radial turbines or operating the high pressure turbine at higher speeds have been suggested [39]. State of the art of advanced cycles is proposed in Section 6. In order to facilitate the use of SPT plants in arid locations, the power block must

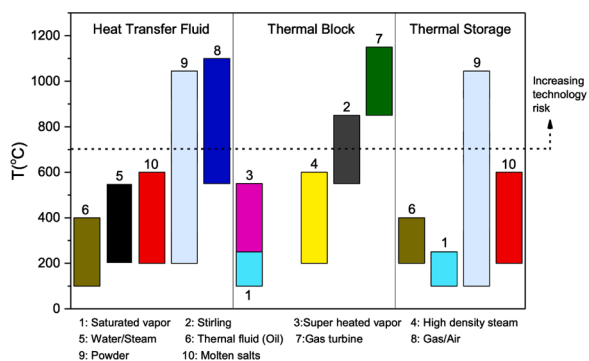


Fig. 1. Operational temperature ranges of different sub-systems.

Table 1

Typical power plant operating conditions reported in [37,38] (The cycle efficiencies cited assume an indirect dry-cooled condenser, operating at 60 °C with multistage feed water preheating).

No.	Power cycle	Steam conditions (°C)	(bar)	Cycle efficiency (%)
1	High-tech. parabolic trough collector plants	375	100	~35
2	High-tech. molten salt solar power tower plants	535	115	~40
3	Old subcritical fossil fuel plants	535	165	~42
4	High-tech. Subcritical fossil fuel plants	565	165	~43
5	Old supercritical fossil fuel plants	565	255	~44
6	High-tech. supercritical fossil fuel plants	600/610	270	~45
7	Advanced supercritical fossil fuel plants	600/620	285	~46
8	Ultra-supercritical fossil fuel plants	700/720	350	~48

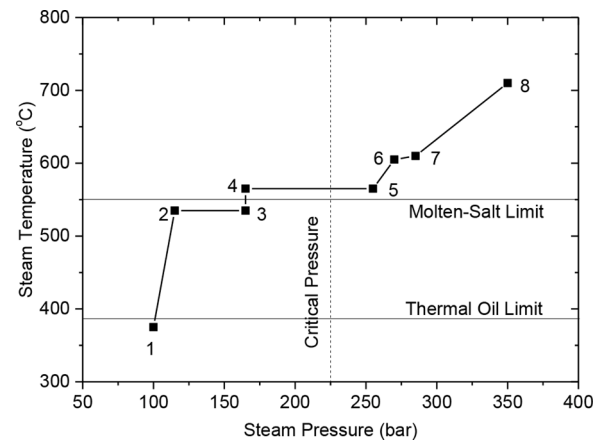


Fig. 2. Evolution of Standard Reheat Rankine-Cycle configurations (numbers refer to Table 1) [37].

use dry, indirect cooling for lack of sufficient cooling water.

1.4. Objectives and layout of the review

In addition to the main concept, particle-driven CSP involves specific components and units that are more commonly used in chemical engineering than in power engineering. Consequently, this paper aims to review the different unit operations where heat transfer to/from the particles is involved both from literature data and from experimental findings.

Section 2 reviews the particle solar receivers tested at various scale, with a focus on the systems with continuous particle circulation. Particle handling issues are detailed in Section 3 since it is a critical point of the technology. Section 4 gives an insight in particle heat exchangers, another originality of the particle-driven CSP concept. A detailed state of the art of existing and advanced thermodynamic cycles is proposed in Section 5. Accounting for the various building units, scaling up procedures, operation in baseload or peaker mode, and hybrid systems are discussed in Sections 6 and 7 respectively. The hybrid systems (bio-energy/CSP) are examined in Section 8. An examination of the required future developments is proposed in Section 9 and the LCOE estimation for a commercial-scale peaker plant is detailed in Section 10 with a reference to current molten salt technology. Section 11 concludes the paper.

Although the scope of the present review paper is limited to the

application of concentrated solar radiation to generate electrical power, recent developments open broader perspectives where the captured heat is directly used in physical processes (e.g., in drying of products [40], in continuous process steam generation [41]), in thermo-chemical processes (e.g., solar biomass pyrolysis or gasification [42]), and even in high temperature calcination of minerals [43,44]. These direct captured solar heat applications have a higher thermal efficiency since avoiding the Carnot losses of the power cycle. These applications are however not dealt with in the present review, but would merit a separate treatment.

2. The particle-driven solar power tower concepts

2.1. Fundamentals of particle technology applied to CSP application

2.1.1. Properties of solid/gas systems

In dealing subsequently with the different solid/gas systems in the CSP concepts, some definitions will be frequently used, and are only briefly summarized below, since available in numerous handbooks on powder or particle technology.

2.1.1.1. Particle size and shape. Three diameter definitions are commonly used for packed and fluidized beds:

- d_p : sieve size, the width of the minimum square aperture through which the particle will pass;
- d_v : volume diameter, the diameter of a sphere having the same volume as the particle;
- d_{sv} : surface/volume diameter, the diameter of a sphere having an equal ratio of surface area to volume ratio as the particle

The last two diameters are related through Wadell's sphericity factor φ [45], resulting in:

$$\varphi = \frac{d_{sv}}{d_v} \quad (1)$$

It has been well established that the most appropriate parameter for correlating the flow of fluids through packed and fluidized beds is the external surface area of the powder per unit particle volume [46], and the most relevant diameter is thus d_{sv} . Unfortunately, there is no simple generally accepted method for measuring the sphericity of small irregular particles. Although values have been published, they should be regarded as estimates only and range from 0.64 to 1 for most materials. Viewing the particles through a microscope will usually enable a realistic value of φ to be determined, according to the method described in Kong et al. [47].

2.1.1.2. Particle density. The density of a specific particle is defined as [46]:

$$\rho_p = \frac{\text{mass of a single particle}}{\text{volume the particle would displace}} \quad (2)$$

The particle density should not be confused with the bulk density of the bed, ρ_B , which takes account of the voids in and between the particles. For nonporous solids the particle density is equal to the absolute density of the material, ρ_{ABS} . For porous solids, $\rho_p < \rho_{ABS}$, and cannot be measured by the usual means and a mercury porosimeter can be used.

For bulk powders, the effect of the gas-filled voids between the particles is accounted for, and $\rho_B = (1-\varepsilon)\rho_p$ with

$$\varepsilon = \frac{\text{total volume of bed} - \text{volume of particles}}{\text{total volume of bed}} \quad (3)$$

2.1.1.3. Dimensionless numbers. The previous fundamental characteristics are commonly grouped within dimensionless numbers, the most representative being:

$$\text{Archimedes number: } Ar = \frac{d_{sv}^3(\rho_p - \rho_g)\rho_g g}{\mu^2}$$

$$\text{Reynolds number: } Re = \frac{d_{sv}\rho_g U}{\mu}$$

Additional dimensionless numbers, namely Nusselt and Prandtl, will be used further in the text and explained as and when required.

2.1.1.4. Packed beds of powders. A widely used characterization of packed beds is the pressure drop. An equation developed by Ergun [48, 49] has been proven satisfactory:

$$\frac{\Delta P}{H} = 150 \frac{(1-\varepsilon)^2}{\varepsilon^2} \frac{\mu U}{d_{sv}^2} + 1.75 \frac{(1-\varepsilon)^2}{\varepsilon^2} \frac{\rho_g U^2}{d_{sv}^2} \quad (4)$$

With ΔP , the packed bed pressure drop per unit height (H) for a gas with viscosity μ and density ρ flowing at a superficial velocity of U through the bed of voidage ε . Under laminar flow conditions ($Re < 1$) the first term on the right hand side dominates, whereas in fully turbulent flow ($Re > 1000$), the second term dominates.

2.1.1.5. Gas velocity. In powder technology, gas velocities are expressed as superficial velocities, i.e., the ratio of the gas flow rate and the cross-sectional area of the containment vessel.

$$U = \frac{F_g (\text{Nm}^3/\text{h})}{A (\text{m}^2)} \quad (5)$$

2.1.1.6. Solid flux and particle velocity. The solid flux is also defined as the mass flow per unit time and per unit cross sectional area of the vessel.

$$G_p = \frac{F_p (\text{kg}/\text{h})}{A (\text{m}^2)} \quad (6)$$

Since $F_p = (1-\varepsilon)\rho_p A U_p$, the solids velocity U_p is equal to

$$U_p = \frac{G_p}{(1-\varepsilon)\rho_p} \quad (7)$$

2.1.1.7. Transition velocities. Since different hydrodynamic regimes occur in gas/solid systems, regime-transition velocities will be used, for example, the minimum fluidization velocity, U_{mf} ; the minimum bubbling velocity, U_{mb} ; the particle terminal velocity, U_t ; the velocity at the onset of turbulent fluidization, $U_{t\tau}$; or at fast fluidization, U_{TR} . These velocities will be determined and quantified in Section 2.2.2.

2.1.1.8. The powder classification. Work by Geldart [50] and by Baeyens and Geldart [51] summarized the experimental and industrial experience of using different powders. A powder classification was established based upon increasing cohesiveness (C-type), aeratability (A-type), bubbling fluidization (B-type) and specific behavior of coarse powders (D-type). The main properties of the 4 groups are specified by Geldart [50].

Geldart [50] presented a tentative diagram for classifying the powders into groups having broadly similar fluidization characteristics in ambient air. The group boundaries were further refined and completed by, e.g., Wu and Baeyens [52], Rabinovich et al. [53] and Kong et al. [47]. Cohesive C-type particles are not recommended for use in particle systems.

2.1.2. Solid/Gas systems: from packed bed to pneumatic conveying

2.1.2.1. The gross behavior of solid/gas systems. The processes of heat or mass transfer and chemical reaction in fluidized beds depend on the interaction of gas and solids within the bed. Different contacting regimes are possible, depending on the solid/gas characteristics, the bed geometry and the operating gas flow rate. The transitions are presented in Fig. 3.

When a gas passes upwards through a bed of particles, it percolates through the void spaces, and at low gas flow rates the bed remains

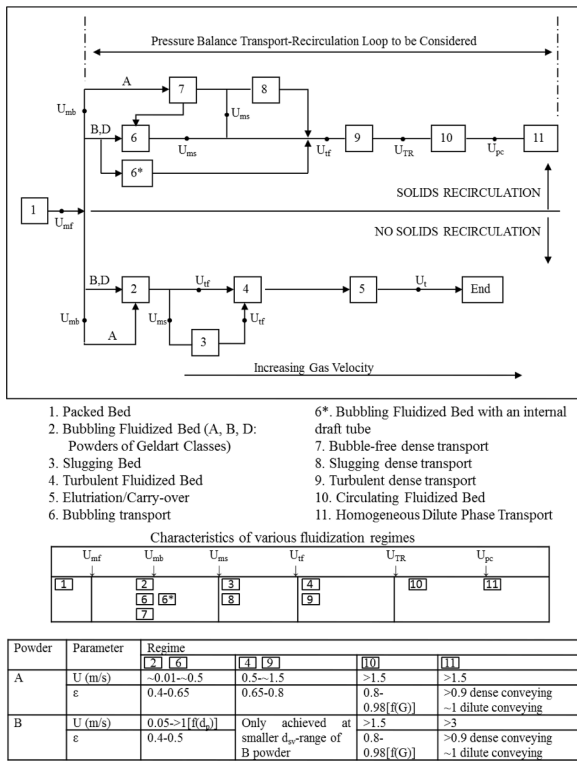


Fig. 3. Operation modes of solid/gas systems.

packed. The increase in pressure drop is proportional to the gas flow rate in the laminar flow mode (Eq. 3). When the pressure drop approaches the weight of the bed per unit cross-sectional area, the particles start to move slightly without losing mutual contact, but in such a way that the gas is given a maximum passage. A further increase in gas flow rate will lead to the state in which the drag force between the particles and the gas counter-balances the weight of the particles and the bed is considered to be incipiently fluidized. The superficial gas flow rate at this point is called the minimum fluidization velocity, U_{mf} .

For most solid/gas systems, an increase in flow rate beyond U_{mf} results in bubbling. No increase in pressure drop is observed since the excess gas by-passes the dense phase as bubbles. For A-type powders however, this increase in gas flow rate results in a progressive expansion of the bed and bubbling only starts at a higher velocity, called the minimum bubbling velocity, U_{mb} . In cohesive powders, channeling of the gas is often observed. If the superficial gas velocity gradually increases above U_{mf} or U_{mb} , bubbles form and rise upwards through the bed growing in size as they do so. As the velocity increases further, the average bubble size increases and may reach a size comparable with the diameter of the bed: the bed is said to be slugging and the superficial gas velocity at the onset of slugging is called minimum slugging velocity, U_{ms} . The commencement of slugging is dependent primarily upon the bed diameter and $U-U_{mf}$, called the excess gas velocity. Slugging should be avoided.

At sufficiently high gas flow rates, the terminal velocity of the particles, U_t , is exceeded and solids are carried out of the bed with the gas stream. For the sake of completeness, a variant of fluidization namely the spouted bed technique is mentioned. It is often used for coarse materials. Gas is introduced into the bed by a single central nozzle and the formed jet penetrates through the full depth of the bed. At very high gas flow rates, pneumatic conveying will occur: U_{pc} is the onset velocity of pneumatic conveying.

2.1.2.2. Characteristics and transition velocities. The dominant parameter in fluidization is the superficial gas velocity. In circulating fluidized

beds (CFBs) and pneumatic conveyors, the solids loading in general and solids circulation rate in the CFB are also important [54,55].

The different operation modes of powder gas systems have been discussed by previous researchers [50,56], and can be distinguished with operating velocities at the transition of subsequent operation regimes, U_{trans} , using selected empirical equations listed in Table 2. For circulating fluidized bed and pneumatic conveying applications, additional critical velocities are the choking velocity (U_{ch}) for vertical transport, and the saltation velocity (U_{salt}) for horizontal pneumatic transport. Both circulating fluidized bed and dilute-phase pneumatic conveying (solid/gas mass flow ratio below 10 kg/kg) are not recommended for CSP receiver applications due to the low solid fraction of the upflowing suspension, and the high volumetric gas flow rate required (leading to excessive sensible heat losses).

However, for the particle conveying within the CSP loop, the dense-phase pneumatic conveying, operated at high solid/gas mass flow ratios of 100 to 250 kg/kg, is deemed applicable and merits further investigation due to its flexibility, non-mechanical nature and expected economics. This is dealt with in Section 3.

2.1.2.3. Bubbling and slugging regimes. In a bubbling fluidized bed, small bubbles are formed at the distributor and grow when rising through the bed. Their rising velocity is a function of the bubble diameter. In beds of Geldart-A type particles, a stable maximum bubble size can be reached. In beds of coarser particles, bubbles keep on growing. The fluidization regime starts to alter when the bubbles grow larger than approximately 50 % of the bed diameter and when the wall effect influences the bubble and solids flow. The rise velocity of the bubbles, now called slugs, is determined by the bed diameter. Slugging beds are characterized by large pressure fluctuations [56]. According to Yagi et al. [60], slugging is unlikely for low values of the height/diameter ratio.

2.1.3. Heat transfer in gas-fluidized beds

2.1.3.1. General considerations. Heat transfer is generally very favorable in bubbling fluidized beds, representing one of the key advantages of fluidization. Some extended reviews of heat transfer are presented by Gutfinger and Abauf [61], Botterill [62], Saxena et al. [63], Grace [64], Baeyens and Geldart [65], and Xavier et al. [66].

For most practical purposes, a gas fluidized bed may be macroscopically regarded as isothermal [84,85]. In general, thermal equilibrium is achieved within about 25 mm of the bottom of a fluidized bed. For high velocity jets entering a bed through a perforated plate or nozzles, a greater distance may be required.

The heat transfer coefficient for bed to wall heat transfer is normally very high, of the order of 500 - 1000 W/m²K, roughly one order of magnitude higher than that for steady state transfer to the wall in a packed bed, and two orders of magnitude better than gas to wall transfer in an empty column under comparable flow conditions. The overall heat transfer coefficient between the bed and a wall, h , is made up three components [65-67]:

$$h = h_{pc} + h_{conv} + h_{rad} \tag{8}$$

Table 2 Prediction of transition velocities.

U_{trans}	Equations	Ref.
U_{mb}	$U_{mb} = \frac{2.07 d_p \rho_g^{0.06}}{\mu^{0.347}} \exp(0.716 F_{45})$ F_{45} : fine fraction less than 45 μm	Abrahamsen and Geldart [57]
U_{mf}	$Ar = 1823 Re_{mf}^{1.07} + 21.27 Re_{mf}^2$	Wu and Baeyens [52]
U_{if}	$Re_{if} = 0.36 Ar^{0.59}$ for $2 < Ar < 10^8$	Deng et al. [58]
U_{TR}	$Re_{TR} = 3.23 + 0.23 Ar$	Zhang et al. [59]
U_{ms}	$U_{ms} = U_{mf} + 0.07 \sqrt{gD}$ D: diameter of the bubbling fluidized bed	Baeyens and Geldart [56]

The particle convection term, h_{pc} , is that arising from unsteady state conduction through a gas film and particles during the time that particles are contacting the wall. Some workers [64,65,68,69] call this the particle convective transfer since the time-averaged value relies on frequent particle replacement, i.e., on convection by the particles to the bulk of the bed after the transfer has taken place by unsteady state conduction. The h_{conv} term is called the “gas convective” component. For modest bed temperatures (e.g., less than about 1000 °C) the particle convective component dominates for small particles while the convective component h_{conv} is rate-controlling for large particles where the interstitial gas velocity is significant. The radiation component h_{rad} becomes important at high temperature.

It is a common simplification to assume that the three components can be predicted separately and then simply added. This procedure should, however, be used with caution when two or more of the components are of comparable magnitude.

2.1.3.2. Particle convective component, h_{pc} . The favorable heat transfer coefficient between fixed surfaces and fluidized beds of fine particles results from high values of h_{pc} . Favorable time-averaged values of h_{pc} are associated with frequent exposure of fresh particles from the bulk to the heat transfer surface.

Gas convective component, h_{conv} .

In addition to heat transferred due to conduction through stagnant gas, transfer also occurs due to mixing of gas percolating along the surface in the interstitial voids between the particles. Baskakov et al. [70] correlated this component by means of

$$Nu = \frac{h_{conv}d_p}{\lambda_g} = 0.009Ar^{0.5}Pr^{0.33} \quad (9)$$

Alternatively, Denloye and Botterill [68] obtained values over an experimental range of operating conditions up to 10 bar:

$$\frac{h_{conv}(d_p)^{0.5}}{\lambda_g} = 0.86Ar^{0.39}(10^3 < Ar < 10^6) \quad (10)$$

2.1.3.3. Radiation component, h_{rad} . Radiation heat transfer from fluidized beds is simplest for large particles since their temperature does not vary appreciably during exposure to a hot or cold surface. Therefore, radiation can be predicted from the net flux between two isothermal planes. Since the bubbles can be considered transparent, no allowance needs to be made for the fraction of time during which bubbles are at the surface. Representing both wall and particle surface as gray bodies, the Stefan-Boltzmann equation can be used:

$$h_{rad} = \frac{\sigma_B(T_W^4 - T_p^4)}{\left(\frac{1}{\epsilon_s} + \frac{1}{\epsilon_{bed}} - 1\right)(T_W - T_p)} \quad (11)$$

σ_B is Stefan-Boltzmann constant and it equals $5.67 \times 10^{-8} \text{ W/m}^2\text{K}^4$

The effective bed emissivity, ϵ_{bed} exceeds the particle emissivity, ϵ_s , due to multiple reflections.

For small particles, the description of radiation heat transfer is more complex since it must consider the bed as a semi-transparent medium in order to account for radiation penetration in the particle packet [71].

Gutfinger and Aubauf [61] tabulate no fewer than 34 different correlations, and others have been added since their review was prepared. The predictions of different correlations commonly disagree widely due to different fluidized bed dimensions, bed materials, operating conditions and hydrodynamic regimes. It is important not to apply these correlations outside the ranges for which they were derived. Separate correlations are available for transfer to the external wall, to vertical tubes and to horizontal tubes. Some correlations seek to give the effect of superficial gas velocity, whereas others are for the maximum heat transfer coefficient. The correlations presented do not include the effect of radiation. Where radiation is important, it should be added on as outlined before. The accuracy of the correlations shall not be assumed to

be better than $\pm 30 \%$ within their ranges of application. Large discrepancies must be expected when the correlations are extrapolated to other conditions.

2.1.3.4. Maximum particle convection heat transfer coefficient, h_{max} . Many investigators have reported data in the region of h_{max} for heat transfer from an immersed surface to the bed or presented correlations to predict this maximum value. Similar data for heat transfer at the outside wall have been presented, generally about 30% lower than h_{max} for immersed surfaces. Most experimental results have been taken only in small size units (< 15 cm on I.D.).

Obviously most practical applications of the fluidized system will be in the region of h_{max} and a prediction of both the maximum achievable heat transfer coefficient and the corresponding gas flow rate is very valuable for process optimization as it provides a standard of excellence.

A number of correlations have been given for the maximum heat transfer coefficient achieved when U is varied over a wide range. The correlation of Zabrodsky et al. [72] covers a relatively broad range of data including beds operated at high temperature:

$$Nu_{max} = \frac{h_{max}d_p}{\lambda_g} = 0.88Ar^{0.213}(10^2 < Ar < 1.4 \times 10^5) \quad (12)$$

This equation may be applied for vertical or horizontal tubes and for particles smaller than about 1 mm.

A similar approach was adopted by Baeyens and Geldart [65] with

$$Nu_{max} = 0.91Ar^{0.21} \quad (13)$$

If by analogy with other existing correlations, gas properties are included as Pr number ($Pr^{0.33}$), and Eq. (13) is modified to

$$Nu_{max} = 1.02Ar^{0.21}Pr^{0.33} \quad (14)$$

2.1.3.16. Finned tubes. Improved heat transfer rates on a bare tube basis can be obtained with an extended finned heat transfer area. In addition, the extra confining impact of the fins may locally reduce the velocity of solid suspension, thus reducing the erosion of the tubes. Various types of fins have been tried. Hager and Thomson [73] showed that fins have little effect on hydrodynamics for vertical tubes, but play an important role for horizontal and inclined tubes. The de-fluidized region above tubes with radial fins tends to be larger than for bare tubes. The region between transverse fins tends to be de-fluidized. There is less tendency for bubbles to adhere to finned than to bare tubes, while bubbles distort more as they pass finned tubes.

Rates of heat transfer increase as fins are added to bare tubes [74–79] but the increase levels off as the fin height is increased. The fins are much less effective if particles are unable to circulate freely between them. A deterioration in heat transfer coefficient due to this effect was noted for d_p greater than about 0.1 x fin spacing [76].

While correlations have been proposed for heat transfer from finned tubes, the range of experimental conditions covered is too narrow for reliable predictions to be expected under different conditions. The best procedure, if pilot plant data are unavailable, would appear to be to use bare tube correlations and to apply correction factors to allow for the presence of fins, using the cited studies to suggest the degree of augmentation likely for a given configuration and tube material.

In the review by Baeyens and Geldart [65], the emission packets renewal model approach with contact resistance represents the bubbling bed situation very accurately. It is now widely used and was applied by Zhang et al. [80] for the Upflow Bubbling Fluidized bed receiver.

2.1.4. Novel bubbling regime: vertical upflow systems

Literature concerning dense up-flow systems, with forced up-flow and bubble induced mixing is scarce. Initial research mostly covered moving packed beds [81–83] hence with a gravity down flow of particles. Fluidized bed up-flow reactors were described by several researchers, as reviewed in Supplementary information. The dense

up-flow column is fed at its bottom by a circulation flow of solids at an appropriate pressure to overcome the pressure drop of the upwards-moving bed of solids. The column itself is either aerated from the windbox [84–89] or by a combined windbox aeration and additional aeration at the bottom of the riser column itself. Illustration of the experimental rigs used in these earlier works were presented in Zhang et al [80]. All rigs have an upflow section, and a pressurized feeder.

Table 3 compares the essential earlier literature findings. Except for Tomita et al. [90], all investigations used column diameters $D < 0.1$ m. Transport heights, L_T , vary from 2.0 to 24.0 m [90], and the upflow is either lean with a very low solids fraction α_p or a real fluidized bed operation with solids fraction between 0.25 and 0.4. In circulating fluidized bed operations, the solids fraction is close to 0.02–0.05.

2.2. Survey of the current particle-driven solar receivers

Particle solar receivers can be classified according to the following characteristics,

- Direct or indirect heating of the particles
- Continuous particle flow or batch process
- Types of solid-gas contacting and mixing modes

In addition, inert or reactive particles may be added to the previous list since many developments have been achieved in the field of solar thermo-chemistry for solid-gas reaction processing. Applications in solar thermo-chemistry address calcination, thermo-chemical energy storage, gasification and hydrogen production using redox cycles [94–96]. Most of the thermo-chemical particle reactors apply the direct particle irradiation configuration to reach high temperatures [97].

The type of solid-gas contacting and mixing modes refer to particle reactors in chemical engineering. They are moving beds, falling particles, vortex and centrifugal particle flows, and fluidized beds. A review on gas-solid fluidized bed solar receivers was published recently, it includes consideration on particles properties, receiver developments, measurement methods and modeling tools [98].

2.2.1. Particle-driven solar receivers without particle circulation

The first development of batch fluidized bed solar receivers-reactors dated from the eighties [98]. Fluidized particles were heated from the top of the bed using a beam-down concentrating system, a solar furnace in the previous study. The concept was then developed particularly in Italy and Japan using solar simulators and beam-down solar concentrators. Tregambi et al. [99] studied a directly-irradiated fluidized bed of 127 μm Sauter diameter silicon carbide particles heated by a short-arc Xe lamp coupled with an elliptical reflector. They examined in particular the interaction of bubbles with the radiation beam. The design was then improved using a compartmented windbox, without physical partitioning or internals immersed in the bed [100]. Physically compartmented design was also examined for energy storage applications [101]. The integration of the particle receiver in a calcium looping CSP plant was further proposed [102]. Recently, the same team designed an autothermal solar fluidized bed integrating a double pipe heat exchanger [103] that was proposed to be used for operating a thermo-chemical battery using the limestone calcination/carbonation reversible reaction [103]. Nevertheless, continuous particle flow and pilot-scale receiver were never experimented. Magaldi Company developed the fluidized bed particle receiver heated by a beam down solar concentrating system at prototype scale to produce steam under the name Solar Thermo Electric Magaldi (STEM®) [104]. A 2 MW_{th} plant was installed in Sicily, Fig. 4. The 2 MW_{th} Solar Thermo Electric Magaldi (STEM®) prototype using a fluidized bed solar receiver for steam production.

Previous developments are related to the windowless concept that is not adapted to syngas production based on solid-gas reaction. Kodoma et al. [105] developed a spouted bed-type design equipped with a window for particle processing. The concept was experimented for

driving a two-step water splitting reaction based on NiFe₂O₄ is bed heated by 6 kW Xe-arc lamp [106] and coal gasification [107]. Then a 30 kW_{th} fluidized bed reactor was installed and fabricated at Niigata University, and modeled [108]. Maintaining the batch operation mode, the system was scaled up to 100 kW_{th} and heated by a beam-down solar concentrator [109]. The core fluidized bed temperature of the sand particles attained 1100 °C during experiments.

Fluidized SiC particles of different size (from 0.5 to 2 mm) was used in [110] to heat air inside a 34 mm ID quartz tube. The highest air temperature was measured at 867 °C with 0.5 mm particles.

2.2.2. Particle-driven solar receivers with particle circulation

The following analysis considers separately lab-scale and prototype or demonstration-scale developments.

At lab-scale. Continuous-fed particle receiver-reactor concepts have been tested at lab-scale mainly for solar thermo-chemical applications. Concerning direct absorption systems, they are the vortex flow reactor developed for steam gasification of petcoke [111], the cascading pressure reactor for solar reduction of oxides [112], the spouted bed for continuous steam gasification of biomass [110], and the rotary kiln for calcination [113]. Indirect absorption particle solar reactors have also been developed, for example, the particle flow reactor for biochar gasification [114] and the pressurized adaptation of the vortex flow reactor [115]. Lime production at pilot scale was also demonstrated in a 10 kW_{th} multitube rotary kiln [116] and in a 50 kW_{th} horizontal multi-stage fluidized bed [117]. This latter study can be considered as a prototype-scale demonstration of solar calcination.

The small particle solar receiver concept was proposed in [118] and modeled in [119]. It consisted in a realizing a suspension of sub-micron carbon particles in a gas thus creating a volumetric absorption with negligible scattering. The gas could be inert or reactive. Receiver efficiency in the range 80–90% was predicted. Experimental validation was published in [120] with a mass fraction of particles in the range 0.2–0.5 wt%. Gas temperature varied from 1900 to 2100 K depending of the carrier gas. The integration of the solar receiver with a gas turbine and the associated efficiency was then published in [121].

Various concepts of directly irradiated moving bed particle solar receivers have been published. Xiao et al. proposed the spiral design [122,123]. 300–600 μm sintered bauxite particles were tested with a solar simulator (5 kW). Temperature increases up to 350 °C were measured and the thermal efficiency reached approximately 60%. Inclined moving bed was studied in [124]. A fluidizing gas assisted the particle movement. Experimental result indicated a mean particle temperature of approximately 807 K and a receiver efficiency of 61% for 7.5 g/s particle mass flow rate. Moving bed in quartz tube concept was examined in [125–128]. Helix quartz tube solar receiver was tested in [125]. For a particle mass flow rate of 8.12 g/s the particle temperature increased by 212 °C (0.2 m irradiated length) and the measured maximum thermal efficiency was 61.2%. Study [126] reported cold test of particle flow in vertical tubes with particle sizes ranging from 149 μm to 1359 μm (mean diameter) with and without insert in single and multi-tube systems. Solar simulator test results were examined in [127]. A temperature increase of 164 °C was measured with 718 μm particles for a mean radiative power density of 276 kW/m² on a 0.26 m irradiated length. The corresponding thermal efficiency was 50%. Nie et al. [128] experimented and modeled the particle flow characteristics in tubes equipped without and with an insert delimiting an annular irradiated section. They recommended using an insert and a layer thickness of 5 mm to obtain a homogeneous axial particle velocity.

At prototype scale. Solar power production based on the particle technology involves critical constraints such as receiver scalability at multi-MW scale, handling of continuous flows of large amounts of particles, hot particle storage and particle-to-working fluid heat exchanger design. The concept of a particle solar receiver and storage integrated with a combined cycle was published in [129].

Three main solar receiver concepts are presently under development

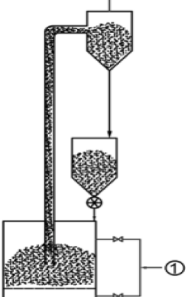
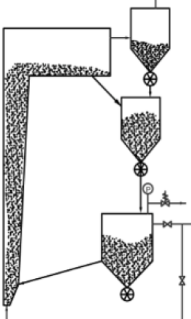
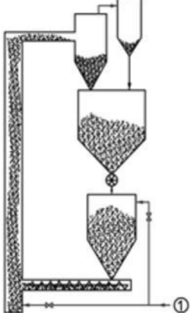
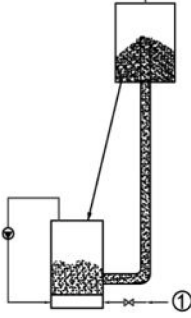
at prototype and demonstration scales worldwide, the free falling or obstructed particle receiver, the centrifugal receiver and the multi-tube fluidized bed [130]. Both first types are direct particle heating concepts and the latter is an indirect heating design.

Sandia National Laboratories (SNL) developed the free falling particle central receiver concept in the early eighties [131]. The particle curtain is directly heated by concentrated solar energy in a cavity. In this configuration, the main operation parameters are the particle size, the particle cloud absorptance and optical thickness, and the mean residence time of the solid in the irradiated zone [132]. The concept was then analyzed in the perspective of large-scale applications at high temperature [133]. After a period of reduced activity in the field, SNL

started again to develop the technology in the framework of the US-DoE SunShot initiative. Receivers for commercial-scale solar power plants (100 MWe) were designed [134]. Simulations indicated that a 256 MW_{th} receiver with a 10.63×10.63 m aperture and 50° nod angle can reach a thermal efficiency in the range 80–86.8% when delivering particles at approximately 750 °C. The receiver was assumed to be located on a 195 m height tower. Mills [135] simulated the thermal efficiency of an intermediate scale 135 MW_{th} peak falling particle solar receiver heating particles in the range 750–775 °C. The 700 μm particle curtain length was 14 m. The thermal efficiency was found between 83 and 86.8% with an annualized value of 85.7%. An important issue of the falling particle solar receiver is the particle flow behavior. This issue was addressed in

Table 3

Literature review of dense particle upflow systems.

Reference	Illustrations	Powder	d_p (μm)	ρ_p (kg/m ³)	D (m)	L_T (m)	α_p (-)	F_g (kg/s)	F_p/F_g (-)	$\Delta P/H$ (mbar/m)
Tomita et al. [90]		cement	30	2560	0.41 0.668	24.0	0.09–0.18 0.08–0.14	0.023–0.06 0.062–0.135	101.5–228.7 99.6–131.5	53.8–115.8
Li and Kwaak [83]		resin coal	65 1000	1188 929	0.047 0.047	8.0	0.66 0.62	0.00044–0.00076 0.0012–0.0016	17.1–25.0 7.5–9.2	125–188 170–225
Zhu and Zhu [85]		FCC-catalyst	65	1780	0.101	3.6	0.24–0.29	0.016–0.032	25.0–37.5	45–55
Watson et al. [86]		alumina	2690	3500	0.0464 0.0714	3 4	0.22–0.5 0.33–0.61	0.0104–0.0239 0.0103–0.0444	19.2–732.2 71.8–202.7	78.3–167 148.5–200

(continued on next page)

Table 3 (continued)

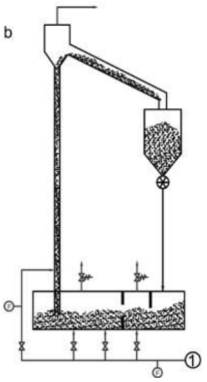
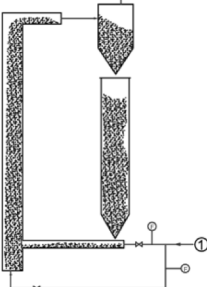
Reference	Illustrations	Powder	d_p (μm)	ρ_p (kg/m^3)	D (m)	L_T (m)	α_p (-)	F_g (kg/s)	F_p/F_g (-)	$\Delta P/H$ (mbar/m)	
Turzo [88]		alumina	54	2360	0.028	6.0	0.31–0.41	0.00005–0.00058	100.0–741.4	80	
Flamant et al. [87, 91]		SiC	64	3120	0.036	2.0	0.26–0.35	0.00013–0.00057	1039–4077	88	
Hirama et al. [84]		HA54	38	750	0.10	5.5	0.003–0.25	0.011–0.053	1.7–4.8	2–180	
		FCC-catalyst	57	930	0.10			0.006–0.17	0.031–0.041	1.4–15.2	5–150
Pitić et al. [92]		sand	75	2260	0.05	2.5	0.01–0.03	0.16–0.79	34–838	3.5–5	
Zhang et al. [93]		sand, bituminous coal	74–79	2160–2340	0.05	2.5	0.01–0.03	0.04–0.32	8.5–9.4	2.1–2.3	



Fig. 4. The 2 MW_{th} Solar Thermo Electric Magaldi (STEM®) prototype using a fluidized bed solar receiver for steam production.

Ho [136] and Kim [137]. Ho [136] characterized the free-falling flow of CARBO Accucast (75% Al₂O₃, 11% SiO₂, 9% Fe₂O₃, 3% TiO₂) 280 μm particles experimentally and numerically. Particle mass flow rate in the range 3–9 kg/s.m (with respect to curtain width) have been tested. The particle velocity 1 m after the release point was approximately 5 m/s and the curtain thickness doubled at the same point. The particle volume fraction decreased from 60% to less than 10% after a 0.5 m trajectory from the release point that resulted in an increase of the curtain transmittance. The wind effect on the particle flow stability was examined in Kim [137]. The experimental results obtained with 697 μm CARBO HSP (83% alumina) particles indicated that critical loss of particles might result from winds with certain angles of the attack. For a 45° angle of attack, a less than 0.46 m of the cavity depth, and a 6.5 m/s wind velocity, up to ~10% particle loss occurred. Contrarily, wind with 90° angle of attack resulted in a particle loss less than 2% and the closer to the back wall the lower the particle curtain loss due to wind. On-sun test

results are reported in Siegel [138] and Ho [139,140]. Siegel [138] published experimental results obtained with a 6 m tall cavity receiver equipped with a 3 m high and 1.5 m width aperture operating in the power range 1.6–2.5 MW_{th} using the 5 MW_{th} SNL solar tower facility in Albuquerque. CARBO HSP with 697 μm mean diameter particle were introduced in a 1.5 m in depth cavity. Runs duration lasted from 3 to 7 min depending on the mass flow rate. The measured particle temperature increase was ranging from 100 to 250 °C as a function of incident solar power at the cavity aperture and particle mass flow rate, in agreement with simulation data. Maximum receiver thermal efficiency was 50% with dominant radiation losses with respect to convection. This result can be explained by the low value of the average solar flux density on the particle curtain, 400 kW/m². Excessive heating of the receiver back wall was noticed due to the decrease of particle volume fraction from the top to the bottom of the particle curtain that resulted in an increase of its transmittance. Ho [139] reported the test result of a 1 MW_{th} falling particle receiver carried out with the same solar facility. The receiver consisted of 2m×2m×2m cavity with a ~1mx1m aperture. CARBO Accucast particles with 280 μm mean diameter were used. Free-fall and obstructed-flow particle receiver design have been tested. The obstructed flow design consisted in using chevron-shaped mesh structures in order to increase the residence time of the particle in the solar irradiated zone. Consequently, the residence time of the particles in the irradiated zone was approximately 0.2–0.4 s for the free-falling receiver and 1–3 s for the obstructed-flow receiver. The particle can be recirculated thanks to an Olds' elevator. A temperature increase of approximately 200 °C/m drop was measured with the obstructed-flow receiver for a solar flux density of 400 kW/m². The bulk outlet temperature exceeded 700 °C for several tests. The temperature increase reduced to 100–150 °C/m drop for a solar flux density of 600 kW/m² and 2–3 kg/s.m (curtain width) particle mass flow rate. The thermal efficiency ranged from 50 to 90% and 40–80% for the obstructed-flow and free-fall receivers respectively. Technical issues were observed with variable particle mass flow rate and deterioration of the chevron structure of the obstructed-flow receiver. Further tests were performed with a closed-loop feedback system aiming to maintain the particle

outlet temperature by varying the mass flow rate [140]. The experimental system is illustrated in Fig. 5.

During the tests, the particle set point temperature varied from 350 to 650 °C. The control system proved to work well during high temperature runs. Nevertheless, oscillations have been observed in rapid irradiation variation conditions. The receiver thermal efficiency ranged from 50% to 90%.

The German Aerospace Center (DLR) developed the centrifugal particle receiver concept (CentRec). Proof of concept was performed using the DLR 10 kW solar simulator [141]. The CentRec receiver is a rotary cylinder that can be inclined 90° to the horizontal. The feed particles form a thin layer at the wall due to the centrifugal acceleration. The additional action of gravitation results in a slow movement of the particle in the axial direction from the bottom to the cylinder aperture. During their trajectories, they are heated by the concentrated radiation focused at the aperture. Sintered 1 mm diameter bauxite particles were used during the high temperature tests of the lab-scale receiver oriented vertically (90°) or at 45°. The 137 mm ID aperture received a maximum flux density of 1 MW/m² and the size of the cylinder was 170 mm diameter and 260 mm height. The power at the aperture varied from approximately 2.5 to 7 kW. Temperatures up to 900 °C were experimentally obtained for the highest radiation power and with a 45° inclination. It was observed that a homogeneous and constant particle flow was difficult to maintain. More details on experimental results are given in Wu et al. [142]. The tests were performed with a radiation flux density in the range 265–670 W/m² and particle mass flow rate in the range 3–9.5 g/s. The measured temperature varied from 385 to 885 °C. For an inclination angle of 45°, the maximum particle outlet temperature of ~900 °C was achieved for a particle mass flow rate of 3 g/s and a flux density of 370 kW/m² at the aperture. The receiver efficiency decreased with increasing outlet particle temperature from 84% at approximately 400 °C to 51% at 900 °C. For the vertical (90°) position and a maximum input flux of 670 W/m² the receiver efficiency reached about 75% (±4%) for particle at ~900 °C. The receiver was scaled up to 2.5 MW_{th} (but never tested at this power level) and qualified with a 100 kW electric heating system [143]. On-sun tests have been performed at the DLR's test facility Jülich Solar Tower [144]. Fig. 6 shows the solar receiver.

During tests, the rotation speed was approximately 45 rpm, the particle mass flow rate was ranging from 0.07 to 0.15 kg/s and the maximum solar flux density was 400 kW/m². Outlet temperatures higher than 900 °C were measured during short time periods. It was observed that particle mass flow rate and film homogeneity were very sensitive the rotation speed.

The French National Center for Scientific Research (CNRS) and project partners developed the fluidized particle-in-tube solar receiver since 2010 [145]. The development steps of this indirectly heated particle solar receiver are summarized in the next paragraph.

The fluidized particle-in-tube concept was also named “upward bubbling fluidized bed (UBFB)”. A key point of this concept is the particle diameter. It addresses type A particles of the Geldart classification [50], typically 50 μm mean diameter particles. The upward movement of the fluidized particles in the tubes is produced according to the following principle. The bottom tip of the tubes (typical ID diameter 40–50 mm) are immersed in a feeder tank in which the particles are fluidized. This tank is named “the dispenser”. The upward mass flow rate of the particle is controlled by tuning the dispenser’s freeboard pressure, as the particle mass flow rate in the tubes is a function of the differential pressure between the dispenser and the top of the tube as shown in Boissière [89]. A secondary air injection (identified as “aeration”)

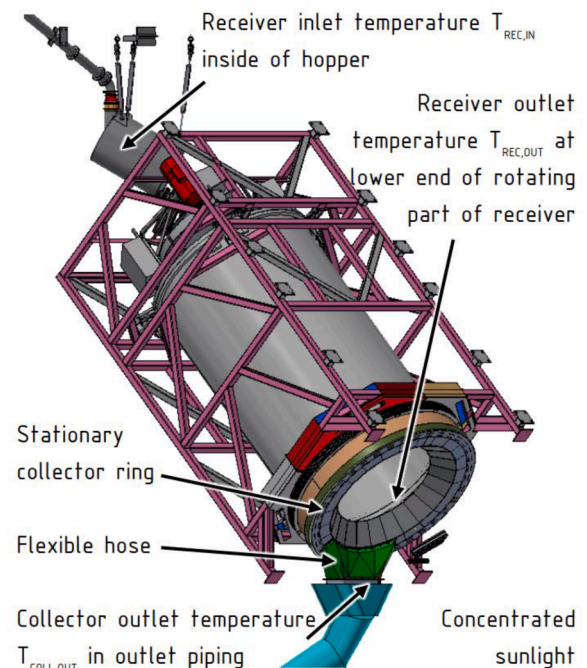


Fig. 6. The DLR centrifugal particle receiver (CentRec) [144].

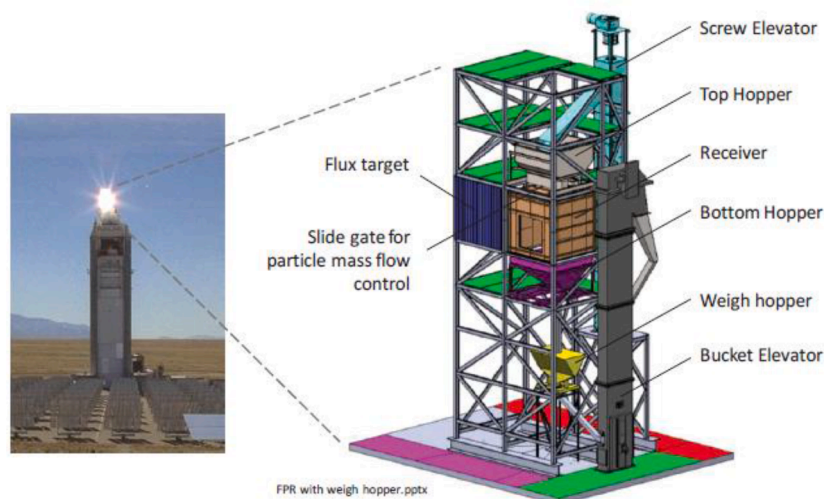


Fig. 5. Sandia's 1MW_{th} particle receiver test loop [140].

located at the bottom of the tubes is necessary to stabilize the particle flow. The typical pressure drop in the tube is approximately 100 mbar/m. The corresponding mean particle volume fraction ranges from 0.30 to 0.45, it decreases with the aeration flow rate. The local particle volume fraction decreases also with the temperature increase along the tubes from the bottom to the top when heated by solar energy [146]. The structure and stability of the particle flow as a function of the tube height, aeration flow rate and temperature is still a subject of research. The main issue is the degeneration of the bubbling regime into the slugging regime thus, the latter resulting in a considerable decrease of the wall-to-fluidized bed heat transfer coefficient. The transitions of fluidization regimes were studied in [47,58]. For air velocities in the range 0.01–0.30 m/s, the freely bubbling, wall slugging and axi-symmetric slugging regimes were identified [96]. The transition between the bubbling and wall slugging regime occurred in the first half meter of the tube. Above 1 m, wall slug coalescence resulted generally in the appearance of axi-symmetric slugs. Fortunately, for type A particles, the increase in temperature results in shifting the slugging transition to a higher bed height of several meters. For higher gas velocity turbulent and fast fluidization regimes were identified in [97]. Recently, the problem of slug occurrence was solved by adding Bubble Rupture Promoters (BRP) long the total tube height of 6 m [58].

The solar receiver development was performed in three steps as summarized in Table 4.

The developments include the proof of concept with a 1m-long single absorber bare tube that achieved 750 °C particle outlet temperature [148] and testing of fin tube [153]. Then an experimental campaign of a particle loop at pilot scale involving a 150 kW_{th} solar receiver and a particle recirculation equipment [154]. Finally, the upscaling of the technology at the MW scale by the implementation of a complete system including a collection and a conversion loop [151]. The latter facility is composed of a 3 MW_{th} solar receiver, two storage tanks, a particle heat exchanger and a 1.2 MW_e gas turbine operating in the hybrid mode (Fig. 7). The tests associated with the three steps were performed using large-scale solar facilities, the 1 MW CNRS solar furnace in Odeillo-Font Romeu for the first two steps and the 5 MW Themis power tower.

The three technologies can be examined with respect to the following criteria assuming that they can deliver particles at 750 °C or higher.

- Acceptable solar flux density
- Construction material issues
- Particle attrition
- Particle loss
- Scaling up ability

Direct absorption solar receivers can accept higher flux density that indirect absorption concept due to the limited value of wall-to-particle heat transfer coefficient and of the operating temperature of the absorber tube walls. Typical values are 1 MW/m² for the former and 0.5 MW/m² for the latter. Construction material issues are identified for the three solar receivers, back wall for the falling particles, kiln wall for the CentRec and tube wall for the UBFB concept. The falling particle receiver is the most sensitive to particle attrition due to the high impact

Table 4
Development steps of the UBFB solar receiver.

Steps	Step 1. Proof of concept	Step 2. Lab-scale	Step 3. Pilot-scale	Step 4. Large-scale prototype
Testing unit	Single tube 0.5 m long	Single tube 1 m long	16 tubes, 1 m long in a cavity	40 tubes, 3 m long in a half cavity
Thermal Power	10kW	40 kW	150kW	3MW
Testing facility	1MW solar furnace	1MW solar furnace	1MW solar furnace	5MW Themis power tower
Reference	[147,148]	[149]	[150]	[151,152]

velocity of the particles at the end of their fall. CentRec and UBFB are not sensitive because of the low particle velocity involved. Particle issues for the UBFB technology were discussed by Kang et al. [155]. Particle loss is a critical issue for open direct absorption particle receivers due to temperature and wind effect on particle flow stability. Scaling up ability to large scale, typically some 100 MW_{th}, is examined in Section 7. The next section addresses the particle handling issues in Particle CSP application.

3. Particle handling in particle-driven CSP plants

3.1. General considerations

The solids heated in the solar receiver are transferred to the thermal power block and stored before their use. In turn, the cooled solids leaving the power block are stored before being transferred back to the solar receiver to be reheated. The number of solar fields in a project will depend upon a combination of economic factors and power requirements so the discussion deals only with the requirements for a single field.

The typical solar tower will be between 100 and 200 m high, and the power block is at ground level. Consequently, in addition to moving the solids horizontally, they also have to be moved vertically. The horizontal distance will be determined by the site arrangement but is likely to be at several hundred meters. A design requirement is that the transfer equipment is enclosed to minimize dusting, and insulated to minimize heat losses and maintain the solids temperature. The thickness and multi-layer composition of the refractory insulation (low density alumina refractories, ceramic fiber and rockwool backing) should guarantee an outer wall temperature of around 50 °C. The heat losses are hence limited to the natural convection of the ambient air and the outer wall. With a heat transfer coefficient of natural convection at curved or flat surfaces in the order of 3 to 5 W/m²K, heat losses can be limited to well below 0.1 kW/m².

To eliminate the need for equipment to move the hot solids downward, gravity provides the motive force. The solids leaving the solar tower are directed to the horizontal transfer system and later are discharged into hot storage from above the hoppers. Elevators are required to raise the cool solids to the level of the solar receiver and, depending on the design selected, from storage to the horizontal conveyor

Two important considerations for the solids transfer system selected will be reliability and availability. As the operating window for heating the solids is limited to between 7 and 10 h, even a relatively short interruption could reduce the amount of hot solids stored and, thereby, reduce power plant output. Such an interruption would be exacerbated if, for example, two solar towers shared a transfer system. Hence, to achieve the required availability, each solar tower should have a dedicated horizontal conveying system, and the equipment selected must be reliable with acceptable inspection and preventative maintenance requirements. The effect of flow interruptions can be managed, at some additional cost, by the provision of surge-capacity hoppers.

This section discusses the selection process for the handling equipment required to move the solids horizontally between the solar towers and the power island, raise the solids vertically, and feed them short distances between equipment items.

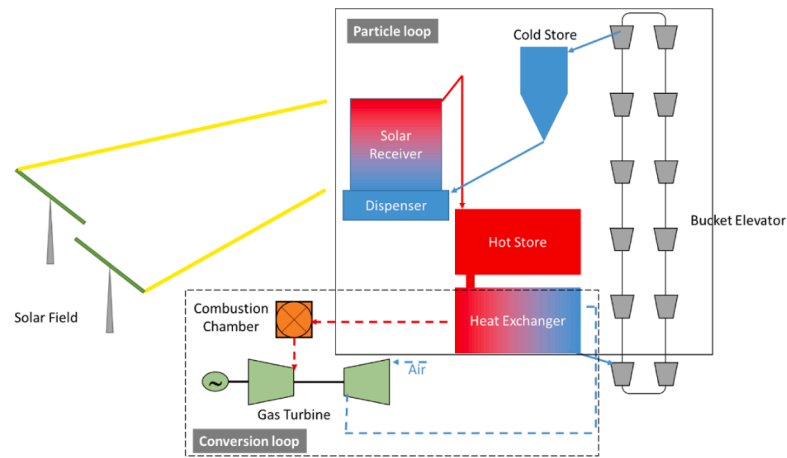
3.2. Potential solids conveying systems for long distance horizontal solids transfer

3.2.1. Systems that do not meet the requirements

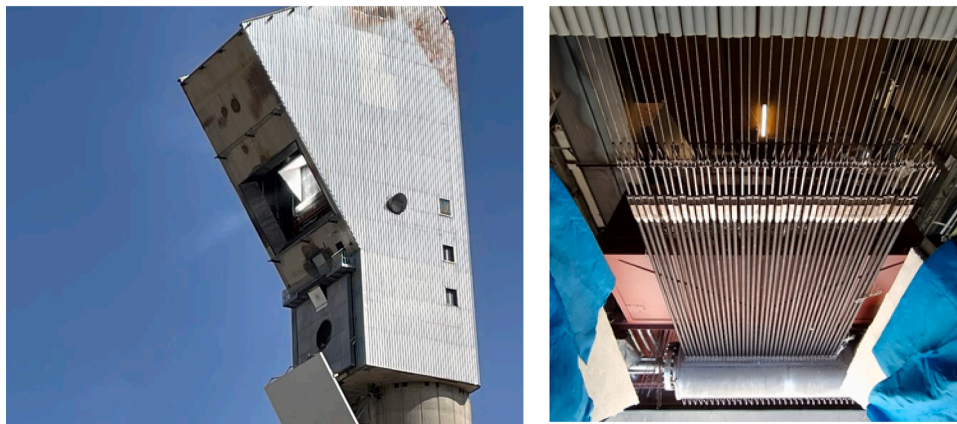
Several options have been investigated, but only those able to operate at elevated temperatures are discussed.

Those eliminated are presented first in detail:

Drag chain conveyors [156,157]. The maximum operating temperature is limited to 450 °C. Also, the maximum conveying capacity of



a. Next-CSP Prototype layout



b. The solar receiver with the cavity during solar test (left) and without the cavity (right).

Fig. 7. The Next-CSP prototype.

60 m³/h and the maximum horizontal conveying distance of 60 m would require multiple units making the selection uneconomic.

Pipe Conveyors [156,158,159]. Although satisfying the conveying capacity and horizontal distance criteria, the maximum operating temperature is limited to 150 °C.

Two additional technologies, although able to meet the design criteria of operating temperature, conveying capacity, and conveying distance were also eliminated for the following reasons.

Dilute-phase pneumatic conveyors: The conveying air cools the solids, and although around 75% of the heat transferred to the air can be recovered, the power plant would be derated by up to 14%.

Railway wagons [160]: Complying with regulations results in wagons only carrying 50 tons of solids, requiring multiple wagons to transfer the 790 tons of solids per hour for each solar tower. The resulting short feeding and discharging times for this intermittent operation are difficult to achieve. Additionally, the cost of the system was greater than that for alternative technologies.

Screw conveyors [161–166], and **vibrating conveyors:** Both these technologies satisfy the temperature and conveying capacity requirements but only for distances up to 15 m. Although not suitable for long-distance conveying, they could be used as solids feeders in the Power Island and delivering hot and cool solids to and from the long-distance conveyors. These technologies are presented below and will be discussed further in this section.

3.2.2. Selected horizontal conveying techniques

Two conveying technologies have been identified that have the potential to meet the selection criteria, but both present significant design challenges. Experience from coal-based power demonstration projects identifies that introducing novel features or designing outside of operating experience can result in operational issues that cause extensive delays and cost overruns. Careful analysis is required to determine which design is the more reliable. Given the high temperatures involved and the cooling time required, mechanical failures will take time to rectify. This loss of availability and the loss of generating revenue needs to be factored into any economic assessment.

Apron Conveyors [167–170]:

A conveying system consists of two horizontal pulleys around which a continuous belt of linked plates rotates. At least one pulley is powered; the powered one is the drive pulley and, if unpowered, the other one is the idler pulley. The solids from the solar tower will enter the conveyor at the idler end and discharge at the drive end into the hot storage hopper. As the belt loops beneath the loaded section, it returns to the feed point empty hence, a separate conveyor is required to deliver the solids from the cool hopper to the solar tower. However, as the design also operates inclined, it can collect solids from the cool hopper discharge and by raising their elevation reduce the number of vertical elevators required to feed the solar tower.

Apron conveyors are used to transport hot clinkers from cement kilns to storage silos. The clinker temperatures are usually in the range 500 to 800 °C, although they can be higher under upset conditions. To

withstand the high temperatures and heavy-duty requirements, the belt consists of closely fitting steel plates. Plates across the belt form cells to “anchor” the solids on the belt, and overlapping side plates prevent spillage into the space below the belt. The traction is provided by chains on either side of the plates or by a steel wire belt on which the plates are mounted. Although the solids conveyed may be as high as 800 °C, the conveyors are open, allowing natural cooling of the conveying structure so that the structure and drive mechanism, chain or belt, are at lower, more acceptable temperatures. To reduce air-related sensible heat losses, the design proposed for the solar application is enclosed so the conveyor enclosure and drive mechanism would be at the same temperature as the solids.

To provide corrosion resistance, stainless steels will be used that, at 800 °C, will have lost a large proportion of their tensile strength. The elevated temperature will also require certain departures from standard conveyor design.

- The conveying casing will also have to be reinforced to avoid distortion, adding to the amount of steel required. In addition, slip joints would be required to accommodate thermal expansion.
- For increased wear resistance, the drive chain is hardened, a property that will be lost at elevated temperature in addition to the loss in tensile strength. For this reason, the chain drive would have to be mounted outside the conveyor. This will require a redesign of the conveying mechanism inside the conveyor.
- The drive belt will remain inside the conveyor, where the temperature rise will expand its length. A 500 m conveying distance will require a 1000 m long belt, which expands. Arrangements to accommodate this expansion may limit the length of an individual conveyor and require more than one to traverse the 500 m.

Side-Pulled Conveyor [171,172]:

An alternative to the apron conveyor is the side-pulled conveyor. This design uses a drive chain located outside the conveyor casing to which are attached flights that penetrate the casing to contact the solids. The drive pulley shaft is vertical, and the chain with flights returns to the idler pulley within a continuation of the casing located to the side. In this way, unlike the apron conveyor, the returning side can be used to convey material. Applied to the solar project, the side-pulled conveyor could deliver hot solids to the power block on one side and return cool solids to the solar tower on the other. As this double-duty increases flow resistance, both pulleys will likely be driven. This design cannot negotiate inclines so will require more vertical elevators than the apron-belt design. Hence the whole conveyor length would run approximately 20 m above ground level, the actual elevation determined by the height of the hot storage hopper solids inlet.

A design issue is the turning moment placed on the single chain by the force required to move the solids. The flights will be at 800 °C and will have to be reinforced to compensate for the associated loss of strength. The use of two chains with the flights attached to each is not possible as the outer chain has to travel further when negotiating the pulleys. Penetrating both side walls would also complicate the design of the casing, for which the lid would have to be supported separately to the base to provide a clear gap all around

3.3. Potential vertical transfer systems

Four methods of raising the solids can be considered. A bucket hoist, which rises individual loads up the tower is not recommended. Its operation is discontinuous and requires intermediate storage to ensure continuity of solids feed to the solar receiver. This places a large mass at the top of the tower requiring that the structure and foundations be reinforced to carry the additional load. Additionally, to place the hopper discharge at a similar level to the receiver solids feed system, the elevator hoist has to raise the solids to the top of the hopper requiring a higher vertical lift than alternative elevators. For these reasons, this

option was eliminated from consideration.

Bucket Elevator [18,173,174]:

A bucket elevator consists of a series of buckets mounted on two continuous chains. Like the horizontal conveyors, the chains are moved using a drive pulley with sprockets located at the top of the elevator with an idler pulley at the bottom. To reduce drag, the solids should be fed directly into the bucket rather than picking them up by passing through a bed of solids at the foot of the elevator. The filled buckets rise up the elevator, pass over the drive pulley, and discharge through a chute.

The solids feed system for the solar receiver is approximately 120 m above ground level. Suppliers indicate that the maximum lift height for a bucket elevator is 65 m for a solids flow rate of 400 tons per hour. As the horizontal conveyor will discharge solids approximately 20 m above ground level, four elevators will be required. Two elevators will each lift 395 tons per hour to around 70 m and discharge into two additional elevators to lift the solids to around 120 m.

Inclined Apron Conveyor:

The apron conveyors discussed previously are also capable of operating at inclined angles up to 60°, which would require taller cross plates to prevent the solids from flowing back. Illustrations of an inclined apron conveyor are given in standard conveying handbooks. For a conservative inclination of 45°, the conveyor would be located 100 m away from the solar tower, and the horizontal conveyor would discharge into it. To reach the 120 m level would require an elevator 140 m long, well within the capabilities of the design. The advantage of using this approach is that only one elevator will be required, but a potential drawback is the shadow it could cast across the solar field.

Dense-phase Pneumatic Conveying:

Pneumatic conveying can be considered [175]. Since high-temperature filtration can be used to de-dust the conveying air at a sub-micron particle size level, the hot conveying air can be re-used for the conveying itself, thus reducing sensible heat losses commonly encountered in pneumatic conveying. If a dense-phase conveying is applied, at solids-to-air ratios of 100 to 250 kg solids/kg air, the air flow will be limited. Pneumatic conveying has the advantages of cost and reliability. Mechanical conveying concepts will imply significant extra power needs due to not only lifting the particles, but also the heavy-weight chains and buckets. Dense-phase conveying is however a non-mechanical concept where only the particle lifting and friction and acceleration losses need to be accounted. The conveying power is hence predicted to be 60 to 70% only of the power required by a mechanical particle lifting. The low solid and air velocities applied in a dense-phase system moreover lead to a conveying of particles without major pipeline erosion or particle degradation.

3.4. Additional conveying methods

The solar project will require solids feeders at various locations within the solids transfer system between the solar towers and the Power Island, and within the Power Island. For example, the Power Island feeders will be required to feed hot solids to and remove cool solids from the fluidized-bed heat exchanger. In the solid’s transfer system, feeders will be required to transfer hot solids from the solar tower to the horizontal conveyor, and to remove cool solids from storage.

Three possible feeders were identified, and these are discussed.

Screw Feeders

This conveying system consists of a rotating screw blade located within a sealed U-shaped trough. The screw is driven at one end of the trough and supported at the other. If more support is required, hangers, suspended from the top of the trough, can be located on the screw shaft at points between the screw sections. The screw feeder can handle the required volumetric flow, but the conveying distance is limited to around 12 m primarily by the torque required to turn the shaft of the screw.

High-temperature feeders are offered by suppliers but are not common plant items, and as such their design may carry a higher element of

risk. The materials of construction are expensive; for the cool solids, 310 austenitic stainless steel will be acceptable, but for the hot solids higher-grade steel such as 254 SMO, will be required. The design will need to accommodate differential thermal expansion between the trough and the screw. Because of the high temperatures, the drive and end bearings will be mounted distant from the trough where temperatures will be lower.

The screw flight design is adjusted to suit the properties of the material being conveyed. For the fine sand, to ensure that it moves forward efficiently, a short-pitch, close-tolerance screw may be used, with the feeder declined slightly towards the discharge opening. To limit product degradation and abrasion, the screw will turn at the slowest speed possible to achieve the required flow rate. To further limit abrasion, the flights and the trough are plasma coated with hard surfacing materials such as plasma-sprayed chromium carbide. Even with these measures incorporated, abrasion and product degradation may be high, in which case two or more screws in parallel may be required to lower the screw speed.

Vibrating Tray Feeders

When the tray vibrates, the solids are agitated and move along the tray in the direction of the vibration. To assist motion the tray can be declined and provided that the declination is less than the angle of repose, solids motion should cease once the tray stops vibrating. For large industrial units, the tray is mounted on springs and the vibration is generated using electromagnetic or pneumatic drives. For the solar application, these would have to be mounted outside the insulation layer. Vibrating tubular conveyors are also available but do not feed at the rate required, 390 m³/h.

The tray must be free to vibrate and cannot be mechanically attached to the feed or discharge equipment. To prevent dusting, flexible seals are required at these locations. At low-temperature operation, elastomer seals are used. At the higher temperatures, a silica or ceramic fiber seal would survive the temperature, but how they would function under constant medium-amplitude, low-frequency vibration is unknown. Metal bellows are used to prevent transmission of low-amplitude, low-frequency pump vibration to pipework, but again their suitability for use on the solar project is unknown.

Despite meeting the operating temperature and solids volumetric flow criteria, if suitable seals cannot be identified then, for health and safety reasons, the vibrating feeder will not be selected.

Solids Removal from the Solar Receiver

The hot sand leaving the top of the heat transfer tubes will be collected and spillover, descending approximately 100 m to the elevation of the horizontal conveyor. Allowing 800 tons/h of sand to fall 100 m vertically will land at the bottom of the pipe with a significant impact load sufficient to damage refractory and distort metal. The design needs to remove this possibility. This could be achieved using a zig-zag pipe arrangement to slow the solid's rate of descent. The tubes should be stainless steel to avoid problems with refractory differential expansion. However, the sand will likely wear the metal which will need to be protected by surface hardening. If an acceptable design solution for a gravity discharge system cannot be reached then consideration should be given to more controlled removal using a conveyor system. By adding moving equipment, this solution comes at increased capital and maintenance costs.

3.5. Conveying and feeding equipment design considerations

Equipment suppliers understand their equipment, but the solar project application may pose several challenges with which they do not have ready answers. Points to be clarified as part of the equipment selection process include the following.

- As the equipment heats up, so the metal will expand. Hence, chains and belts that were correctly tensioned when cold will need to self-adjust when operating at temperature. The measures adopted at

lower temperatures may not be applicable for the enclosed high-temperature designs under consideration.

- To achieve the required high reliability, in addition to selecting equipment with the potential for high reliability, some preventative maintenance and inspection schedule will be required. Ways of achieving this need to be clearly established.
- The conveyor carries certain standard monitoring instrumentation to ensure reliable operation and help reduce component wear and deterioration. Speed switches are used to curtail feed to the conveyor should it slow down or trip. All such instrumentation should function reliably at elevated operating temperatures.
- The solids feed rate to the various equipment items, especially the solar receiver and the fluidized-bed heat exchanger, need to be accurately measured. How this is to be achieved needs to be established. Such measurements will be fed to the control logic to facilitate control of the solar process and the protection of equipment from damage.

As a part of the solids transfer equipment selection, consideration should be given to the benefits of equipment standardization. These include the following.

- Maintenance and operational teams will be more familiar with equipment issues and how best to rectify them. The sharing of this experience with common equipment items shortens the start-up period and leads to a more reliable plant.
- Standardization of maintenance tasks improves productivity resulting in shorter maintenance turnaround times.
- Spare parts inventory will be lower, reducing the cost of stock-keeping and spare part management.

3.6. Solids storage hoppers

3.6.1. Design principles

The application will require two sets of hoppers, one for the hot solids and one for the cool solids. If there are several solar towers, it is likely they will share hoppers to limit capital costs. Both types of hoppers will be carbon steel vessels lined with refractory, an insulating layer next to the wall covered with a protective abrasion resistant refractory, which comes into contact with the solids. A wealth of experience has been gained from refractories operating at up to 900 °C in circulating fluidized-bed combustors that should be applied to the benefit of the solar project. A vital piece of information is that to avoid premature failure of the hard-faced refractory it should not be allowed to heat up or cool down at rates greater than 50 °C/h: at higher rates the greater the likelihood of surface cracking increases.

Cracking can also occur for two additional reasons. During refractory dry-out of thick layers of low permeability refractory, water vapor can build up sufficient pressure to create cracks. Adding moisture-release fibres to the refractory to provide paths to vent the water vapor can minimize this problem. Some fibres are tubular and others shrink or burn out as the refractory heats up. The second reason is when insufficient allowance is made for refractory expansion requiring that expansion joints be carefully designed.

When the refractory is hot, fine solids enter these cracks, and as the refractory cools the crack closes. In this way, the solids in the crack create sufficient local stress to cause the refractory to spall away from the surface. If sufficiently large, the spalled material can interrupt solids flow, and the space left in the wall will accelerate further damage. In the worst case, the insulating refractory will be damaged and expose the vessel wall to high temperatures and possible failure.

The vessel will be heavily insulated internally, but suddenly impacting an internal surface only marginally cooled with 600 or 800 °C material will exceed the 50 °C/h temperature limit. Some measures are available to minimize the effect of any cracks formed, one of which is the addition of approximately 4% by weight of 310 steel fibers to reinforce

the refractory. These fibres are typically 35 mm long with a diameter of 0.4 mm, and by expanding more than the refractory they create a network of fine cracks too small for the sand to enter. The presence of the fine cracks allows the refractory to expand without further cracking, and so improve the resistance of the refractory to thermal shock. A variety of refractory materials and methods of application are available and vary by supplier, the careful selection of which will be essential to the reliability of the refractory-lined vessels.

As spalling can still occur with even the most carefully installed refractory, early detection of vessel wall overheating is essential. Two approaches should be adopted. First, the carbon steel outer surface should be painted with temperature-sensitive paint to alert operators that the failure process is in progress. The second is to complete regular infrared thermographic surveys of the vessels. These provide early detection of areas of increased temperature and allow their progress to be monitored.

The insulating refractory will be sufficiently thick to achieve an external temperature of 50 °C to limit heat losses. Hot solids will be drawn from storage typically between 19:00 and midnight and filled again between 09:00 and 17:00. Hence, between midnight and 09:00, the hoppers will be cooling. One way to limit the cooling is to leave some hot solids in the vessel, although this will increase the size of vessel required. If determined to be advantageous, this same approach should also be used with the cool-solids storage hoppers. Leaving solids in the hopper will also prevent falling solids directly impacting and damaging refractory.

As the solids are free-flowing, it may not be necessary to use the steep-sided, conical hopper walls of mass flow designs. These also make the hoppers taller and raise the height the conveyor or elevator has to raise the solids to the inlet port. Instead, it is proposed to use cones with a 30° incline. To ease movement of the solids to the exit, they will be fluidized locally, taking care not to erode the refractory, by air introduced through metal lances distributed across the cone. A common problem in fluidized-bed combustion is solids backflow through the air distributor nozzles, and the design and arrangement of the lances should cater for such an eventuality. At least initially, the flow resistance of the fixed-bed of solids above the cone will result in the majority of the fluidizing air leaving with the discharged solids, something that the solids removal equipment must accommodate.

If shared with other solar towers, the roof of the hot solids hopper will have more than one solids entry port. These should be located to avoid solids impact with the hopper walls, and each will be provided with isolation valves. The number of removal ports will need to be determined by detailed design. Assuming that an extraction feeder is required to feed the conveyor, factors to take into consideration are as follows.

- A single hopper extraction point has the advantages of simplicity, but if the feeder/conveyor fails then all the hot solids are isolated from use. Additionally, a feeder/conveyor capable of handling the required flow would be required.
- Although an extraction port for each solar train would allow for maximum availability (if one fails, then others are still available), access for multiple feeder/conveyors both below the hopper and in the vicinity of the fluidized-bed heat exchanger may prevent this. A detailed plant layout is required to determine the arrangement and number of hopper solids extraction and fluidized-bed feeder trains.

The cool solids returning from the Power Island will be elevated to the top of the hopper using a similar feeder/conveyor arrangement as used to feed the hot solids. The number of removal ports per hopper is fixed by the number of horizontal conveyors to be fed, but how to feed those conveyors will need to be determined by detailed design. Factors to take into consideration are as follows.

- If the apron feeders are selected, then an extraction feeder can direct the solids directly to the conveyor at ground level allowing the conveyor to rise to the elevation required for the feed arrangement to the solar tower.
- If side-pulled conveyors are used, then the solids also need to be elevated. The extraction feeder could feed either a vertical or inclined elevator. Depending on the equipment layout, the extraction feeder may have to travel a distance that eliminates the use of screw and vibrating feeders.

Solids level detection is an important measurement to avoid overfilling the hopper and also to avoid draining it if a solids inventory is to be maintained. Sensors are available for reliable level detection at lower temperatures but what would be used at elevated temperatures needs to be established. One option may be a cooled version of a conventional sensor such as microwave or radar detectors. Wall-mounted capacitance probes that penetrate into the solids may not be successful.

3.6.2. High-temperature valving

The solids transfer system will require numerous high-temperature valves to isolate equipment either when not in service or when downstream equipment fails. Fortunately, there is a wealth of relevant experience from fluid catalytic cracking (FCC) units to help guide the selection of the most appropriate valving. FCC is a high-temperature process that uses a catalyst (150 µm to 0, with a mean size of 70 µm) to crack high-molecular-weight hydrocarbons into lighter, more valuable products such as petroleum and olefinic gasses. The catalyst is progressively coated with carbon that is burnt off in a regenerator operating at around 800 °C and 2.5 bar. The valving required to control the flow of the abrasive, high-temperature catalyst can be expected to be equally suitable for application in the solar project for which the olivine sand used is of a similar size and abrasivity.

Depending on the supplier, these valves can be either ball valves or gate valves, and each type is available in sizes up to 900 mm, more than adequate for the solar project application. An advantage of the solar project application over that of the FCC process is that the system is at a lower pressure, which may allow clearances within the valves to be increased, reducing the likelihood of the valve seizing. The isolation valving usually consists of a pair of valves as follows.

- The main on-off valve is automatically actuated to achieve rapid cut off in an emergency. It might also be closed to isolate filled solids storage hoppers from the conveyors.
- Immediately upstream of the main valve is a valve that opens and closes manually to allow work on the main valve, and as such must provide a tight seal against solids flow.

Whatever type of valve is used, it must operate reliably, be resistant to corrosion and erosion, and accommodate the effects of thermal expansion and thermal shock. For the solar project application, the exposed surface will be protected from erosion by chromium carbide applied by high-velocity oxygen fuel thermal spray. Some manufacturers use ceramic balls for erosion resistance, but these would have to resist thermal shock upon start-up and restart each day.

3.6.3. Dust control

The release of dust and the associated hot air is to be avoided. In addition to constituting health, environmental, and safety hazards, the dust may drift across the solar fields. The potential for dust emissions in the conveying system occurs at each point solids enter a vessel, as the entering volume of solids will displace a similar volume of dusty air. If the only way out for the air is counter to the solids, then solids flow may be impeded. To vent this displaced hot air safely, it will first have to be filtered. As the filters offer flow resistance, an extractor fan will be required to assist the airflow through the filters.

Filters are in service operating at temperatures above 800 °C, and the

technology is readily applied to the requirements of the solar plant. In these other applications, in addition to its temperature, the gas stream contains corrosive species, in which case the solar application is less demanding. Sintered Fecralloy® metal fibres are formed into cylindrical elements of various designs, self-supporting or internally supported, plain-faced, or pleated to increase the surface area per element. To raise removal efficiency, the dust collects on the outer surface and forms a filter barrier. Once the pressure drop across the filter reaches a specific value, the dust cake is blown off with a pulse of high-pressure air. The efficiency of the filter itself can be increased by using finer fibres, but this also decreases porosity and raises pressure drop. The final design selection will depend on the particle size of the dust presented to the filter and on an acceptable compromise between efficiency and pressure drop.

The volume of solids from a solar tower can be up to 230 m³/h (without voidage). These will displace a similar volume of gas at the hot solids surge hopper and the conveyor entry point, and also at the entry points of the cool solid's conveyor and the elevators. At the hot and cool storage hoppers, where multiple streams may enter, the volume of gas displaced will be correspondingly higher. The hopper filters will have to be sized for the fluidizing air used to assist solids removal. If high-temperature fans for such low throughputs are not available, a standard fan protected by an upstream gas cooling circuit will be required.

4. Particle-driven heat exchangers

4.1. The particle-to-working fluid heat recovery in the power block

Being the equipment that usually withstands the highest pressure and temperature in the thermodynamic cycle, the primary heat exchanger (or set of heat exchangers, depending on the cycle) is of utmost importance to the plant's performance and economics.

Due to the difficulty to pressurize high quantities of particulate solids and to efficiently separate the particles from a fluid, the heat transfer from particles to the working fluid is not considered feasible via direct contact, despite the typically high efficiency of such a solution. Particle-to-working fluid heat exchangers are therefore selected to be an indirect model, and can be divided into fluidized-bed heat exchangers and moving bed heat exchangers. While fluidized-bed heat exchangers are generally the preferred solution thanks to their higher heat transfer coefficient, moving packed beds can be used for bigger or denser particles whose fluidization would be heavily penalized in terms of thermal losses and auxiliary consumptions. A review of heat recovery technology from high temperature particles is presented in [176].

4.2. Moving bed heat exchangers

Baumann and Zunft first proposed a shell-and-tube, moving bed heat exchanger [177] used to transfer heat from an air solar receiver to a storage medium made of coarse particles of diameter ranging from 0.56 to 2.89 mm. The same architecture (moving bed of particles on the shell side, fluid in the tubes) was then suggested to serve as hot source for a water/steam Rankine cycle [178]. The study of its flow dynamics and heat transfer [179,180] showed that particle-side heat transfer coefficients up to 240 W/m²K could be reached.

Moving packed beds were further investigated by the particle solar pathway of the US-DoE's SunShot initiative [18]. In particular, a moving packed-bed, shell-and-plate configuration was characterized extensively regarding heat transfer [181,182] and transient behavior [183], exhibiting overall heat transfer coefficients of 380 W/m²K for particles of 200 µm in diameter. That configuration was selected by Sandia for the construction of a pilot to be integrated with their particle receiver and sCO₂ test loop [184,185], considering its fair performance compared to fluidized-bed heat exchangers for the considered particle diameters, and its superior potential for improvement as compared to shell-and-tube moving bed heat exchangers. Nevertheless, technical manufacturing

challenges must be addressed for this design, and then printed circuit heat exchanger (PCHE) technology is necessary to accommodate high pressures at the gas side [182].

4.3. Fluidized bed heat exchangers

4.3.1. The particle-to-tube wall heat exchange coefficient

In the absence of receiver-related constraints that make the use of large particles (diameters > 200 µm) necessary, fluidized bed heat exchangers are not heavily penalized by the parasitic consumption and heat losses caused by a high flowrate of fluidization air. Their better heat transfer coefficient compared to moving packed bed heat exchangers can then be taken advantage of. The variation of fluidized bed-to-surface heat transfer coefficient with particle properties and operating parameters was studied since decades [186–188]. The effect of the particle size, shape, density, specific heat, air mass fluidizing velocity, tube size, tube material, bed depth, heat flux and distributor design [186]. Particle size and operating temperature and pressure (as well as bed to heat transfer surface temperature difference) are the main parameters affecting the heat transfer coefficient. In particular, it is well known that h_w increases with a decrease in particle diameter [188]. For example, the following values of h_w are reported, 600 W/m²K for 241 µm glass bead and a 12.7 mm O.D. tube [186], 500 W/m²K for 370 µm alumina particles at 800 °C and a 35 mm O.D. tube [187], and 800–900 W/m²K for 160 µm sand particles [188]. Recently, heat transfer coefficients as high as 1600 W/m²K were measured for 129 µm sand particle and 6 mm O.D. horizontal tubes [189]. Data for horizontal tube bundle are presented in [190].

Among recent applied studies regarding CSP or heat storage, Haider and Schwaiger et al. [191] proposed a thermal storage system based on fluidized particles, with insight on the design of the heat exchanger. Ma et al. [192] suggested replacing solar salts with particles in a CSP plant, using heat exchangers similar to those used in fluidized-bed coal plants. More detailed modeling works [193,194] proposed a counter-flow arrangement of heat exchangers (multistage fluidized bed), assuming perfect mixing on particle side in each module [195]. All the modeling work presented above mainly relies on correlations from the literature. However, due to the high uncertainty on the particle-side heat transfer coefficient, experimental validation is necessary.

Li et al. [194] investigated the benefit of heat transfer enhancement on the bed-to-wall heat transfer coefficient. They observed significant benefits when using finned tubes: up to 1200 W/m²K for particles of 128 µm average diameter, 1600–3000 W/m²K for smaller particles of 85 µm average diameter. However, the latter already measured very good bed-to-wall heat transfer coefficients (around 800 W/m²K) for bare tubes, to be compared to a wall-to-working fluid coefficient of 325 W/m²K. In that particular case, the benefit of fins in terms of overall heat transfer is probably not sufficient to justify the additional cost of using finned tubes. The situation is different with other heat transfer fluids as shown in the next section.

4.3.2. The tube-wall to working fluid heat transfer

Depending on the working fluid used, heat transfer coefficient can be predicted from literature data. They are represented in Fig. 8 for various working fluids.

Whereas for LP and HP air, the heat transfer resistance will be mostly located inside the tube, other working fluids are characterized by a heat transfer coefficient that approaches the bed-to-tube value. Both heat transfer resistances will hence play a proportional role.

4.3.3. Design considerations for a bubbling fluidized-bed heat exchanger to be used as hot source

The choices leading to a design of bubbling fluidized-bed heat exchanger are mainly driven by the following criteria, adapted from [184,196]:

- Affordability (both CAPEX and OPEX): being the equipment that is most heavily exposed to thermo-mechanical stress, such an exchanger can be expected to use noble materials such as Ni-based alloys. Exchangers are reported to cost about two times more when using austenitic stainless steel, as compared to carbon steel heat exchangers, and the factor increases to 5 if a Ni-based alloy such as Inconel 625 is used [197].
- Compatibility with the particles necessary to the receiver: usually, the type of receiver prevails when selecting the particles. Depending on the particle type [50], fluidized beds – as opposed to packed beds – may be a more or less practical and cost-effective option.
- Heat transfer: while high temperatures are detrimental to the receiver's efficiency, they tend to improve the cycle's conversion efficiency as indicated in Section 6. The heat exchanger should therefore allow a minimal temperature difference between the particles and the working fluid.
- Pressure losses for the working fluid: pressure drops are relatively benign for Rankine cycles where the working fluid is compressed in liquid phase. However, their potential substitutes presented in Section 6 are Brayton cycles that compress gasses with significant power consumption [198,199]. These cycles will be much more sensitive to pressure drops, so that a compromise needs to be made on fluid velocities: higher Reynolds numbers will be favorable to heat transfer, at the expense of higher pressure drops, and vice-versa. Fig. 8 illustrated this compromise for a fixed geometry, typical for a shell-and-tubes heat exchanger, at pressure/temperature conditions of the working fluid that are representative of the different cycles. While supercritical CO₂ and steam do not seem impacted by pressure drops, the low density of air in a gas turbine penalizes it heavily, thus making it difficult to obtain good heat transfer coefficients without incurring excessive pressure losses. With water or supercritical CO₂ as working fluid, the heat transfer coefficient on the particle side (between 200 and 800 W/m²K as mentioned above) prevails because it is much lower than that on the fluid side. Heat transfer intensification on particle side has shown significant gains in terms of heat transfer [194], but the economic gain to be expected from such measures is still uncertain. While finned tubes clearly lead to a reduction in heat exchange surface when a high-density working fluid is used (steam or supercritical CO₂), such designs are not relevant for fluidized beds exchanging heat with low-density working fluids such as air at low pressure, as the heat transfer limitation is rather on the wall-to-working fluid side.
- Parasitic and thermal losses: the main parasitic consumption related to such equipment arises from the air compressor for fluidization. This consumption is primarily dependent on the pressure ratio and air flowrate that correspond respectively to bed height and particle size and density. Thermal losses are directly linked to the flowrate of

- fluidization air: fluidization air leaves the heat exchanger at particle temperature whilst it usually enters the compressor at ambient temperature. Excessive losses can be mitigated by recirculating a portion of the air, but compression becomes impractical above a compressor inlet temperature of 400 °C [191]. For a better heat recovery, an exchanger is needed between compressor outlet and bed outlet; due to the poor heat transfer characteristics of air at nearly atmospheric pressure, such an option may prove uneconomical.
- Structural reliability: due to the extreme temperatures and pressures to which the equipment is exposed, its intrinsic ability to withstand high pressures and temperature cycling is of utmost importance. Thermal expansion should be particularly looked after, as a rod of SS347 will typically gain 1% in length from ambient to 538 °C [200], that is around 1.5% from ambient to 800 °C.
- Manufacturability: the geometry and material selection should be as close as possible to standards allowing for easy manufacturability. Otherwise, the economics or even the mere feasibility of such an equipment would be problematic.
- Scalability: a gain in specific costs is usually expected from process equipment when their capacity increases. Although the gain is usually higher when increasing the size of a single equipment (up to a certain size), modularity can also result in economic gains and improve overall availability through redundancy.
- Off-design and transient operation: although nominal efficiency is generally the ultimate target of early design, a certain flexibility is expected from CSP plants that usually start up every day. The thermal inertia, driven by the mass of metal and the inventory of particles and working fluid, can be an important parameter regarding the plant's overall quick response. Simple and quick temperature and flow control on both sides of the exchanger are required for operational stability as well as fast load change.
- Maintainability: the geometry and location of the heat exchanger should facilitate its access, inspection and maintenance.
- Compactness: a moderate size tends to minimize the length of piping connected to the equipment, thus limiting the thermodynamic cycle's overall pressure drop and inertia. Even more importantly, compactness usually results in benefits on all the criteria mentioned above.
- Maturity: a design with similarities with other industrial equipment will (at least partly) benefit from their operating experience, thereby potentially improving its availability.

Considering the high complexity of the phenomena involved, their importance in the overall plant's reliability and economics, and the lack of predictive models consolidated with experiments and industrial experience, particle heat exchangers should be a key R&D subject in the years to come.

5. High efficiency thermodynamic cycles

As shown in the detailed example of a peaker tower CSP plant (Section 10), the solar island of a CSP plant accounts for approx. one third of its Capex whose amortization accounts for more than 80% of its LCOE. For a baseload plant of the same thermal power, the share of the solar island in the CAPEX is even higher, as the cycle and (more marginally) the thermal storage are smaller.

Besides, the cleaning of the heliostat mirrors represents a significant share of the O&M costs that are the remaining part of the LCOE. Consequently, one of the best drivers to lower the LCOE of a CSP plant is to downsize the solar island, which means reducing its thermal power. For a given amount of yearly power generation, it amounts to increasing the efficiency of the power cycle. That reasoning, as well as the present section, applies to all types of CSP systems and in particular to those using particles, insofar as they can reach the typical hot temperature for each cycle.

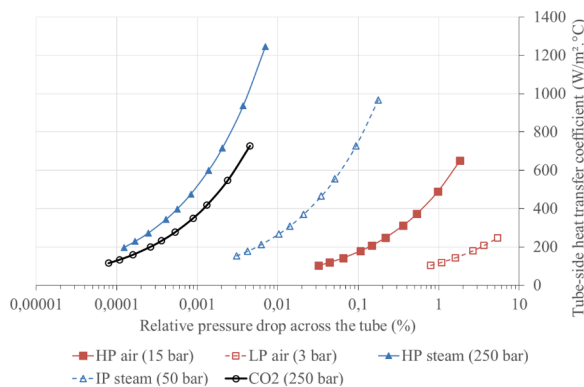


Fig. 8. Tube-side heat transfer coefficient vs. pressure drop for an 8 m long tube with an internal diameter of 9 mm in the turbulent regime ($10^4 < Re < 10^5$) at an average temperature of 600 °C.

5.1. Constraints affecting the power cycle that are specific to CSP

In an ideal Carnot cycle, the heat input to and the heat release from the working fluid are isothermal. Supposing that the temperature of the working fluid during these heat exchanges is T_{hot} and T_{cold} respectively, the cycle efficiency is equal to $1 - T_{cold}/T_{hot}$. However, in most real thermodynamic cycles, the temperature of the working fluid increases during the heat input and/or decreases during the cooling. Let us consider, as an example, the Brayton cycle of a gas turbine pictured in Fig. 9.

T and S represent the temperature and the entropy of the working fluid. The isobaric heat input starts at 2 and ends at 3 (1–2 is the compression, 3–4 the expansion and 4–1 the isobaric cooling). The temperature that matters regarding the cycle efficiency (i.e., corresponding to T_{hot} in the Carnot formula above) is the “average” temperature T_{hot} of the fluid during the heat input. It is defined as follows:

$$\text{Heat input} = \int_2^3 T dS = T_{hot} (S_3 - S_2) \quad (15)$$

Similarly, the “average” temperature T_{cold} of the fluid during its cooling is defined as follows:

$$\text{Heat removed} = \int_4^1 T dS = T_{cold} (S_1 - S_4) \quad (16)$$

In this case, where the fluid keeps the same phase and supposing its specific heat is constant, T_{hot} is the mean Log of T_2 and T_3 : $T_{hot} = (T_3 - T_2)/\ln(T_3/T_2)$. T_{cold} can similarly be approximated by $T_{cold} \sim (T_1 - T_4)/\ln(T_1/T_4)$. The efficiency of the cycle is improved by increasing the temperature of the working fluid during all the heat input. One way to achieve that is to design a cycle where the beginning/lowest temperature of the heat input is increased. In the example of Fig. 10, the heat input starts at a higher temperature due to a compression at a higher pressure; at the same time, expanding the air across a wider pressure ratio leads to a lower temperature T_4 , therefore to a lower T_{cold} . Both effects directly increase the cycle’s efficiency. There are several other ways to change T_{cold} and/or T_{hot} without changing the cycle’s minimum and maximum temperatures: a common way is to reheat the working fluid at the middle of the expansion. If the exhaust of the turbine is hotter than that of the compressor, a regenerative heat exchanger can also be used.

For all power plants, the highest temperature of the heat input (T_3 in Figs. 9 and 10) is always limited (through a techno-economic optimum) by material limitations and costs. Similarly, the pressure increase suggested in Fig. 10 is limited by the same material and cost considerations. Regarding CSP plants, specific issues may put a lower limit:

- The temperature may be limited by the storage medium itself (as it is the case today) or by corrosion issues if novel high temperature molten salts are used;
- Increasing the temperature results in an increase of the external wall temperature of the solar receiver. Most of the thermal losses of the receiver being radiant and therefore proportional to T^4 (T being the absolute temperature of the external wall), the thermal losses of the receiver may eventually offset the gain in cycle efficiency. In contrast, the radiant energy emitted by the heat exchangers of a combustion boiler is not lost.

Once an optimal value of the highest heat input temperature of the cycle is determined taking the above into account, the cycle efficiency can still be improved by raising the lowest heat input temperature (T_2 in Figs. 9 and 10). However, this means reducing the temperature range of the heat input ($T_3 - T_2$) by the same amount. The thermal storage of all commercial CSP plant works with sensible heat, with two tanks of storage medium at two different temperatures. Since the temperature of the hot medium is kept close to T_3 to avoid increasing the temperature of the receiver (see above), the temperature difference of the storage system $\Delta T_{storage}$ is closely linked to $T_3 - T_2$, and will decrease in a similar way. Therefore, increasing T_2 of the power cycle for a given T_3 has two negative consequences on a CSP plant:

- It increases the required amount of storage medium in inverse proportion with $\Delta T_{storage}$, with an obvious impact on the Capex (amount of medium and size of the tanks).
- The losses of stored heat during prolonged periods are increased (e.g., 3 K lost are 1% if $\Delta T = 300$ K but 2% if $\Delta T = 150$ K). This may be a minor drawback for big installations (with higher volume/external area ratios of the tanks) storing their heat for no more than a few days.
- The mass flow of heat transfer fluid (which is also the storage medium in a molten salt tower or the particle tower concept studied here) increases in inverse proportion with $\Delta T_{storage}$. A lower $\Delta T_{storage}$ means costlier pumping or handling systems and more parasitic consumption. This is significant for a molten salt tower, and a huge penalty for the particle tower (as shown in Section 11).

The issues related to the cooling temperature of the working fluid discussed below are not explicitly specific to CSP generation; however, they affect all power plants located in arid areas, which include CSP plants. Due to their need of high direct solar irradiation, CSP plants must be built in dry areas that are also hot in most cases. High water consumption is impossible or strictly regulated in such regions; should water be available nonetheless, the reliability of its supply would be doubtful over the plant’s lifespan. This eliminates once-through direct

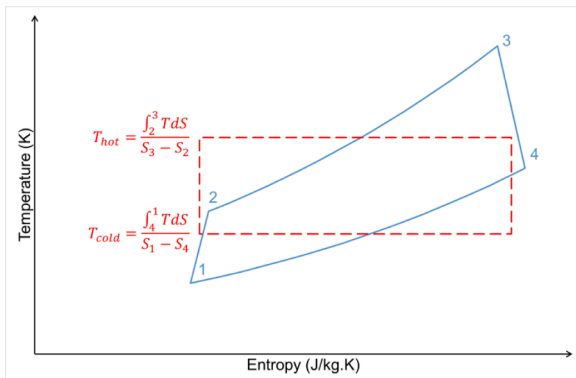


Fig. 9. Average temperatures of the heat input and cooling in a Brayton cycle. Solid blue: air Brayton cycle, dashed red: equivalent Carnot cycle.

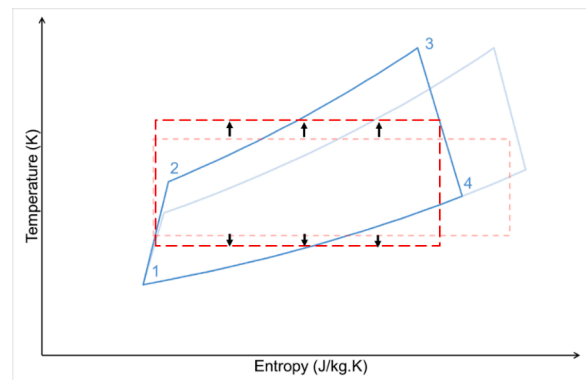


Fig. 10. Effect of increasing maximum pressure on the T-S diagram of an air Brayton cycle. Dark/light, solid blue: resp. high-pressure/low pressure air Brayton cycle; dark/light, dashed red: resp. equivalent Carnot cycles.

water cooling (no sea or big lake nearby) or wet cooling based on evaporation: only dry cooling can be reasonably envisioned. Putting aside the direct water cooling that is the cheapest and allows for the lowest and least variable cooling temperature, let us compare dry and wet cooling. Below are some brief reminders about the dry bulb and the wet bulb temperatures of the ambient air:

- 1) The dry bulb temperature T_{db} is the “usual” ambient temperature. The wet bulb temperature T_{wb} is the temperature obtained when adiabatically removing heat by evaporating additional water until saturation.
- 2) The difference $T_{db} - T_{wb}$ is zero when the air is saturated (relative humidity = 100%) and increases when the humidity decreases.
- 3) For a given specific humidity (mass ratio of vapor contained in the air), $T_{db} - T_{wb}$ increases when T_{db} increases, so that T_{wb} moves in the same direction as but less than T_{db} .

Consequently:

- Due to 2) above, T_{wb} is significantly lower than T_{db} in dry areas, and even more so in dry and hot areas because of 3).
- In given area, the specific humidity tends to be independent of the temperature over time. Therefore, according to 3) above, T_{wb} is less variable than T_{db} .

To summarize, in CSP-friendly areas, the dry bulb, “usual” ambient temperature that is the reference sink temperature for dry cooling is significantly higher and more variable than the wet bulb temperature that is the reference sink temperature for wet (i.e., evaporative) cooling. Besides, due to the low density and poor heat transfer properties of air at ambient pressure, dry cooling means a high final temperature difference in the cooling heat exchange (typically 15 K) and a significant parasitic consumption of the cooling fans. As will be shown below, all power cycles are significantly but not equally affected by dry cooling with respect to their efficiency.

5.2. Reference power cycle: Rankine steam cycle of a typical molten salt tower

The Rankine steam cycle of a typical molten salt tower has one reheat and typically 5 to 7 feedwater preheaters including the deaerator. A schematic diagram of the power cycle and its T - S diagram are shown in Fig. 11a and b. In the previous figures SH means superheater, RH reheater, and PH preheater. The PH 3 is the feedwater tank with the deaerator. Unlike the others, it is a direct contact preheater. The expansions shown in Fig. 11b are ideal (isentropic) whilst the real expansions are slightly tilted to the right so that the entropy increases.

As can be seen in Fig. 11b, the reheat allows increasing T_{hot} defined above (see Fig. 19) and limiting the final part of the steam expansion that takes place below the saturation curve (moisture is detrimental to expansion efficiency and causes blade erosion). The preheaters increase the starting temperature of the heat input, thereby increasing T_{hot} . The steam characteristics vary (e.g., the main steam pressure can be lower) but are typically as follows:

- Main steam at 120 to 170 bar/550 °C, and reheat steam at 550 °C;
- Feedwater temperature 210 to 260 °C, depending on the steam pressure, in order to allow for a salt return temperature of about 300 °C.

The temperatures of the main and reheat steam are of course determined by the maximum allowable bulk temperature (565 °C) of the salt that is universally used in commercial molten salt towers (NaNO₃-KNO₃ eutectic mixture), considering a reasonable 15 K final temperature difference in the superheater and reheater.

In conclusion, for a solar tower using the standard molten salt as

storage medium, the subcritical Rankine cycle described above is quite optimal. Only incremental upgrades (mainly of the efficiency of the turbomachinery) and therefore limited improvements are to be expected from the current “half-net” cycle efficiency¹: about 42.5% with an ambient temperature of about 35 °C, as determined below. A significant increase in cycle efficiency can only be expected from the integration of a novel power cycle. Several options are discussed below.

5.3. Supercritical steam cycles

If the storage medium allows for temperatures higher than 565 °C (which is the case with fluidized particles), the steam characteristics mentioned above can be improved, thereby increasing T_{hot} that is the prime parameter towards higher cycle efficiency, as explained above. As can be seen in Fig. 12, increasing T_{hot} is achieved by increasing the feedwater temperature, the main steam and reheat steam temperatures (T_3 and T_6), and the temperature of the evaporation plateau. The latter corresponds to increasing the pressure (pressure and temperature are linked in two-phase conditions). Increasing the pressure shortens the evaporation plateau (the latent heat decreases) until it is reduced to one point, namely the top of the saturation dome. This is the critical point: 221 bar and 374 °C. At pressures above 221 bar, there is no phase-change discontinuity; the water is a supercritical fluid whose isobaric heating path in the T - S diagram is an S-curve located above the saturation dome in the T - S diagram. Rankine Steam cycle with main steam at pressures above 221 bar are called supercritical cycles. The T - S diagram of a supercritical steam Rankine cycle is shown in Fig. 12 below. As in Fig. 11b, the expansion shown are isentropic whereas real ones are somewhat tilted to the right.

A second reheat is not uncommon on supercritical steam cycles: typically, on plants with moderate steam temperature (e.g., 540–565 °C) and low condenser pressure (direct water cooling in a cold area): without a second reheat, the expansion of the reheat steam would cross the saturation dome too early in the T - S diagram and its wet part would be excessive. However, due to their high condenser pressures inherent to dry cooling, future CSP plants with supercritical steam cycles do not strongly need a second reheat; besides, the added complexity seems difficult to justify with small-scale cycles that would suit CSP applications.

So far, supercritical steam cycles were developed for pulverized coal plants. A generally accepted classification of supercritical coal plants distinguishes supercritical (SC), ultra-supercritical (USC) and advanced ultra-supercritical (A-USC) steam cycles with the following hierarchy in terms of main and reheat steam temperatures and pressures, thus in terms of efficiency and material requirements: SC < USC < A-USC. That classification varies according to the entities (R&D centers, manufacturers, etc.); Table 5–1 below gathers ranges or typical values of steam pressure and temperature given by various sources. General Electric labels its “Steam H” generation as A-USC despite its main steam and reheat temperatures (650 °C/670 °C). For future CSP applications, USC cycles as defined in Table 5, or the lower end of A-USC cycles as defined by General Electric, are probably the right choice: steam pressure 25 MPa, superheated/reheated steam temperatures 600 °C/620 °C, with a potential objective of 30 MPa/650 °C/670 °C later. Higher steam pressures and temperatures are too far from technological readiness, and the gain in overall efficiency would not be as straightforward as with coal plants, because of the thermal losses of the solar receiver that depend strongly on temperature.

The commercial availability of small-scale supercritical steam cycles is an issue. In 2018, there were 226 USC units in operation in China, 22 in South Korea, 19 in Japan, 13 in Germany, and others in several other

¹ The cycle half-net efficiency is defined here as $\eta_{half-net} = \frac{P_{gross} - P_{FW,pump}}{Q}$ with P_{gross} the gross electric power of the cycle, Q the heat consumed by the cycle and $P_{FW,pump}$. It allows a fair comparison between cycles that use different heat sinks.

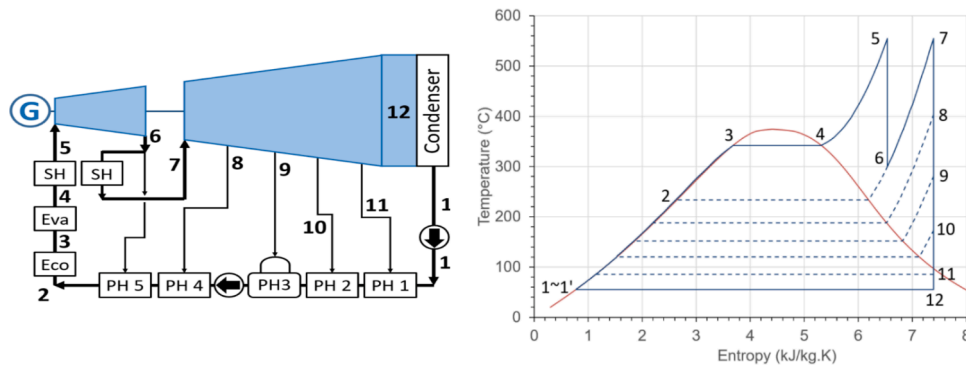


Fig. 11. (a-left): typical subcritical Rankine steam power cycle; (b-right): T-S diagram of the cycle.

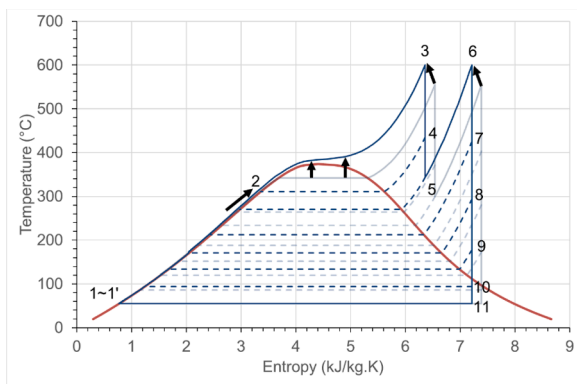


Fig. 12. Main changes from a subcritical (light blue) to a supercritical (dark blue) steam cycle on a T-S diagram.

countries. In contrast, there were no AUSC plants (with steam temperature ≥ 700 °C) in operation or even under construction in late 2018 [201].

The power output of USC turbines ranges typically from 600 to 1100 MW_e [204,208]; given the complexity of such plants, economies of scale can explain their size. Besides, there is a technological hurdle for small-scale supercritical steam power cycles. Due to steam density, the volumetric flow rate in the HP turbine of a small supercritical turbine is low, which translates into short blades with high flow rates leaking through the clearances, which affects the turbine's efficiency. An HP turbine rotating faster thanks to a gearbox is a possible solution.

That being said, small-scale supercritical steam turbines are gaining ground. The OECD introduced new financing rules in 2015 that required coal plants between 300 MWe and 500 MWe to be supercritical to benefit from attractive financing [208]. Today, Siemens proposes supercritical steam turbines of 250 MWe. General Electric proposes 300 MWe USC power cycles with steam (main steam pressure/main steam temperature/reheat steam temperature) at 30 MPa/600 °C/620 °C and 150 MW_e USC power cycles with steam at 25 MPa/600 °C/620 °C [207].

Table 5
Classification of supercritical coal power plants according to various sources.

	Unit	Sloss [201]	Wheeldon & Phillips [202]	IEA 2013 [203]	Nomoto [204]	Weiland and Shelton [205]	Nair and Kuman [206]	GE Steam Power [207]
SC	MPa	24.8	26.2	22.1–25.0	22.1–25.0	22.0–27.0	22.0–24.0	25.0
	°C	565–600	582	540–580	< 566 or 593	565–600	565–580	565
SC	MPa		24.8	27.6	22.1–25.0	25.0–30.0	24.0–31.0	25.0–34.0
	°C		≥ 600	604	580–620	600–640	595–620	SH 600 RH 620
-USC	MPa		27.6–34.5	35.2	25.0–35.0	30.0–35.0	24.0–35.0	> 34.0
	°C		700–760	700–725	> 700	700–760	> 705	SH 600–650° RH 620–670

In [15], the Electric Power Research Institute studies a 300 MW_e (gross) flexible Advanced Ultra-Supercritical (A-USC) Coal-Fired Power Plant that is downscaled from a reference advanced Ultra-Supercritical (USC) cycle currently proposed by General Electric. The authors consider that a power output of 300 MW_e is a reasonable minimum with the steam characteristics considered (last row of Table 6). The timescale of the commercial availability of supercritical power cycles (with power outputs appropriate for CSP applications) is summarized in Table 6.

5.3.1. Efficiency of a USC steam cycle integrated in a CSP plant compared to that of a benchmark subcritical cycle

In [209], 14 steam power cycles suitable for a molten salt tower were studied and their performances assessed and compared, with the following main characteristics:

- Gross power output 165 MW_e;
- Condensing pressure/temperature 15.2 kPa/54.3 °C, corresponding to an ambient temperature of 35 °C (or 40 °C with a very efficient air-cooled condenser);
- Steam characteristic ranging from 12.0 MPa/553 °C/553 °C to 26.0 MPa/580 °C/580 °C (same temperature for main steam and reheat steam).

In order to compare power cycle efficiencies, “half-net” efficiencies are considered, i.e., calculated after deducing only the electric consumption of the feedwater pumps from the power output. The benchmark cycle working with steam at 12.0 MPa/553 °C/553 °C has a gross efficiency of 43.2% and a half-net efficiency of 42.5%. After reprocessing the data obtained in [209] for the most advanced cycles, one can determine the performances of a cycle working with steam at 26.0 MPa/600 °C/600 °C: gross efficiency 47.0%, “half-net” efficiency 45.3%. Compared to the benchmark cycle, this is a 6.6% relative increase (+2.8 percentage points) in half-net efficiency, the one that matters. It allows reducing the thermal power of the solar island by 6.2%.

Table 6
Timescale for commercial availability of small-scale supercritical power cycles.

Power Output	Timeframe	Main Steam P	Main Steam T	Reheat Steam T
150 MW _e	Now	25.0 MPa	600 °C	620 °C
300 MW _e	Now	30.0 MPa	600 °C	620 °C
300 MW _e	Mid-term	33.0 MPa	650 °C	670 °C

5.3.2. Efficiency of an A-USC steam cycle integrated in a CSP plant

The main characteristics of the 300 MW_e (gross) power cycle studied and optimized in [Hack] (see above) are as follows:

- Main steam at 33.0 MPa/650 °C, reheat steam at 6.28 MPa/670 °C, no second reheat;
- Condensing pressure 3.9 kPa (temperature 28.4 °C), feedwater temperature of 330 °C;
- Gross efficiency 53.38% at full load, and “half-net” efficiency (i.e., deducing only the electric consumption of the feedwater pumps) 51.20%.

In order to be compared with those mentioned above, the performances of this power cycle must be reprocessed for a condensing temperature of 54.3 °C that was considered above for the benchmark and USC cycles. Assuming that the exhaust area of the low-pressure turbine is adjusted to keep the same exhaust losses [210], the gross efficiency decreases from 53.38% to 49.9%. The consumption of feedwater pumping remaining unchanged, the half-net efficiency is 47.7%. Compared to the benchmark cycle, this is a 12.2% relative increase (+5.2 percentage points) in half-net efficiency. It allows reducing the thermal power of the solar island by 10.9%.

5.3.3. Flexibility of USC and A-USC steam cycles for CSP applications

Since they are the sole application for supercritical steam cycles today, available data exist for pulverized coal plants only. The transients (ramp rate, start-up duration, etc.) are limited by both the boiler and the steam cycle, and it is generally not fully clear which one prevails. Besides, these plants are much bigger than CSP plants, and were generally built at a time when flexibility was not as crucial as today. Eventually, the definition of hot, warm and cold starts varies according to the authors.

Generally, the steam generators currently used in subcritical CSP plants feature a drum to separate steam from liquid water. This pressure vessel with its thick wall is the limiting component regarding transients. Supercritical steam generators are once-through: breaking them down into water preheater, evaporator, and superheater interconnected in series is no longer needed as the steam generator does not involve any phase change. The drum disappears, even though a steam separator system is still needed for start-up purposes, when the pressure is still below 22.1 MPa [209]. Therefore, a supercritical steam generator is likely to allow for faster transients than the subcritical ones currently used in CSP plants. As a result, the limiting component will be the turbine and possibly the high-pressure steam piping.

Ramp-up and load decrease rates (in % of full load per minute) including primary and secondary response capability, and minimum load operation (about 20% [15]) are relevant parameters regarding flexibility; however, for CSP plants that will be peakers, the hot start-up time is the most telling criteria. A hot start takes place within 8 h after shutdown according to [211], and 12 h after shutdown according to [212]. The duration of a hot start (until full load) varies significantly depending on the power plant and the definition of a hot start, but is approx. 1 hour to 2.5 h according to [212], and 90 min minimum for a 50 MWe supercritical plant according to [211]. Hack mentions 2 h for a hot start, but without precisely defining what a hot start is. Bedognist [213] defines a hot start with a maximum of 8 h after shutdown, then gives hot start-up times for three SC/USC pulverized coal plants:

- Belchatow II Unit 1 (Poland), completed in 2011, lignite-fired, 858 MW_e, 26.6 MPa/554 °C/582 °C: 140 min
- Walsum Unit 10 (Germany), completed in 2013, hard coal-fired, 725 MW_e, 27.4 MPa/600 °C/620 °C: 66 min
- Boxberg Unit R (Germany), completed in 2012, lignite-fired, 675 MW_e, 28.6 MPa/600 °C/620 °C: 80 min

All these data are given for pulverized coal power plants with bigger turbines than those envisioned for CSP applications; besides, their boiler might be the limiting component regarding transient capabilities. Price [214] envisions a hot start-up in as little as 25 min for a peaking molten salt tower that features a 230 MW_e (net) subcritical power cycle and a once-through steam generator whose purpose is precisely to allow for faster transients. Compared to the latter reference, the thicker piping and turbine casings of a supercritical power cycle are potential hurdles, but a hot start-up lasting 45 to 60 min until full load seems a realistic objective. Further studies are nonetheless required to provide a more accurate conclusion.

5.3.4. Materials for a USC/AUSC steam power cycle in a particle CSP plant

For a given steam temperature, the tubes of a particle-driven steam generator used in a CSP plant do not withstand the same maximum outer temperatures as those of a coal-fired boiler. Besides, unlike the combustion gasses in a coal-fired boiler, the particles on the outer side of the tubes are not corrosive. Therefore, regarding the material issues affecting a particle supercritical CSP plant, it is legitimate to focus more specifically on the turbine.

Advances on high-grade steels and nickel-based superalloys for the hottest parts dictate the current state-of-the-art of USC/AUSC coal power plants. The main hurdle to overcome are the deployment of such materials, their affordability, and the mass production of specialized equipment made of them [201]. The material used so far in power plants working at lower-temperatures and pressures do not have sufficient creep and corrosion characteristics. Significant advances were made and continue to be made regarding the materials required in the boiler and the turbine of supercritical coal plants. In the USA, the second phase of the ComTest project is currently under progress with completion due by the end of 2021 (deadline based upon January 2019). It aims at manufacturing and testing full-scale components for steam at 760 °C [215]. The long-term behavior (over the lifetime of a power plant) of some materials required in an A-USC plant must yet be validated.

The available material types for steam power plants depending on the temperature are shown in Table 7, with the materials specifically needed in USC and A-USC plants listed in the rightmost columns.

The most appropriate materials are component-dependent: casing of shells/valves/nozzles, bolts, rotors/discs, nozzles/blades, piping. They also depend on the temperature range. Zhang [202] and Nair and Kumaran [206] give lists of these materials for the abovementioned components with the following temperature thresholds: 565 °C, 593 °C, 620 °C, 700 °C, and 760 °C. All the high temperature components of an A-USC turbine must be made of Nickel-based alloys. Even for a plant whose steam temperature approaches 650 °C, a high-end Nickel-base alloy such as Inconel 740H is required for the highest temperature components [15].

5.4. Externally heated air combined cycle gas turbines

5.4.1. Main characteristics of fossil-fired combined cycle gas turbines

In most power cycles, the bulk of the lost exergy is generally destroyed in the hot source: the working fluid is heated at a much lower temperature than the theoretically available one (e.g., generally ≥ 2000 °C in a furnace, or the sun’s external temperature ~ 5700 °C for a CSP plant). As an internal combustion engine able to heat its working fluid at up to 1600 °C, fossil-fired gas turbines minimize these early second-principle losses. On the other hand, they release exhaust heat at temperatures higher than 400 °C (aero turbines) or 600 °C (industrial

turbines), which limits their efficiency to about 43%. Conversely, externally heated Rankine steam cycle (as those described above) have a quite inefficient hot source but an excellent isothermal (i.e., Carnot-like) heat sink at nearly ambient temperature. By connecting a gas turbine (topping cycle) with a Rankine steam cycle (bottoming cycle) that recovers its exhaust heat, one benefits from the best of both worlds. The output of the steam turbine is about 50% of that of the gas turbine. Efficiencies up to 64% are achieved in ISO conditions by state-of-the-art combined cycle gas-fired gas turbines [217]. In such installations, the gas turbine works with the highest possible turbine inlet temperature (TIT, that is, T_3 in Fig. 9 above: up to ~ 1600 °C) and its pressure ratio is adjusted (generally up to ~ 25) so that the exhaust temperature (T_4 in Fig. 9 above) is at 620–650 °C, which is convenient for heat recovery by the steam cycle. Due to the water evaporation plateau that creates a pinch in the heat exchange, a heat recovery steam generator (HRSG) producing steam at a decent pressure level (e.g. >12.0 MPa) would release flue gases at >200 °C. Therefore, in order to recover the low-grade heat and release the flue gasses at 85–125 °C, current HRSGs include three pressure levels (HP, IP, and LP). The Q-T diagram (heat exchanged vs. temperature from one end of the HRSG's gas path to the other) of a typical three pressure-reheat HRSG is shown in Fig. 13 below. Some heat exchangers shown in Fig. 13 are split to further minimize exergetic losses, so that 3P-RH HRSGs featuring about 15 heat exchangers are not uncommon. For a given pressure level (i.e., color), the horizontal line corresponds to the evaporator, the line on the right-hand side is an economizer, the line(s) on the left-hand side are superheaters.

5.4.2. Design specificities of an externally heated combined cycle gas turbine

With air as working fluid, an externally heated gas turbine raises much less corrosion issues than supercritical steam or CO₂ power cycles. Besides, whatever the power cycle, no corrosion affects the particle-side of the primary heat exchanger(s) whilst combustion gas (in a coal plant) or molten salt (in a benchmark solar tower) are corrosive. Eventually, pressures are about 10 times lower. Therefore, the allowable TIT is higher than that of a sCO₂ or an A-USC steam turbine. That being said, a TIT of, e.g., 900 °C (a quite aggressive target) is no match with that of a fossil-fired gas turbine, even one with an old design. However, with proper design of the gas turbine, a combined efficiency approaching 50% is feasible, which makes the concept a competitive option compared with supercritical steam or CO₂ cycles.

In order to maximize the combined cycle efficiency, both the

Table 7
Available material types for steam power plants. Sources: [206,216].

T range	≤ 420 °C	420–620 °C	620–680 °C	≥ 680 °C
Grades	Low alloy ferritic steels	Ferritic creep-resistant steels	Advanced Austenitic Stainless steels	Nickel-based alloys
Examples	T/P22, T/P23, T/P24	T/P91, T/P92, T/P122	304H, 316H, 347H, Sanicro25	Haynes 230,
Main contents	2% Cr, small amounts of other components	9% to 12% of Cr, and small amounts of Mo, V, Nb	18%Cr-8%Ni; 16%Cr-12%NiMo; 18%Cr-10%NiNb; 22%Cr-25% NiWCuNbN	Inconel 617 Inconel 623 Inconel 740, etc.
Merits	welding, strength, oxidation	Oxidation	creep, corrosion	
Drawbacks	Creep	welding, production time	High thermal expansion, sensitization to intergranular corrosion, stress corrosion cracking in wet environment	Cost

externally heated and the gas-fired gas turbines are coupled with the same bottoming cycle, namely a three pressure reheat steam Rankine cycle (an example of its Q-T diagram is shown in Fig. 13). Its main characteristics are typically: HP steam: 16.0 MPa, 585 °C, reheat steam: 3.0 MPa, 585 °C, LP steam: 0.3 MPa, stack temperature: 85 °C. The heat recovery rate of the steam generator is $\sim 89\%$ and the compound (HP + IP + LP) efficiency of the cycle is about 35%.

The respective designs of the gas-fired and externally heated gas turbines differ, beyond the fact that the latter lacks combustors and all the related hardware (piping, valves, etc.).

The schematic and T-S diagram of a double reheat gas turbine are displayed respectively in Figs. 14 and 15. Let us consider a fictitious no-reheat gas turbine operating with the same TIT (i.e., value of T_3 , T_5 , and T_7 in Fig. 15) and the same exhaust temperature T_8 that is a good value for combined cycle operation. Its cycle (using the dotted isobaric line in Fig. 15) is 1→1.5→(6)→7→8→1, with a lower pressure ratio (hence the compression ending at “1.5”). The only components that remain are an initial section of the compressor, the third heat input, and the last expander.

As it appears clearly in Fig. 15, the “average” temperature (as defined at the beginning of this section) of the three reheats (2→3 + 4→5 + 6→7) is higher than that of the single reheat 1.5→7. In conclusion, for given turbine inlet and exhaust temperatures, the theoretical efficiency of a gas turbine increases with the number of reheats. However, this must be tempered for real cycles. Due to their high TIT, gas-fired gas turbines require a substantial mass flow rate of cooling air to be extracted from the compressor, then re-injected in the first stage (the hottest one) of the expander; this is detrimental to the efficiency. Adding reheat(s) means extracting more cooling air, which more than offsets the gain with very high TITs, so that last generation reheated turbines no longer exist. Due to their low TIT, externally heated gas turbines are uncooled, which makes the aforementioned downside of reheat(s) irrelevant; however, each heat input is done by a heat exchanger with a significant pressure drop to which Brayton cycles are very sensitive. Therefore, one or maximum two reheats is in practice the best trade-off. With reasonable assumptions regarding pressure losses, the best combined cycle efficiency is obtained with one reheat configuration when $TIT \geq 900$ °C, and with two reheats when $TIT \approx 800$ °C [218].

5.4.3. Current status of the studies of externally heated gas turbines

Externally heated gas turbines were already studied, with diverse configurations (open, recuperated, or combined cycle, with or without intercooled compression, with or without reheat(s)), and for various potential applications: CSP, nuclear, external firing with coal or biomass, etc. In 2012, Barigozzi et al. [219] presented a method predict the design and off-design performance of a hybrid open-cycle gas turbine through detailed modeling (“hybrid” means that the turbine features a supplementary combustion). In 2013, Sanchez-Organ et al. [220] performed the thermodynamic optimization of a regenerative, intercooled and reheated gas turbine with a solar-only heat input, without

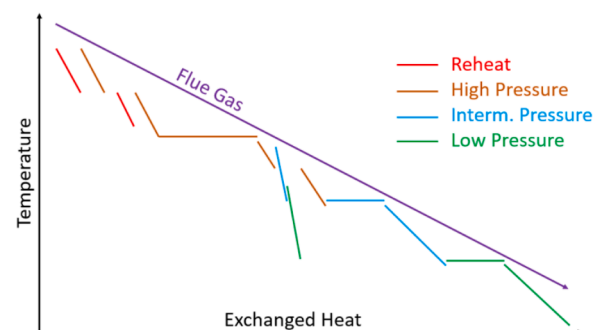


Fig. 13. Typical flue gas/steam cycle temperature profile for a three pressure reheat HRSG.

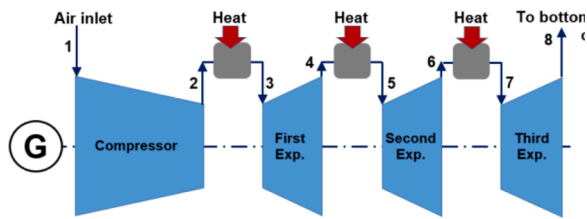


Fig. 14. Schematic of a double reheat gas turbine, adapted from [218].

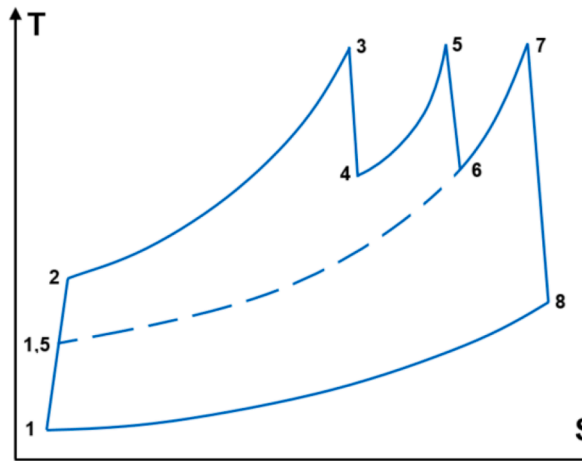


Fig. 15. Temperature-entropy diagram of the double reheat gas turbine shown above.

storage. In 2014, Andreades et al. [221,222] proposed to modify commercial gas turbines for solar or nuclear applications, the heat input being performed by high temperature molten salt (thus allowing for thermal storage) plus optional hybridization. In 2015, Al-Attab et al. [223] reviewed the existing externally fired gas turbines with specific emphasis on the high temperature heat exchangers and had previously tested (in 2009) a biomass-fueled micro-gas turbine focusing on the heat exchanger's efficiency [224]. Siros et al. in 2017 [218], then Valentin et al. in 2018 [17] described the optimization of a solar-only, low TIT combined cycle gas turbine with the purpose of its integration in a solar tower power plant using particles as storage medium. Zaversky et al. [225] analyzed the potential performances of solar-driven combined cycle gas turbines; the topping gas turbine is indirectly heated by an atmospheric air receiver through a regenerative heat exchange system. A techno-economic study of this concept was then done in [226], concluding that the LCOE of this concept is higher than that of a regular Rankine steam cycle, despite a higher efficiency. Many of the publications (including others than those mentioned above) consider direct air heating through a pressurized solar receiver, which does not realistically allow for significant thermal storage: full dispatchability is generally allowed by a supplementary combustion that also increases the TIT in solar operation when installed downstream of the solar receiver. The pressure losses of the loop that heats the working air are often subject to optimistic assumptions.

5.4.4. Efficiency of an externally heated gas turbine with a TIT of 780 °C

A TIT not exceeding 800 °C seems a reasonable hypothesis to mitigate the heat losses of the solar receiver and to avoid the need for the costliest superalloys. According to [17], a net efficiency of 48.6% can be achieved under realistic (and even slightly conservative) assumptions with a TIT of 780 °C and a condensing temperature of 45 °C, with a double reheat configuration. To ensure a fair comparison with the supercritical steam and CO₂ cycle described above, this figure is reprocessed as follows. Firstly, adding the power consumption of the air-cooled

consumption (1.4 MW_e) to the net power output (161.0 MW_e) results in a half-net efficiency of 49.0%. Then, raising the condensing temperature from 45 °C to 54.3 °C results in a half-net efficiency of 47.7%. This is the efficiency of the A-USC steam cycle with main/reheat steam at 650 °C/670 °C under the same conditions (see above).

It should be noted that the TIT of 780 °C considered above is close to the minimum acceptable; should it decrease below this value, the resulting efficiency would drop very quickly, thus making the externally-heated combined cycle pointless.

5.4.5. Flexibility of externally heated combined cycle gas turbines for CSP applications

A modern gas turbine can, if necessary, reach full load from a cold start-up in about 20 min. It never limits the flexibility of a combined cycle whose transient capabilities are therefore those of its steam cycle. In general, HRSGs (always subcritical so far) feature a drum for each pressure level to separate steam from liquid water. Due to its thick wall, the high-pressure drum is the limiting component regarding transients. However, Benson® HRSGs with a once-through – i.e., drum-less – HP circuit allow for faster transients: a hot start lasts typically 50 min from gas turbine start-up to combined cycle full load [227]. Benson® HRSGs have been commercially available for at least two decades.

5.4.6. Technological readiness of externally heated combined cycle gas turbines

The advanced dry low NO_x burners of state-of-the-art gas-fired gas turbines are cutting-edge technology that disappears from an externally heated gas turbine. The heat exchangers that replace the combustion are studied in Section 4. A double reheat gas turbine would be a first-of-a-kind at industrial scale. However, a single reheat gas turbine has been on the market since 1995: the Ansaldo (ex-Alstom ex-ABB) GT24/GT26 (the former in its 60 Hz version, the latter in its 50 Hz version) that was very successful [228]. Therefore, the double should not constitute any major technological risk. The maximum temperature of the turbine's hot parts is necessarily lower than that of the particle-air heat exchangers and *a fortiori* than the external temperature of the solar receiver's tubes. Using a high grade Nickel-based alloy for the turbine's hot components (notably its blades) will suffice: no internal cooling and no thermal barrier coating are required. To summarize, despite its double reheat layout, the externally heated gas turbine should be easier and cheaper to design and manufacture than a gas-fired turbine. The bottoming cycle is exactly the same as that of a gas-fired combined cycle equipped with a Benson® HRSG.

The combined requirement of relative low pressure drops and small temperature differences results in bulky and therefore expensive particle-air heat exchangers. This is especially true for the low-pressure heat exchangers. In practice, several heat exchangers in parallel are necessary for each pressure level, which makes air piping and particle handling more complex (see Section 11).

In case of a turbine trip (unexpected disconnection from the grid), a gas-fired gas turbine avoids over speeding by immediately closing the gas valve; with an externally heated turbine, due to the inertia of the heat exchangers, the hot air must be safely diverted within a split-second; this must still be validated with a utility-scale turbine.

Considering all the above, designing and manufacturing the externally heated combined cycle considered in this study, including the particle-air heat exchangers, should not raise any major challenge. The main hurdle would rather be to convince a manufacturer to build the gas turbine.

5.5. Supercritical CO₂ (sCO₂) Brayton cycles

Gas turbines work in compliance with a Brayton cycle (shown in Fig. 19) that uses a quasi-ideal gas as working fluid (namely air). In a typical industrial internal combustion gas turbine, the compression consumes about half of the work released by the expansion.

Consequently, the net specific work of the cycle (expansion work minus compression work per unit of mass flow of working fluid) is very sensitive to component efficiencies (pressure losses and turbomachinery efficiencies). This in turn penalizes the cycle efficiency and is exacerbated by the moderate TITs allowed by external heating (as opposed to TITs up to 1600 °C allowed by internal combustion with proper cooling of the hot path). Besides, due to the low density of atmospheric air, recuperative cycles (where the exhaust heat is partly recovered to pre-heat the working air after compression) are not realistically feasible on utility-scale units. Combined cycle configurations, where a bottoming steam cycle uses the exhaust heat, are described in the previous chapter.

Using CO₂ as working fluid mitigates these shortcomings: its critical temperature is 31.0 °C, which is generally close to the available heat sink temperature. The CO₂ that enters the compressor, though not in its liquid phase, is close to its critical point, which means high density and low compressibility. Consequently, the compression work is low, thereby increasing the net specific work of the cycle and lowering its sensitivity to component efficiencies. Besides, due to its critical pressure (7.38 MPa), the density of the CO₂ remains high throughout the cycle, thereby allowing for efficient recuperative heat exchangers with little penalty in terms of relative pressure drops. High recuperation rates – corresponding to low pressure ratios – mean higher average hot source temperature T_{hot} as described in Fig. 19 and thus higher efficiencies.

As a result, sCO₂ cycles allow for good or very good efficiencies at moderate TITs, even though steam Rankine cycles (that pump water with even less work consumption) remain unbeatable at low TITs (a tentative comparison is proposed below). Unfortunately, the two characteristics that contribute to this efficiency – namely, compressing the working fluid near its critical point and being highly recuperative – are also significant hurdles for CSP applications:

- Even though the conjunction of cold weather and high direct irradiation is conceivable in some sites (probably elevated ones), CSP-friendly areas are generally hot and arid. Dry cooling combined with high ambient temperature result in compressor inlet temperatures (i.e., the lowest CO₂ temperature of the cycle) that are much higher than the critical temperature of CO₂ (31.0 °C). With such temperatures, the benefit of low compression work – maximum when the compressor inlet temperature is just above 31.0 °C – almost disappears. Consequently, in terms of efficiency, Brayton sCO₂ cycles suffer much more from poor cooling conditions than steam cycles whose efficiency only decreases according to the Carnot principle. One must keep in mind that, when comparing the respective efficiencies of Brayton sCO₂ cycles and Rankine steam cycles, the temperature of the heat sink is almost as important as that of the heat source.

The impact is even worse on power output, when the compressor inlet temperature increases starting from just above 31.0 °C, at first the compressor rpm increases and/or its inlet guide vanes open to keep the same CO₂ mass flow. But when the temperature further increases and the rpm and/or the IGV opening have reached their maximum, the mass flow decreases, and the power output decreases more than the efficiency.

- Being highly recuperative, sCO₂ cycles have a usually narrow temperature range of the heat input; in a CSP plant, the temperature difference (ΔT) of the storage system will be similarly narrow. When only sensible heat is used, with roughly constant heat capacities, the inventory of storage medium and the mass flow rate of the heat transfer fluid are inversely proportional to ΔT . Consequently, a narrower ΔT means more Capex and more parasitic consumption for pumping/handling the heat transfer fluid. Besides, the thermal losses of the solar receiver increase because its average temperature is higher for a given maximum temperature.

Specific layouts of sCO₂ cycles can mitigate these two drawbacks, but with some negative impact on the efficiency. This caveat is sometimes overlooked by some publications studying sCO₂ cycles integrated in CSP plants with a compressor inlet temperature of, e.g., 32.0 °C.

5.5.1. Overview of the various sCO₂ cycles – best candidate for CSP applications

The earliest reference on sCO₂ cycles acknowledged in the literature is a Swiss Patent filed by Sulzer in 1948 on a partial condensation CO₂ Brayton cycle. Cycles using CO₂ as working fluid were then studied in several countries in the 1960s, the papers released by Angelino in Italy [229] and Feher in the US [230] being among the most notable. In 2004, Dostal et al. did an extensive study of the supercritical CO₂ cycles [231]. Although it mainly focuses on nuclear power applications, this study is still a reference regardless of the application envisioned. Several review papers (mentioned below), as well as a book edited by Brun et al. [198], were released since then.

Due to the strongly non-linear behavior of CO₂ around its critical point and the overall low maturity of sCO₂ applications, there is less consensus on the “optimal” designs of sCO₂ cycles than on water/steam cycles that benefit from 250 years of continuous development. Variants are therefore very numerous, so that dedicated literature reviews proved necessary to compare their merits. Amongst other studies, Ahn, Crespi and Yin [232–234] provide an overview of most if not all the layouts that were devised, the last two publications being focused on CSP applications. Most of the cycles mentioned in these papers are Brayton cycles in which the fluid remains above the saturation dome. In some cycles, the temperature of the working fluid goes below the critical temperature (31.0 °C), the main compressor being replaced by a pump and the cooler by a condenser: these are transcritical Rankine CO₂ cycles (note that the supercritical steam cycles should rather be referred to as transcritical). In [233], Crespi classifies the cycles according to their layout regardless of them being trans- or supercritical. However, transcritical cycles can be discarded from this overview that is dedicated to CSP applications since they need a compressor inlet temperature substantially lower than the critical temperature to make sense from an efficiency standpoint: typically ≤ 15 °C, which corresponds to an ambient temperature lower than ~ 5 °C with dry cooling.

The simple recuperative cycle must obviously be preferred to the simple cycle, but carries a major drawback regarding the recuperative heat exchange that is pictured in the Q - T diagram shown in Fig. 16. Near the cold end of the heat exchanger, the cold CO₂ path (in blue) is close to the critical point, hence an increasing specific heat that corresponds to a lower slope of the blue line. Conversely, the hot path is at a higher pressure that keeps it away from the critical point, hence the almost constant specific heat and slope of the red line. This mismatch between the two specific heats causes a pinch at the cold end of the heat exchanger that translates into a high temperature difference along most of the heat exchange, even for a (theoretical) infinite exchange area. This irreversibility has a major impact on the cycle efficiency.

The remedy consists in splitting the recuperator into a LTR and a HTR (low and high temperature recuperators) – and diverting part of the mass flow away from the LTR, so that the lower mass flow going through it compensates for the higher specific heat. The most prevalent layout that implements that is the recompression layout. Its schematic and T - S diagram are shown in Fig. 17.

Based on the studies carried out by Angelino, Dostal et al. compared in [232] the following cycles based on their efficiency: pre-compression, recompression, partial cooling cycle, and partial cooling cycle with improved regeneration. One must keep in mind that Angelino studied transcritical cycles; with a supercritical cycle, the improved regeneration proposed for the partial cooling layout becomes irrelevant. The authors conclude that:

- The recompression cycle (shown in Fig. 17) is the most efficient for turbine inlet pressures higher than approx. 20 MPa (which is the general situation);
- The efficiency of the partial cooling cycle (shown in Fig. 18) is almost independent of the turbine inlet pressure; as a consequence, the partial cooling cycle becomes more efficient than the recompression one when the turbine inlet pressure goes below approx. 20 MPa.

The cycle layouts deemed most appropriate for CSP vary according to the publications released since the early 2010s. It is the recompression cycle (amongst 12 layouts without reheat) according to Ahn et al. in [232]. LCOE considerations led Crespi et al. to prefer the Allam cycle and the Partial Cooling cycle, both without reheat. However, the Allam cycle considered is transcritical with a minimum CO₂ temperature of 20 °C, which greatly limits its potential for CSP.

Neises and Turchi compared in [235] the relative merits of the recompression and partial cooling cycles, both with reheat. A compressor inlet temperature of 50 °C – slightly conservative, even for CSP – was considered. When using a heat exchanger effectiveness model (as was generally the case in previous studies), the efficiencies of both cycles are similar. However, the authors characterized the recuperators by their conductance (in W/K) which is a better proxy for their size and cost, and concluded that the partial cooling cycle is more efficient until high values of recuperator conductance are considered. Other aspects favor the partial cooling cycle. The wider temperature range of the heat input is a significant plus for CSP, as explained above. The partial cooling cycle is almost unaffected by lowering the turbine inlet pressure, e.g., from 25 to 20 MPa, unlike the recompression cycle. In another study by the same authors [236], the LCOE of molten salt towers using simple recuperative, recompression, and partial cooling cycles (this time without reheat) are compared. The turbine and compressor inlet temperatures are 630 and 45 °C respectively. The minimum LCOE with the partial cooling cycle is 6.2% lower than that with the two other cycles. In the comparison with the recompression cycle, the reason is the wider temperature range of the heat input compared to that of the recompression cycle (hence cheaper storage, less receiver thermal losses, and lower parasitic consumption to pump the molten salt, as explained above). As for the simple recuperated cycle, it is penalized by its lower efficiency. This study confirms the conclusions drawn from the previous one.

In [237], Binotti et al. compared three non-reheat sCO₂ power cycles integrated in a solar tower system with TITs up to 800 °C: recompression cycle, partial cooling cycle, and recompression with main compression intercooling (RMCI). The latter is similar to the partial cooling cycle, but with the bifurcation before the first cooling rather than after the first compression. The ambient temperature considered is 40 °C. The final comparison criterion is the solar-to-electric efficiency that factors in cycle efficiency, thermal losses of the solar receiver, and auxiliary consumption (including salt pumping and cooling fans). It is 24.5% (with a

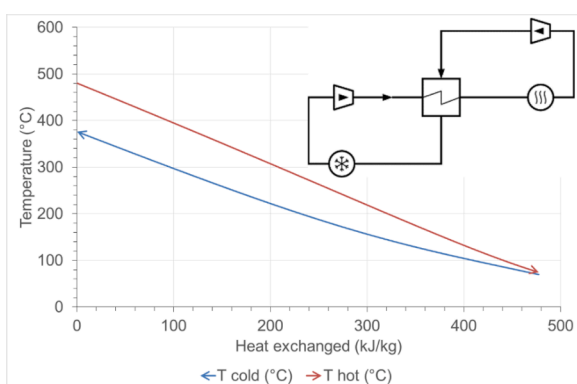


Fig. 16. Q-T diagram and schematic (top right) of a simple recuperated cycle.

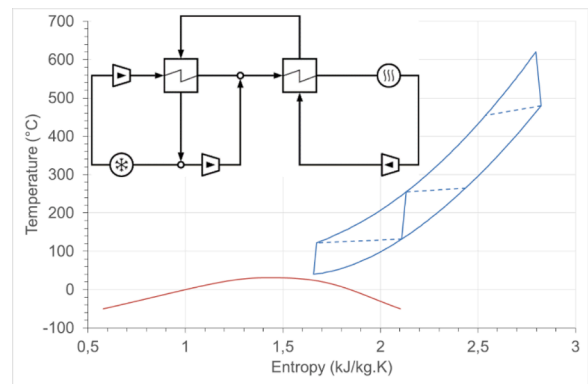


Fig. 17. T-S diagram and schematic (top left) of a recompression sCO₂ Brayton cycle.

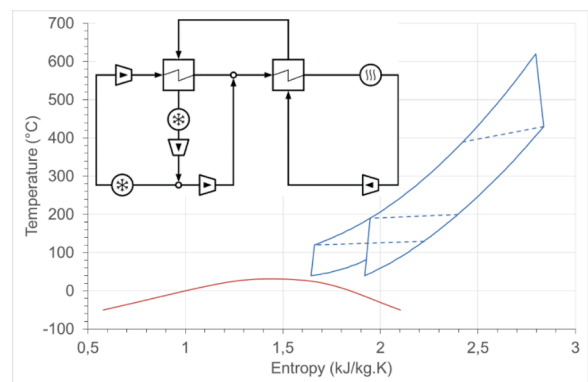


Fig. 18. Partial cooling sCO₂ Brayton cycle.

cycle gross efficiency of 48.6%) with the RMCI cycle, obtained with a TIT of 750 °C; it is similar (0.4% lower) with the partial cooling cycle (obtained with TIT = 780 °C) and 3.9% lower with the recompression cycle (obtained with TIT = 740 °C). Being as efficient as the partial cooling cycle with a lower TIT, the RMCI cycle wins. Comparing these two cycles using a conductance model (that should be more representative than effectiveness) for the heat exchangers would be interesting.

Adding a reheat improves the efficiency by about 1.5% point (i.e., ~3%), as shown by Mecheri and Le Moulec [238]. However, a reheat does not seem optimal for CSP. The turbine inlet pressure is limited for feasibility and cost reasons and the exit pressure must be higher than the critical pressure (or reasonably lower for partial cooling or intercooling cycles); this limits the turbine overall expansion ratio and the corresponding temperature drop. Splitting the expansion with a reheat also splits this temperature drop, thereby lowering the temperature range ΔT of the heat input (this is why the reheated cycle is more efficient). As explained above, a lower ΔT is not welcome for CSP applications.

The seven studies mentioned above provide a good insight of the most appropriate power cycles for CSP applications, even though many other studies cover the subject. The partial cooling cycle seems to be the best choice for CSP, but it should be further compared with the recompression cycle with main compression intercooling to reach a final decision.

5.5.2. Existing power sCO₂ power cycles or experimental loops today

Table 8 gathers the known projects with a power output of 100 kW_e or above that are being or were already demonstrated and tested (except the 10 MW_e STEP project that is still underway). The three first projects mentioned are the commercially relevant demonstration systems [239], the others being primarily R&D loops.

- Net Power is a 50 MW_{th} (~25 MW_e) internal oxy-combustion/Allam cycle plant that was first fired on 30 May 2018 [217]. The CO₂ produced by the combustion is the working fluid and is pipeline-ready (thanks to its pressure) for CO₂ capture. Water – the other combustion product – is removed once condensed. However promising, this concept is not applicable for CSP.
- Echogen is the closest to commercialization. Its target application is waste heat recovery where cycle efficiency, but also heat recovery rate matter. The company favored layout simplicity and compactness, the main objective being to replace organic Rankine cycles.
- The STEP demonstration plant aims at becoming the largest indirectly gas-fired sCO₂ power plant, expected to be tested from January 2021 to September 2022 (pre-Covid schedule). Its design allows for operation first in simple recuperated mode at 500 °C, then in recompression mode up to 715 °C [240]. It benefits from lessons learned from the Sunshot 1 MW_e test loop.

Smaller experimental loops (< 100 kW_e, hence not mentioned in Table 8) are being or were already tested:

- In Asia, in the Korea Institute of Energy Research and in the Tokyo Institute of Technology;
- In Europe: in TU Wien in Austria, in the Research Center Rez in Czech Republic, and within the following projects funded by the EU's H2020 program: sCO₂-HeRo, ITHERM, and sCO₂-Flex. In the latter, critical components are being tested separately.

It is generally acknowledged that an electric power output of at least ~10 MW_e is necessary for an experimental loop to be representative of the future challenges to be met by future utility-scale sCO₂ power cycles [232]. Some challenges encountered with most test loops are specific to small turbomachinery and therefore not relevant for future utility-scale power cycles: notably, the issues (especially the impact on performances) affecting the thrust and radial gas-foil bearings needed for this scale of turbomachinery [232]. Conversely, the solutions developed for the bigger STEP turbomachinery regarding seals and bearing (e.g., hydrostatic bearings with hermetic turbomachinery that do not need seals, hydrostatically-assisted gas foil bearings, etc.) are potentially scalable. Depending on the experimental loop, the arrangement of compressor(s), turbine, generator, and electric motor if applicable varies (decoupled or on the same shaft). The compressors and turbines are generally radial (including on Echogen); the turbine of Net Power, STEP, and Sunshot is axial.

5.5.3. Efficiency

Assessing the efficiency of supercritical Brayton CO₂ cycles – let alone comparing it with that of steam cycles – is difficult, mainly for the following reasons,

- Accurately predicting, for a future utility-scale plant, the efficiency of the turbomachinery (particularly the main compressor that works close to the critical point) is uncertain.
- Many variants of sCO₂ cycles exist, and the best choice for CSP applications depends on several criteria beyond the sole cycle efficiency at design point.
- As explained above, sCO₂ cycles are much more sensitive to the heat sink temperature than steam cycles; this must be taken into account to ensure a fair comparison whose conclusion will depend on the ambient temperature.

Amongst the many studies that included the determination of the efficiency of one or more cycle configurations, a representative selection is proposed in Table 9. A table summarizing the efficiencies obtained from other studies [241]. It complements Table 9 but does not mention the compressor inlet temperature.

Table 10 gives an estimate of the influence of the compressor inlet temperature on the cycle efficiency. Please note that the variations of efficiency mentioned are in relative %: for example, an efficiency decrease from 50% to 49% (one percentage point) means 2%.

The impact of a CIT increase on the efficiency drawn from [198,238] are design values; in other words, the design of the cycle is CIT-dependent. Conversely, the impact determined in [253] is off-design. Its lower value can be explained by 1/ an active control of the low-pressure side of the cycle depending on the CIT, 2/ the higher CIP that is beneficial with higher CITs, even though it penalizes the efficiency when the CIT is close to 31.0 °C. Besides, the partial cooling cycle and probably the intercooling cycle (that seem a better fit for CSP than the recompression cycle) are known to be less sensitive to the compressor inlet temperature than the recompression cycle considered in Table 10. In view of these results, to extrapolate efficiencies from values obtained with 32 °C or 33 °C to higher CITs, applying a penalty of 0.50% (relative %) per Kelvin seems reasonable. This rule of thumb was used to recalculate the efficiencies drawn from Table 9 for inlet temperature of 45 °C and 51 °C that are typical for CSP. Table 11 gathers the results obtained; only studies with TITs ≥ 600 °C were kept, and the RMCI cycle in [237] was removed because it somehow duplicates with the PC cycle. The A-USC cycle studied above was inserted in the Table as a comparison basis; the condensing temperature replaces the compressor inlet temperature, and the “half-net” efficiency of 51.20% drawn from [15] was readjusted for condensing temperatures of 45 and 51 °C using the same method as above.

According to this tentative comparison, the efficiency of the sCO₂ cycles are generally not higher than that of a A-USC steam cycle for similar TITs (resp. 650 and 670 °C for the main steam and the reheat steam). It is only significantly higher in two studies: in [237], but with a much higher TIT; and in [235], even subtracting ~1.5 percentage point to account for the reheat that is not convenient for CSP, as explained

Table 8
sCO₂ experimental loops with a power output ≥ 100 kW_e Source: [241,242], Acronyms: RE = simple recuperated, RC = recompression.

Name	Ref.	Power (kW _e)	Cycle	Temp. (°C)	Pressure (MPa)	Main partners	Location
Net Power	[217, 243]	25,000	Allam	1150	30.0	Net Power, Toshiba	La Porte, TX (USA)
Echogen	[244]	8000	RE	485		Echogen Power Systems	Akron, OH (USA)
STEP	[240]	Up to 10,000	RE/RC	715	25.0	Gas Technology Institute, SwRI, GE Global Research, GE-Baker Hughes	San Antonio, TX (USA)
Sunshot	[245, 246]	1000	RE	700 °C		General Electric, Southwest Research Institute	San Antonio, TX (USA)
SNL	[247]	125	RC	537	17.0	Sandia National Laboratory, Barber Nichols	Albuquerque, NM (USA)
PTT	[248]	50–250	RC	750	42.3	Peregrine Turbine Technology, Carleton University	Ottawa, Canada
IST	[249]	100	RE	299		Bettis Atomic Power Lab., Bechtel Marine Propulsion	West Mifflin, PA (USA)
SCIEL	[250]	300	RE	500	20.0	Korea Adv. Inst. of Science & Technology, Korea Atomic Energy Research Institute	Daejeon, Korea

Table 9

Efficiencies provided in the literature.

TIT/TIP/ CIT = compressor/turbine inlet temperature/pressure, SR = simple recuperated cycle, RC = recompression cycle, PC = partial cooling cycle, RMCI = recompression cycle with main compressor intercooling, RH = reheat, and UA = conductance.

Ref.	Reference	TIT °C	TIP MPa	CIT °C	PowerMW _e	Remarks	Layouts
[235]	Neises	650	25.0	51.0	35	UA recuperators = 10 MW/K (other UAs also considered) Value drawn from bar-chart	RC with RH 50.39%
[232]	Ahn	500	25.0	32.0			PC with RH 51.21%
[237]	Binotti	750	25.0	51.0	25		RC ~43.8%
							RC 46.9% PC 48.7%
							RMCI 48.6%
[233]	Crespi	550	25.0	32.0			RC 46.5% PC 46.1%
		750	30.0				RC 50.6% PC 51.1%
[251]	Luu		25.0	32.0		From chart (efficiency vs. TIT) with 500 °C ≤ TIT ≤ 850 °C	RC 600 °C 48.1%; 700 °C 52.5%
[252]	Alfani	620	25.0	33.0	100	Results shown for best effic. vs. thermal inertia trade-offs	RC. 42.4% to 43.9%
[236]	Neises	630	25.0	45.0	115	UA recuperators = 30 MW/K (other UAs also considered)	RC 47.6% PC 47.4%

Table 10

Relative variation of efficiency as a function of the CIT.

Ref.	reference	Cycle	TIT °C	TIP MPa	CIP MPa	CIT °C	Efficiency change due to CIT change	Relative efficiency of variation / +1 K @ CIT
[198]	Brun	SR	700	34.5	7.93	35→40	44.00%→42.66%	-0.61% / Kelvin
[198]	Brun	SR	600	34.5	7.93	35→40	40.74%→39.07%	-0.82% / Kelvin
[238]	Mecheri	RC/2RH	620	20.0	8.0	35→45	46.56%→43.81%	-0.59% / Kelvin
[253]	Dyreby	RC	700	25.0	9.17	35→55	51.47%→46.87%	-0.45% / Kelvin

above. A comparison with the efficiency calculated by the same authors five years later in [236] suggests that the modeling may have been somewhat optimistic.

To summarize, based on current knowledge and with heat sink temperatures generally allowed by CSP-friendly sites, the efficiency of sCO₂ cycles is, at best, similar to that of A-USC steam cycles. Given the deviation shown in Table 11, it is not possible to draw more accurate conclusions.

These results are rather consistent with conclusions obtained in previous studies: in [231], Dostal et al. state that 1/ the efficiency of sCO₂ cycles increases more with the TIT than that of steam cycles, 2/ the threshold where sCO₂ cycles becomes more efficient is 550 °C compared to supercritical steam cycles, and 470 °C compared to subcritical steam cycles. However, this comparison was done in 2004 with USC (not Advanced USC) steam cycles, and the compressor inlet temperature was 32.0 °C. With A-USC cycles and dry cooling with hot ambient temperatures, a threshold of about 700 °C seems more realistic.

5.5.4. Flexibility

Flexibility is often mentioned as a key potential merit of sCO₂ cycles for CSP plants that are intended for daily start-up/shutdown cycles. Higher flexibility allows wasting less energy and better meeting the needs of the grid during these transients. Several studies propose dynamic analyses of sCO₂ cycles integrated in a CSP plant, although it is not always clear if truly transient or quasi-steady-state simulations are performed. Marchionni et al. [254] studied a 1-D transient model based on the major components of Brunel University London's test facility,

namely, a simple regenerative 50 kW_e sCO₂ power cycle. Start-up, shut down and heat input variations were studied, and the control system (including turbine by-pass and CO₂ inventory) was optimized. Due to the application targeted (waste heat recovery from industrial flue gas) and the power scale, the conclusions of this study seem difficult to extrapolate to CSP applications. Osorio et al. [255] studied the behavior of a sCO₂ cycle driven by a solar tower during days with diverse irradiation profiles; two unusual buffer storage units are installed, respectively at the hot and cold sources of the cycle. Singh et al. [256] modeled the dynamic response of a sCO₂ cycle driven by a parabolic trough CSP plant without storage during typical summer and winter days. Luu et al. [251] studied several sCO₂ Brayton cycles driven by a solar island featuring an auxiliary boiler but no thermal storage; the main focus was to define optimal operation strategies in order to cope with variable solar irradiation. In [257], the same authors studied thoroughly the cold start-up of a similar power plant with a non-reheat recompression cycle. Regarding the heat input, a boiler-only strategy (no solar input) is proposed: since it allows the operator to fully control the heat input, it could apply to a CSP plant with direct storage. Six hours are required for a cold start-up, from zero to full load operation; no warm or hot start is modelled in the study.

With the exception of the latter (to a certain extent), these publications are focused on the response of sCO₂ cycles submitted to unwanted variations of the heat input. However, this is not the challenge to be met by future CSP plants whose power cycle is fully isolated from any solar events by their direct storage. These power plants will have to meet an increasingly variable power demand from the grid, most probably with

Table 11Efficiencies of some representative sCO₂ cycles plus an A-USC steam cycle.

Ref.	First Author	TIT °C	TIP MPa	PowerMW _e	Layout	Efficiency CIT = 45 °C	Efficiency CIT = 51 °C
[251]	Luu	600	25.0		RC	45.0	43.5
[252]	Alfani	620	25.0	100	RC	41.3	40.0
[236]	Neises	630	25.0	115	PC	47.4	46.0%
[235]	Neises	650	25.0	35	PC/RH	52.8	51.2
A-USC steam cycle[15]		650 670	33.0	300	N.A.	48.96	48.15
[251]	Luu	700	25.0		RC	49.1	47.5
[237]	Binotti	750	25.0	25	PC	51.7	48.7
[233]	Crespi	750	30.0		PC	47.8	46.2

one start-up/shut down cycle per day. Studying these transients, regardless of any solar consideration, is what is really needed. Such studies are currently underway, notably in the Horizon 2020 project sCO₂-Flex [258]; this project develops and validates the design of a 25 MW_e sCO₂ cycle that will increase its operational flexibility. The design is scalable for future fossil-fueled power plants. Cagnac et al. shortlisted three cycles to be further studied in [259]. The components of the power cycle, including their transient behavior, will be tested separately. Alfani et al. [252] describe an insightful study developed within the sCO₂ Flex project. The study aims at finding good trade-offs between thermal efficiency and flexibility of a 100 MW_e recompressed sCO₂ cycle integrated in a coal power plant, its CO₂ characteristics being 620 °C/25 MPa at turbine inlet and 33 °C at main compressor inlet. The study starts from the assumption that the heat exchangers prevail regarding flexibility, because sCO₂ turbo-machinery is very small whilst ~5 MW_{th} of recuperators are required per MW_e of power output. The impact of the heat exchange areas, volumes and masses of the various heat exchangers were analyzed. Various cycle configurations with different combinations of heat exchanger designs were envisioned. A Pareto front of the best efficiency vs. thermal inertia trade-offs provides seven relevant configurations for next generation sCO₂ coal power plants. A sensitivity to the maximum CO₂ pressure and turbo-machinery efficiency was also performed. It is eventually suggested that 1/ such sCO₂ power cycles should allow for a better efficiency/thermal inertia compromise than equivalent subcritical steam cycles (no supercritical steam cycle is mentioned); 2/ a more detailed study of the system and its controls is required to refine this comparison, according to relevant criteria that depend on operational strategies and market valuations. Other studies are currently being performed within sCO₂-Flex and will be published later.

To summarize, even though a growing number of theoretical studies are published, results that allow quantifying the flexibility of a sCO₂ power cycle – with practical data such as hot start-up times or load variation rates – are still lacking today. However, there seems to be a growing interest for this topic in conjunction with the increasing number of test facilities.

5.5.5. Materials

According to Ho et al. [260], the maximum temperature reached by the turbo-machinery (governed by the TIT) should not raise major issues, other than a more complex design of bearings and seals. This prediction is based on the fact that the blades of an un-cooled gas turbine can work – admittedly at much lower pressures – at temperatures up to 1150 °C; it still holds with a (probably more realistic) ~1000 °C threshold for un-cooled gas turbines. In view of this, the authors consider that the pressure and temperature of the primary heater (the hottest heat exchanger) are the parameters that limit the cycle's TIT, depending on the maximum allowable stress vs. temperature of its material. It should be noted that the authors reach this conclusion without taking explicitly corrosion into account.

Corrosion is a major issue and a key criterion for choosing the right materials: the frequent use of CO₂ as inert gas for certain industrial applications may be misleading in this regard. Corrosion with CO₂ at high temperature takes place through oxidation (in a similar way as with steam) and carburization; both phenomena expand with time and temperature following a parabolic law. Since the resistance to oxidation is highly dependent on Cr content, austenitic steels (preferably with a Cr content higher than 17% [234]) are much more resistant to oxidation than ferritic/martensitic steels. The difference is less obvious regarding carburization [261]. Nickel-based alloys are highly resistant to CO₂ corrosion: the generation of a Cr₂O₃ layer provides an efficient protection against further oxidation and carburization is limited by the low solubility of carbon, the low stability of chromium carbide, and the protection allowed by Cr-oxide against carbon penetration. Oxide dispersion strengthened (ODS) steels are promising: their Al₂O₃ inclusions provide far better protection than a Cr-oxide layer, especially regarding carbon penetration. They are being considered for future

nuclear applications but not for CSP, due to cost and manufacturing difficulties.

Even though White et al. mention a 650 °C threshold for replacing stainless steels with Nickel- or even Titanium-based alloys [241]. There seems to be a general consensus for limiting the temperature of 9–12% Cr ferritic-martensitic steels to 500 °C, that of austenitic steels to 600 °C, and to use Nickel-base alloys for temperatures from 600 to 800 °C [198, 234]. Results from long-term studies performed for steels at temperatures up to 600 °C are available; regarding Nickel-based alloys at temperatures > 600 °C, research is underway and more long-term studies are necessary.

5.6. Overall comparison of the proposed highly efficient power cycles

5.6.1. Efficiency

The efficiencies of the three technologies (supercritical steam cycles, combined cycles and sCO₂ cycles) being similar, so are the thermal duty of the respective heat sinks (air-cooled condenser or dry sCO₂ cooler). Therefore, the differences in parasitic consumption of their cooling fans (the main auxiliary consumers of the power cycle) are second-order, so that it is legitimate to compare gross efficiencies. Please note that the “half-net” efficiency considered above for steam cycles is the one relevant for this comparison, since the feed water pumps are part of the cycle, as are the compressors of Brayton cycles. A tentative comparison of the efficiencies of the technologies assessed in this study is shown in Table 12. The cold end temperature of the cycle (compressor inlet in Brayton cycles, condensing temperature in steam Rankine cycles) considered is 54.3 °C, quite typical (even slightly conservative) for CSP. It corresponds to an ambient temperature of about 40 °C. The efficiency given for the sCO₂ cycles is a 2%-wide range because it cannot be precisely predicted today for utility-scale units. In all likelihood, sCO₂ cycles will be more efficient than USC cycles and, at best, as efficient as A-USC cycles and externally heated combined cycle gas turbines. The comparison would be much more favorable to the sCO₂ cycle should the heat sink allow for a compressor inlet temperature of sCO₂ cycles close to 31.0 °C.

The combined cycle needs a higher TIT than the steam and CO₂ cycles to achieve interesting efficiencies. Since the corrosion issues are comparatively non-existent and the pressures much lower, this is not an issue for the gas turbine. However, this higher temperature translates into higher thermal losses, especially in the solar receiver whose radiant losses are proportional to T^4 . Consequently, when considering the overall efficiency of the plant, combined cycle will most certainly be at a disadvantage compared to the USC, A-USC and sCO₂ cycles.

In light of the above, the right choice today to enhance the efficiency of the current benchmark is the USC steam cycle. The sCO₂ cycle may be an option within a ~2030 time horizon; its merits – simplicity, higher flexibility (yet to be proven, but likely), potentially lower cost, and compactness (not really relevant in CSP, given the size of the solar field) – remain.

5.6.2. Technological readiness

USC steam power cycles of 250–300 MW_e (power outputs that can be envisioned for a big solar tower with a solar receiver of ~650 MW_{th} and

Table 12
Tentative comparison of the efficiencies of the three technologies.

	Sub-critical steam	USC steam	A-USC steam	Ext. Heated CCGT	sCO ₂
Pres./TIT/RHT (MPa/°C/°C)	12.0/553/553	26.0/600/600	33.0/650/670	TIT 780 °C	~25.0/~650
Efficiency, lowest T = 54.3 °C	42.5%	45.3%	47.7%	47.7%	46–48%

operated as a peaker) begin to be commercially available and are a first step before the A-USC steam cycle that is not fully technologically ready yet. The externally heated combined cycle raises probably fewer challenges than the A-USC steam cycle but fosters less interest in the literature, so that convincing a manufacturer to build the first-of-a-kind gas turbine must not be taken for granted. Regarding the supercritical CO₂ cycles, it is a long road to go before reaching commercial availability for power outputs ≥ 100 MW_e with a TIT high enough to allow for a decent efficiency compared to that of proven technologies.

5.6.3. Operational flexibility

The steam generator of the benchmark/subcritical steam cycle and the high-pressure stage of the bottoming cycle of the combined cycle should be once-through for higher flexibility. The steam generator of the supercritical steam cycles are *ipso facto* once-through. Therefore, the operational flexibilities should not be very different; probably slightly higher for the combined cycle (thanks to the gas turbine) and slightly lower for the supercritical steam cycles. The supercritical CO₂ cycle should be the most flexible of all, although this remains to be proven.

In the tentative techno-economic assessment presented in Section 11, specific cycles were selected for a detailed example. Other options (e.g., supercritical steam or CO₂) could however be assessed similarly.

6. Scale-up procedures in the particle-driven CSP systems

In process engineering scaling up is a critical issue that needs both experimental and numerical developments. Typical steps can be summarized as follows. First, small-scale prototype development of the technology components and identification of bottlenecks related to scaling-up and operational issues, first validation of the process simulation (TRL4). Second, qualification of the technology through testing at larger scale than previous step with improved hardware, refining of the process modeling, validation of LCA and economic assessments, identification of health and safety, environmental, regulation and resources constraints (TRL5). Third, integration of all the up-scaled components to construct an energy system that accounts and solves the issues previously found, design and modeling of full commercial-scale system including refining of economic and circularity (TRL6). Demonstration system, first of the kind (FOK) commercial system and full commercial application are the next three steps of the development procedure (TRL7, 8 and 9 respectively). For particle-driven CSP systems, the three most developed technologies (falling film, centrifugal particle receiver and fluidized particle-in-tube) have reached TRL5, in particular concerning the solar receiver that is the most critical component. In addition to the particle solar receiver, the particle handling system and the particle heat exchanger are the two other sub-systems for which scaling up issues must be examined carefully. They are discussed in Section 4 and 5. Consequently, this section addresses mainly the scaling-up of the solar receiver and the integration issues. Concerning the solar receiver, typical thermal powers are 10–100 kW for step 1 (TRL4), 100–1000 kW for step 2 (TRL5&6), 5–10 MW for the demo-unit and approximately 50 MW for the FOK unit.

6.1. Scaling-up the particle-driven solar receivers

Upscaling the three most mature technologies cited above gives rise to different issues that are linked to the specific characters of each design. Nevertheless, they share the same question: what is the maximum length/diameter of a single receiver? Considering that increasing the power needs increasing the characteristic length. As a reference, the tube length of commercial molten salt receivers is approximately 20 m. The identified issues for particle receivers are, for example, the control of the stability and opacity (decrease of the particle volume fraction) of the particle flow for the falling film, the particle layer thickness and cylinder diameter for the centrifugal receiver and the bubbling flow evolution to slugging when increasing the tube length

for the fluidized-particle in tubes. At the FOK level, design efficiency of the solar field is a common necessary data for the engineering and cost evaluation of the complete system. In the following, a medium size solar field is designed and a cavity receiver is assumed because of the high operation temperature. This assumption allows calculating the spillage losses that are included in the optical losses.

6.1.1. Solar field at the 50 MW_{th} scale

The optimization of the solar field layout associated with the cavity solar receiver is essential to ensure a high collection efficiency (optical efficiency \times thermal efficiency). In general, a tradeoff must be found because the receiver thermal efficiency increases with a decrease of the solar receiver aperture surface area (reduction of the radiation losses) but the optical efficiency decreases. This trend is due to solar reflected beam spillage at the receiver aperture that rises considerably with a decrease of the aperture size. For large-scale solar power plants (≥ 100 MW_e), a single tower would lead to a low collection efficiency and too many towers would lead to a complex handling and conveying of the particles. Consequently, a sensitivity analysis is necessary to determine the optimal power of the solar receiver.

Such a study involves the integration of many simulation tools. It starts typically with the optimization of the solar field layout using SolarPILOT software [262]. Then the position of the heliostats is introduced into the ray-tracing software that computes the flux density on the cavity receiver elements. Finally, a thermal model provides the power absorbed by the particles, among other data.

The following presents an example of the solar field design approach accounting for a given aperture size of the solar receiver. To simplify the illustration of the approach, the results do not focus on the annual performance but on the performance for nominal operating conditions, March 21 at noon.

In SolarPILOT, the tower height is set to 120 m regardless of the power considered. The solar field design power is increased from 37 to 98 MW_{th}. The field optimization is achieved using representative profiles for 4 days during the year and 7 or 8 h per day. Fig. 19a shows a typical solar field layout optimized in SolarPILOT for an incident power of 61 MW_{th}.

Given the shape of the receiver presented in Fig. 19b, the maximum field radius is constrained in order to locate heliostats on the Eastern and Western part of the field. Consequently, the side zones of the receiver can be more easily irradiated. Under these constraints, the solar field efficiency decreases from 69% to 67% for a receiver thermal power of 50 and 61 MW respectively and a particle outlet temperature of 750 °C. The corresponding aperture size for 50 MW solar receiver is 6.5 \times 6.5 m².

Accounting for the high operation temperature (at least 750 °C), cavity-type solar receiver was chosen for the three most advanced concept. The 50 MW_{th} power for a single unit solar receiver is the recommended size for the centrifugal and the fluidized particle-in-tube technologies. Numerous numerical simulations have been developed to overcome this limit for the falling particle receiver as discussed in the next paragraph.

6.1.2. Particle solar receiver

The thermal performance of a 50 MW_e falling particle receiver was simulated in [135]. The corresponding peak thermal power of the north-facing heliostat field is 135 MW_{th} (2529 heliostats) and the tower height 145 m. The receiver square aperture size is 8.6 \times 8.6 m² and the particle curtain length is 13 m (receiver height). For an average outlet temperature in the range 750–775 °C the receiver thermal efficiency is ranging from 83 to 86.8% for the various tested cases. Annualized value is 85.7%. Kim et al. [263] proposed a multi-stage falling particle receiver in order to maintain a high enough particle volume fraction along the curtain height (it decreases rapidly) and to increase particle residence time under concentrated solar irradiation. Thermal capacity up to 100 MW_{th} was examined. A 256 MW_{th} cavity-type solar receiver with a 10.63 \times 10.63 m² aperture and a nod angle of 50° was modeled in [134].

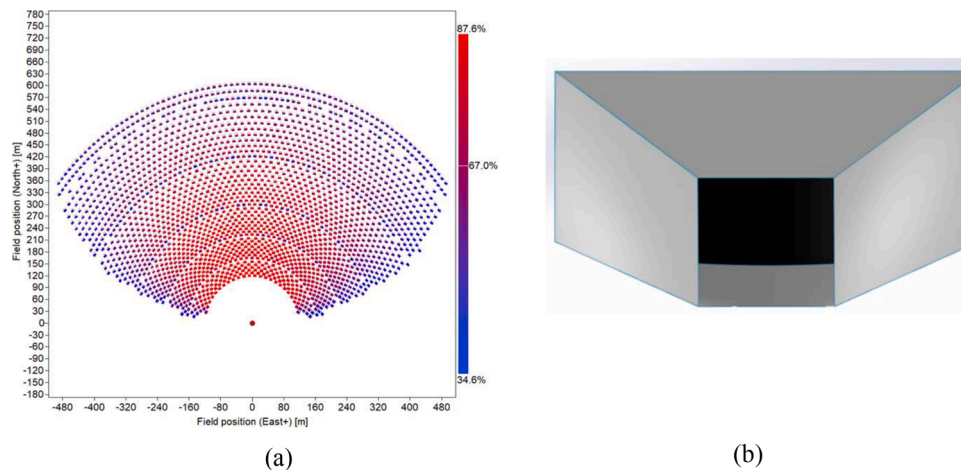


Fig. 19. (a) Solar field layout optimized in SolarPILOT for an incident power of 61 MW_{th}. Colors from red to blue illustrate the variation of optical efficiency of each heliostat. (b) Shape of the cavity solar receiver.

The maximum thermal efficiency reached 86.8%. Gobereit et al. [264] proposed a CFD simulation of a 400 MW_{th} facedown-falling particle receiver that exhibited an efficiency of 83% at design point. In addition, the critical issue of particle emission of the falling particle receiver was examined in [265] for ~ 350 and < 10 μm particles.

Concerning the centrifugal particle receiver, the association of 50 MW_{th} receiver and solar field modules (solar tower modules) is proposed in [266] to design a 125 MW_e commercial scale solar power plant with 12 h storage. Fourteen solar tower modules are necessary to achieve the power plant specifications.

The limit of 8 m in tube length allowing either bubbling or turbulent fluidization, which are favorable regimes for efficient wall-to-fluidized bed heat transfer, was established in [58]. On this basis, Gueguen et al. have modeled the thermal efficient of a 50 MW_{th} cavity fluidized particle-in-tube solar receiver [267] that corresponds to a realistic single receiver power designed accounting for this tube length constraint. They demonstrated that an efficiency of 85% can be reached.

As a conclusion of the previous analysis, one can conclude that two options are open for upscaling the particle CSP technology. First, a medium-scale solar power plant designed based on a ~ 50 MW_{th} solar tower module. Second, a large-scale solar power plant based on the multi-tower concept associating N solar tower modules depending on the desired power and capacity factor. The developers of the falling particle solar receiver are the only ones that assumes a single tower concept at commercial scale. The published works on medium and large-scale particle CSP are analyzed in the next paragraphs.

6.2. Medium-scale particle CSP plant

Solar power plants performances based on an approximately 50 MW_{th} solar tower module integrating a combined (CC) and a sCO₂ Brayton cycle were examined in [268] and [269] respectively, both involving the fluidized particle-in-tube concept. Behar et al. [268] showed that using an off-the-shelf gas turbine and 750 °C outlet particle temperature imposed a hybrid concept. Considering a 44 MW_{th} particle solar receiver, the corresponding power of the CSP plant at design point reached 18.37 MW_e with a 46% CC efficiency and 73.7% solar share. The solar-to-electricity efficiency was 25.8%. The integration of sCO₂ conversion cycle and a 10 MW_e power block results in an only-solar concept studied by [269] in the framework of the Next-CSP project. A solar-to-electricity efficiency of 30.8% and 26.3% at design point and on an annual basis respectively was calculated for 750 °C particle temperature. A sensitivity analysis of the model to particle temperature, heliostat beam quality and main compressor inlet temperature was also proposed.

Among the thermodynamic cycles discussed in Section 6, only steam Rankine cycles and supercritical CO₂ Brayton cycles are realistically applicable at a scale relevant for a ~ 50 MW_{th} receiver as the technical and economic performance of combined cycles is too degraded at that scale. CO₂ cycles show very promising performance at small scale (< 30 MW_e) but their techno-economic performance is to date much more uncertain than that of steam cycles. The detailed example of techno-economic estimation at medium scale given in Section 11 therefore involves a steam Rankine cycle.

6.3. Large-scale particle CSP plant

At utility scale (100 MW_e and more) the multi-tower concept with N solar tower modules (or solar islands) sharing the same particle storage and power block was examined by the authors. The following paragraph summarizes the design procedure of a peaker solar power plant. For more details on the technical features of such a plant, one should refer to Section 11 where a tentative cost estimation is proposed.

One of the original characteristics of such a plant is its low capacity factor, approximately 20–25% on a typical good day, estimated to 15–20% annually. This results in a solar loop and a thermal energy storage of relatively moderate size compared to the power block. At utility scale however, the solar loop is no longer small enough for only one solar field: the high temperatures necessary for the use of a high-efficiency cycle (> 800 °C for an externally heated combined cycle in the example of Section 11) make it impossible to achieve a decent receiver efficiency with an open receiver. A cavity receiver is therefore considered, limiting the individual capacity of a solar loop to 50–70 MW_{th} depending on the working temperature.

As thermodynamic cycles typically draw significant benefits from scale effects (both in terms of efficiency and specific Capex), the thermal energy storage and the power block are centralized. Considering the high Capex and thermal losses expected from long distance, high-temperature conveying (discussed in Section 4), the positioning of each individual field and of the power block + thermal energy storage island has to be optimized in order to minimize the total length of conveyors.

All the auxiliary power of the solar loop is considered to be provided by a small PV farm with a buffer battery, whose production is typically synchronized with the working time of the solar loop.

The externally heated combined cycle discussed in Section 6 needs two reheats in order to achieve an acceptable efficiency (48.6% at nominal conditions), i.e., a total of three heat inputs from fluidized particles-to-air heat exchangers. Air at moderate pressures (< 20 bar) is a poor heat transfer fluid due its low density; on the other hand, heat

transfer cannot be promoted by very high Reynolds numbers on the air side, as the combined cycle is very sensitive to pressure drops (see Fig. 19). High heat transfer surfaces have to be deployed, resulting in several heat exchangers in parallel. That results in an additional complexity of the particle handling systems around the power block, to be minimized by an adequate layout of the different heat exchangers around the air turbine. Simulation of the annual performance and the LCOE of a similar peaker solar power plant is proposed in [270]. A detailed example of tentative LCOE calculation is presented in Section 11 of the present article.

Concerning the falling film technology, another viewpoint is envisioned, the solar power plant is assumed to produce electricity as a base load utility with a capacity factor of 70% [271]. A single tower 100 MW_e solar plant located at Dagget (CA) is modeled with a 14 h storage. The concentration ratio is 1200 and the outlet particle temperature 800 °C. The hot particles power a sCO₂ cycle with a turbine inlet temperature (TIT) of 715 °C.

7. Baseload or peaker plants

7.1. Future CSP plants will be peakers that generate power during nighttime

Photovoltaic electricity is about three times cheaper than CSP, as shown in Table 13 below whose results are drawn from [272]. A site with an excellent irradiation (e.g., Daggett, California) for CSP, and one with a fair irradiation (Kansas City) for PV. The ratios shown in Table 13 would be higher with similar site conditions for both technologies.

Besides, it will be increasingly curtailed (i.e., worthless) during midday hours, an obvious consequence is that CSP must not generate power during daytime (except on sunny summer days when storage overflow would otherwise require heliostat defocusing). On the other hand, in areas with high DNI, CSP is one of the cheapest ways to generate power during nighttime and should remain so until 2040, as explained later in this section. More specifically, CSP plants must generally be designed as peakers that concentrate their daily power generation on a four to six hour time duration (during the evening plus, sometimes, early morning). This requirement will be increasingly critical as the growing share of variable renewables translates into an increasing variability of the net demand, as shown in [273] for California. To achieve renewable shares of 60% and beyond in the future, enhanced grids, proper demand side management and optimized flexibility of existing fossil-fueled power plants will not suffice: flexible renewables and/or massive electricity storage will be mandatory, as shown in [274] for Europe. In [214], a request for proposal issued in mid-2017 by the Arizona Public Service utility was studied and the “best fit” molten salt tower CSP plant was determined. The pricing of electricity is multiplied by a coefficient that depends on the hour of the day and the month: 0, 1, 3 and 9 during respectively 70.2%, 11.8%, 9.7%, and 8.3% of the time. The “best fit” plant has a very low capacity factor: 17.4%, which means that it is a peaker. For this plant, the weighted average of the pricing coefficient is 5.33 whereas it would be 1.84 at best for a base load, “Gemastar-like” CSP plant with a 63% capacity factor. In other words, the value of the electricity generated by this peaker CSP plant is 2.90 times that of the base load plant. Of course, the peaker plant is costlier: compared to a base load plant that generate the same yearly amount of energy, it has a somewhat bigger storage (no heat is spent during daytime) and a much bigger power cycle (in inverse proportion

of the capacity factors). Considering the cost breakdown of a typical molten salt tower described in [275] and reprocessing it for both the base and peaker plants, one can determine that the LCOE of the peaker plant is 1.46 times that of the base load plant. To summarize, the value/cost ratio of the power generated by the peaker plant is about twice that of the base load plant (2.90/1.46): the choice of the peaker is obvious here. The peaker still wins with a much milder (and unrealistic for future highly renewable networks) price differentiation depending on time of day; for example with price coefficients (2.0|1.5|1.0|0.5) instead of (9.0|3.0|1.0|0), the value of the peaker is 1.75 times that of the base load. To summarize, even though base-load CSP plant are regularly mentioned as viable options [276], it will usually be optimal for the electrical systems to use CSP plants as peakers (or perhaps mid-peakers in some contexts) that typically generate power during four to six nighttime hours per day. As shown below,

- Utility-scale batteries charged mainly by photovoltaic power is the only alternative to CSP,
- Today, its LCOE is similar to that of CSP for four hour per day of peak shifted generation, but is higher for mid-merit (i.e., more hours per day) generation,
- CSP will remain competitive in 2040 provided it benefits from substantial improvements.
- It is more expensive today and will still probably remain so in 2040.

7.2. Potential alternatives to CSP as flexible renewable power generation

The flexible renewable technologies for power generation are: hydro, CSP, biomass and geothermal. In order to limit the cost and energy losses of the grid, flexible power generation must be properly dispatched on the territory, including in desert or semi-desert areas that are well-suited to CSP. The global resource for geothermal energy is limited to very specific areas where CSP cannot be envisioned. Hydro and biomass power generation are ill-suited to CSP-friendly, dry areas (due to its low energy density, long-distance transportation of biomass is economically and environmentally challenging). Besides, biomass is renewable but its carbon neutrality is questionable [277] and it generally does not fare better than fossil fuels regarding emission of pollutants such as particles and NO_x. To summarize, in arid areas where flexible power generation is required, no other renewable and clean power generation technology can replace CSP. That being said, utility-scale storage units [278] charged with renewable (including curtailed) electricity can be another alternative to CSP. Hydrogen may play a significant role in the future for long-term storage aimed at correcting inter-season imbalances, but is irrelevant here. Flywheels and supercapacitors cover very short term storage needs that do not belong to the scope of this study either. Pumped hydro storage is discarded for the same reason as hydro power generation. Compressed Air Energy Storage is an attractive concept but it needs underground cavities and its deployment remains confidential. Pumped Heat Energy Storage (i.e., Power-to-heat-to-power storage) may be relevant in some contexts (notably the conversion of existing coal plant into storage units that requires limited capital expenditures) but its round-trip efficiency is low: about 40%. Replacing the electrical heating with a heat pump would increase the efficiency, but not drastically. Cryogenic storage (e.g., using liquid air) is another option [279]; combining heat and cryogenic storages potentially allows for good round-trip efficiency [280] but leads to high complexity and low technological readiness. Thermo-chemical storage could replace thermal

Table 13
Comparison of LCOE of utility-scale PV and CSP without storage.

LCOEs US\$/MWh	Conservative scenario			Moderate scenario			Advanced scenario		
	Utility PV	CSP	Ratio	Utility PV	CSP	Ratio	Utility PV	CSP	Ratio
2020	32.7	82.1	3.20	31.4	82.1	2.61	30.7	82.1	2.67
2030	28.8	78.2	2.72	18.3	58.6	3.20	13.9	42.1	3.03

storage for both CSP and Pumped Heat Energy Storage but its technological readiness is low.

To summarize, in any area where CSP can be envisioned, electrochemical storage (i.e., batteries) is the only possible alternative technology.

7.3. Current and future cost of renewable power shifted with batteries

In such areas, the typical battery unit will be mainly or fully charged with a dedicated PV farm, curtailed (i.e., worthless) electricity being an optional and marginal contribution. The Li-ion technology is dominant for utility-scale batteries and allows for quick charge and discharge, which can be useful for some networks. Other technologies (e.g., Na-S batteries, flow batteries) may prove cheaper in the future for utility-scale storage, but they have other drawbacks [281] and lack industrial maturity; therefore, they are not considered here. The Capex of a complete four-hour Li-ion battery system from 2018 to 2050, as determined in [282], is shown in Fig. 20. The Capex starts in 2018 at US\$ 380/kWh, which corresponds to [283] and is consistent with the 2019 Capex determined in [275]: US\$ 347/kWh for a 200 MWh / 50 MWe storage system. Four hours of nighttime power generation per day meets the typical need of future networks for peak generation, a different discharge duration would change the relative sizing of the inverters with some impact on the LCOE, but to an extent that would not affect the following analysis.

Neglecting the Opex, the LCOS of the battery system corresponds to the amortization of its Capex. A 15 year lifespan, a discount rate of 5% in constant currency, and 300 cycles with a 70% capacity per year are considered. The resulting LCOS for 2020, 2030 and 2040 are summarized in Table 14, with the three scenarios. According to [13], the world weighted average of the 2019 LCOE of PV generation is US\$ 68/MWh. This value was reprocessed as follows: 1/ Reducing the discount rate from 7.5% to 5% (with a 25 year lifespan) reduces the LCOE by 20%; 2/ The required PV capacity is divided by the round-trip efficiency of the batteries (85%). The resulting 2019 LCOE of shifted PV generation is US\$ 64/MWh. Then, a reasonable extrapolation using 2015 to 2019 values from [13] leads to the following predictive LCOEs of PV in US\$/kWh: 59.9 in 2020, 41.7 in 2025, 32.7 in 2030, and 23.5 in 2040. By adding these values to the aforementioned LCOS, one determines the cost of PV electricity fully stored, then released to the network during four nighttime hours. These values are summarized in the columns “LCOE” in Table 14. Please note that the LCOEs mentioned in Table 14 must not be confused with the “LCOE of PV + X hours of battery storage” that is often referred to, where only a fraction of the electricity collected by the PV farm is shifted in order to extend its generation beyond sunset. Since it is well understood that daily power generation must be done by PV only, the comparison must be made between shifted (i.e., nighttime) CSP generation and shifted power generation with PV + batteries.

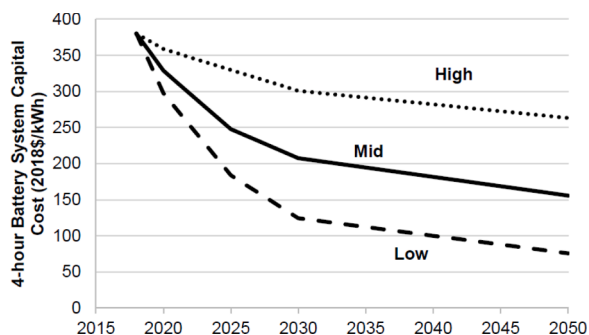


Fig. 20. Cost projections for a 4-hour Li-ion battery system. Source: NREL.

7.4. Economic comparison of electrochemical storage and CSP thermal storage

The medium scenario/2020 LCOE shown in Table 14 is to be compared with that of a peaker molten salt tower built in 2020 that dispatches its power generation within four nighttime hours per day. The total project cost of such a plant (built in the US in order to avoid any geographical bias) can be assessed by reprocessing the results given in [214]: about US\$ 675M for a net power output of 230 MWe with a capacity factor of 13.2%. With a 5% real discount rate, a 25 year lifetime and US\$ 25/MWh for O&M (US\$ 21 + US\$ 4 to account for the bigger power cycle, see Section 11), one obtains a LCOE of US\$ 201/MWh for a plant built in 2020.

Note that the LCOE estimate of Section 11 is made under different assumptions with the objective of comparing the LCOE of a tower using fluidized particle beds with that of a molten salt tower, both being built in 2030. It is not fully relevant here.

All the above mentioned LCOEs correspond to fully shifted power that is generated during four nighttime hours. They would be lower for both technology (CSP and PV + batteries) if the power were generated during more hours (and vice-versa). Here is why:

- The amount of energy generated by a CSP plant sizes the same solar island and the thermal storage system (able to store one day of solar collection); However, for a given amount of energy generated, the sizing of the power cycle (along with the transformer switchgear, the circuit breaker and the transmission line) is inversely proportional to the generation time.
- The same reasoning applies to a PV farm equipped with batteries, replacing the CSP solar island with the PV farm, the thermal storage with the batteries, and the power cycle with the inverters plus transformer switchgear, circuit breaker and transmission line.

Comparing the costs given by [275] for two battery storage systems: 50 MW/200 MWh, total capital cost US\$ 69,456k, and 200 MW/ 100 MWh, total capital cost US\$ 45,260k, one can determine the cost structure of their total capital cost: US\$ 272/kWh + US\$ 301/kWh. The US\$ 301/kWh correspond mainly to the cost of the inverters, plus that of transformer switchgear, circuit breaker and transmission line. It is much lower than that of the sole power cycle, about US\$1100–1200 [284]. Therefore, the LCOE of a CSP plant will decrease much faster than that of a PV + batteries farm when extending the generation time from four hours (considered in this study) to more, e.g., for a plant generating during the whole night.

7.5. Final considerations

The following conclusions can be drawn from this study:

For a peaker plant that generates shifted power during (typically) four nighttime hours

The LCOE of a PV + batteries plant that shift all its generation during four nighttime hours is US\$ 208/MWh, vs. US\$ 201/MWh for a molten salt tower – the current benchmark of CSP plants – with the same dispatch strategy. The difference (3.5%) is well within the uncertainties of the estimates. This comparison applies in the US whose local costs

Table 14

Four hours Li-ion battery system: estimated LCOS of battery system and LCOE of PV generation delivered during four nighttime hours. All values are in 2020 US \$/MWh.

Scenario for cost decrease	2020		2030		2040	
	LCOS	LCOE	LCOS	LCOE	LCOS	LCOE
High	161	221	135	165	126	150
Medium	148	208	92.7	125	81.5	105
Low	133	193	55.5	88.2	44.8	68.3

(labor, regulations) are among the highest in a developing country, the CSP solution would benefit significantly more from cheaper local labor costs: local construction and O&M costs of a CSP plant proportionally are much higher than those of a PV + battery power plant. Therefore, the molten salt tower has probably an edge in developing countries.

The future will be challenging for CSP: according to Table 14, its LCOE must decrease at least as follows in 2030 to remain competitive with that of PV farms equipped with batteries:

- -18% if the cost of PV + batteries farms decrease according to the “high” scenario;
- -38% with the “medium” scenario;
- -56% with the “low” scenario.

Therefore, the future of CSP depends in great part on the cost decrease of PV + batteries farms:

- CSP will most certainly remain competitive if the “high” scenario prevails,
- With the “medium” scenario which is also the most likely, CSP will remain competitive provided significant improvements are performed: incremental ones and, if possible, technological breakthroughs. In the light of the recent past, it seems perfectly feasible.
- If the “low” scenario prevails, the competitiveness of CSP will be an uphill battle: significant technological breakthroughs (such as using particle circulation loops for CSP) are the only option.

Incremental improvements will probably not suffice to achieve that goal; technological breakthroughs, such as using particle circulation loops for CSP, are needed.

For a mid-merit plant that generates shifted power during, e.g., six or more nighttime hours

As explained above, longer generation times favor CSP over PV + batteries quite strongly. Precisely quantifying this statement is out of the scope of this study. However, starting from the conclusions above for four hours of generation, it is clear that CSP is and will remain most certainly competitive than PV + batteries for, e.g., generating eight nighttime hours per day. One potential hurdle remains: with the incremental phasing out of fossil-fueled power plants, peaking renewables will be needed before mid-merit ones.

8. Hybrid systems: the use of alternative fuel for CSP plants

Actual CSP plants have moderate electricity costs, but in most cases quite lower capacity factors and transient problems due to high inertia [285]. Moreover, CSP plants require backup system for non-sun periods. Biomass or other carbonaceous feedstock and their derived energy carriers (biogas, syngas, among others) can be a valid source in the BS system, despite the necessity to build a large biomass collection structure for scale of merit, the volatility of the biomass price and the lower feed-in tariffs [285].

Recently, hybrid CSP technology with biomass has however been rapidly developed. The hybridization [286] of these technologies would increase the power plant capacity factors (when compared to a solar only CSP) and reduces back up fossil fuel consumption still generating a dispatchable electricity flow with positive economic indicators [287]. The first concentrating solar power-biomass hybrid power plant commenced operation in Spain and the combination of both energy sources is promising to lower plant investment [288].

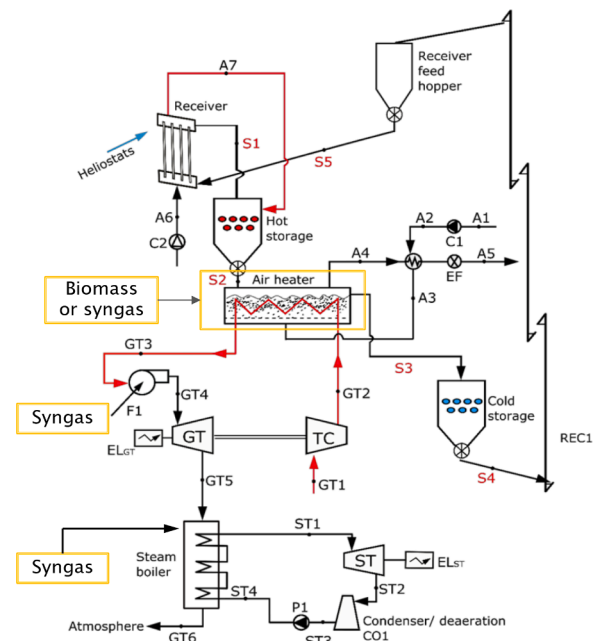
Considered hybrid co-production plants are illustrated in Figs. 21 and 22 [287], where the possible application of biomass, its derived syngas or biogas as back-up fuel is indicated and applied in various sub-sections of the overall plant layout.

Biomass is widely available, with a lower heating value ranged from 15 to 23 MJ/kg. When biomass has a high water content, or comes from animal or urban residues, the most applied biomass conversion

technologies are based on bio-methanation. These technologies are largely applied in wastewater treatment plants (WWTPs) and landfills and generates biogas or landfill gas, which is available as a fuel. Biomass, its pyrolysis/gasification or its bio-methanation derivatives can be readily applied in a hybrid CSP.

Petersheim et al. [288] conducted a case study approach of 17 possible CSP-biomass hybrid configurations including only mature technologies with references >5 MW_e, with the aim of identifying the best configurations regarding technical, economic, and environmental performance in Mildura, Australia. The CSP technologies selected are Parabolic trough, Fresnel and Solar tower with thermal oil, steam or molten salt as working fluid, while the biomass systems include grate, fluidized bed, and gasification with produced gas used in a boiler. The plant net capacity ranged from 17.3 to 19.5 MW_e in all configurations. As results, while the efficiency differences for the 17 scenarios reach 13%, the investment variations are with 31 % significantly larger. Solar tower-biomass gasification hybrids reach the highest net cycle efficiency, 33.2%, but Fresnel-biomass hybrids have the lowest specific investment of AU\$ 4.5 /MW_e. Based on the annual electricity generation CSP-biomass hybrids have an up to 69% lower investment compared to standalone concentrating solar power systems. The integration of thermal storage can increase the annual generation of CSP-biomass hybrid plants up to 17% (7 h TS) but currently requires a capacity value payment to be competitive with a no storage plant. However, even with extensive thermal storage most of the electricity, 70%, still derives from the biomass resource.

Coelho et al. [289] have analyzed numerous possibilities of hybridizing between a forest waste biomass direct burning boiler and CSP plants. They have used Epsilon Professional software to design and optimize the power conversion system, while the solar subsystems, i.e., heliostat field and volumetric receiver have been designed and optimized in HFLCAL software. The authors have analyzed 8 cases in terms of hybrid solution (only solar, biomass or hybrid), scale (4 or 10 MW_e) and storage in the field of the Portuguese Algarve region. They have found that the best technical/economical solution in 4 MW_e power plant scale is the hybrid CSP/biomass plant with storage, which results in a LCOE of 0.144 to 0.149 €/kWh, with higher efficiency and capacity factor than a conventional CSP. Larger hybrid plants will exhibit a better performance: a 10 MW_e power plant can have a LCOE of 0.108 €/kWh



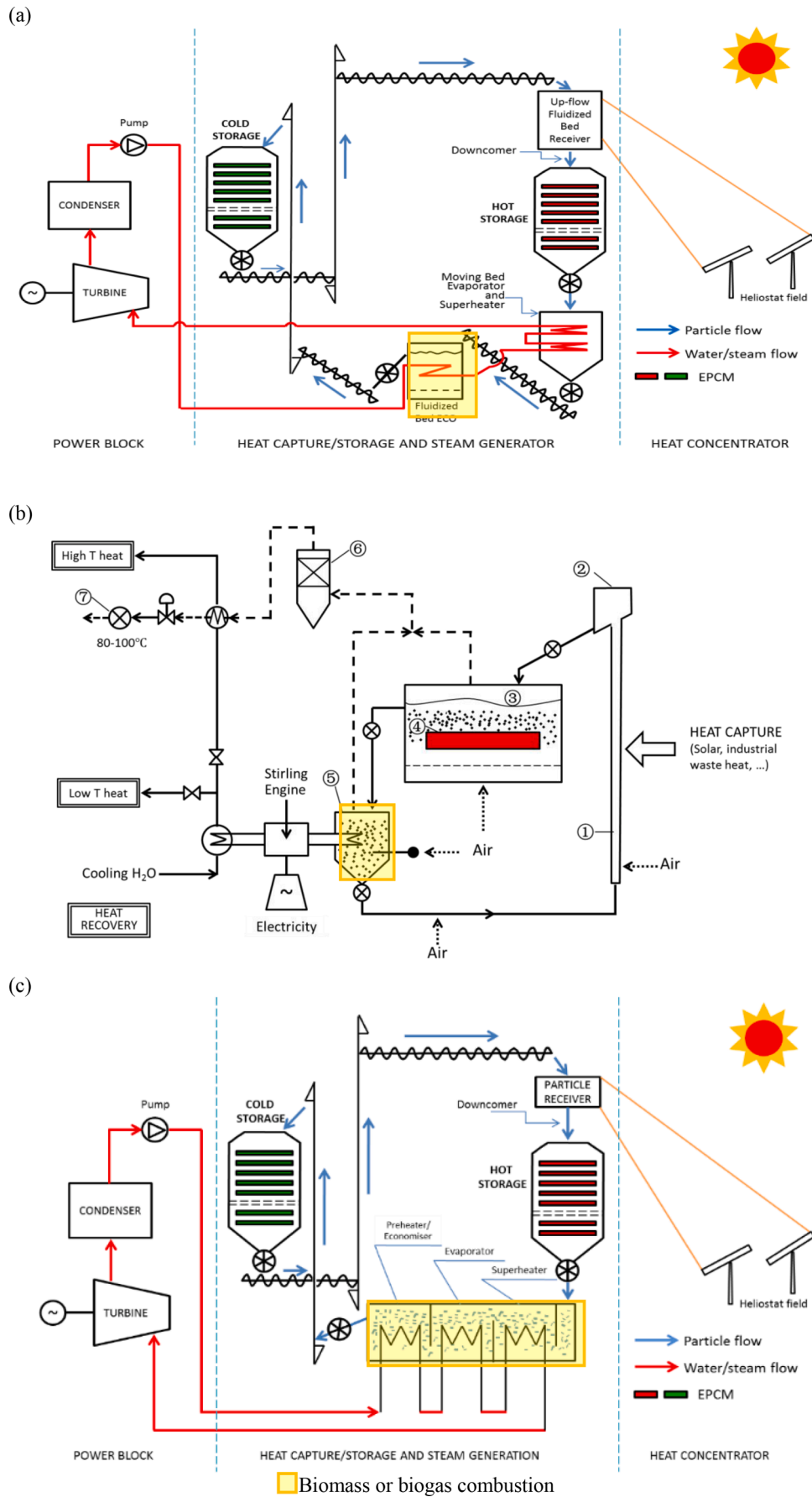


Fig. 22. Different options of a hybrid biomass - CSP power plant.

with twice the annual efficiency and lower costs than the solar only tower system of 4 MW_e. The proposed concept could reduce biomass consumption by 17% compared with biomass only power plant.

Coelho et al. [290] analyzed several base case power plants and hybrid biomass/CSP options: wood gasification, refuse-derived fuel pellets, biogas from a wastewater anaerobic digester, biogas from a landfill and natural gas. As results, the LCOE for the CSP base case is 0.23 €/kWh and the best base case LCOE is the WWTP anaerobic digester with 0.08 €/kWh. The hybrid power plant investment with best payback period is the hybridization with an anaerobic digester, using sludge from a WWTP. This power plant returns the investment in 13 years (sludge collection and transport assumed without cost), presenting also the best net present value (15 million euro). However, for the 4 MW_e scale, WWTP or landfill biogas would only be possible close to large cities (few limited cases) with centralized plants capable of generating enough sludge or municipal solid waste (MSW).

A typical example of a large-scale hybrid CSP plant, is Termosolar Borges, a hybrid biomass-parabolic trough solar thermal plant which provides electricity to the Spanish grid. The plant is the most northern CSP plant built in Spain.

The plant power output is 22.5 MW_e. The facility combines solar power with biomass-fired power generation in a system that allows for continuous electrical production of renewable energy 24/7, even when the sun does not shine. The plant peak capacity of 22.5 MW_e is obtained when there is sufficient solar power. At night, when only the biomass power is available, the plant power capacity is 12 MW_e. The facility is located on a 70 hectare site. The schematic of the power plant is illustrated in Fig. 23.

The solar field consists of trough-shaped mirror reflectors to concentrate solar radiation on to receiver tubes containing thermal transfer fluid which is heated to produce steam. The solar field comprises 2688 collectors, 5.5 m in diameter and 12 m long each, and has been realized by Siemens [291], including the mirror and solar receiver. The heat is transferred with a thermal oil loop.

The thermal block comprises two 22 MW_{th} dual biomass and natural gas boiler (BM-NG), one 6 MW_{th} natural gas conventional auxiliary boiler (auxNG) for assistance, and a steam generator (SG). The biomass is inserted in series on the solar field thermal oil loop. Gas firing is intended for power shaping and back-up.

The electricity generation is composed of a 22.5 MW_e steam turbine generator train and a power transformer. The turbo generator train comprises one high-pressure turbine followed by a low-pressure turbine. The electrical block converts the thermal energy in mechanical energy in the steam turbines followed by the generator which changes that into electricity. Turbine full load efficiency is 37%. The plant is to produce electricity on a continuous basis, round-the-clock. Gas firing is available for back-up. The auxiliary systems include shredding and biomass storage and control systems. Carbon offset is 24,500 t/year.

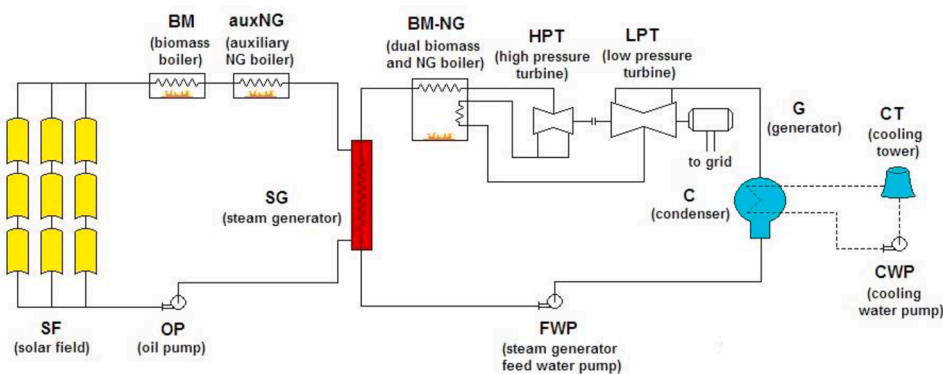


Fig. 23. the Spanish example plant near Lleida Thermo Borges.

Although the previous examples illustrate the potential of hybridizing CSP and alternative fuels, it is obvious that the solution is viable only in geographic regions with high solar irradiance when the CSP can provide a considerable share of the total power, and provided alternative fuels are available. If these conceptions are not met, a hybrid concept should not be envisaged.

9. Additional issues to be further assessed

9.1. Enhancing the particle-to-tube heat transfer coefficient in the particle-to-working fluid heat exchanger

The ideal heat exchanger will be executed as a baffled cross-flow fluidized bed (Fig. 24), using an in-bed externally finned-tube bundle.

The heat transfer coefficient from the fluidized bed to the heat exchanging tube, of different geometries, was measured by Zhang et al. [194]. The heat transfer coefficient from bed-to-wall was measured for the 3 tube geometries, and results are shown in Fig. 25. The fluid velocity inside the tubes was kept constant for all geometries.

The heat transfer from the tube wall to the turbulent fluid flow was separately determined, and was in excellent agreement with predictions by the Gnielinski equation. Finned tubes considerably increase the heat transfer coefficient through the larger surface area exposed to the bed. The twin-bore pipe results confirm the influence of the hydrodynamics and the absence of a stagnant particle nose and gas film enhanced the heat transfer in comparison with the round tubes. Since the heat exchanger will be of externally finned tube design with a high bed-to-wall heat transfer coefficient ($>> 2 \text{ kW/m}^2\text{K}$) [292], the overall heat transfer is determined by the wall-to-in-tube working fluid flow. At air velocities of 35 to 40 m/s at the exit T of $\sim 650\text{--}750 \text{ }^\circ\text{C}$, Gnielinski predicts air-side transfer coefficients of $\sim 325 \text{ W/m}^2\text{K}$.

Clearly, finned tubes enhance the heat transfer coefficient, and the reasons are reflected by the distinct gas/solid hydrodynamics around the tubes of different geometry [292].

9.2. Recommended research prior to multi-MW up-scaling

9.2.1. The maximum achievable solid flux

Common fluidized bed operations can be hampered in a specific (U , G) range where choking occurs, being understood as the phenomenon where a small change in gas or solids flow rate prompts a significant change in the pressure drop and/or solids holdup: the stable upflow regime can no longer be maintained when G -values exceed a certain limit for a low to moderate gas velocity. This choking can occur in dense upflow of particles when the superficial gas velocity and the driving pressure are no longer capable of entraining the particles. In the upflow bubbling fluidized bed concept, only G -values up to $110 \text{ kg/m}^2\text{s}$ were tested during hot experiments, where the stability of the operation was

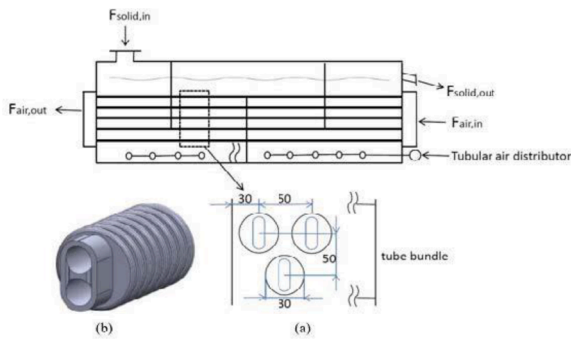


Fig. 24. Air heat exchanger design (a), with illustration of the twin-bore finned air pipe (b).

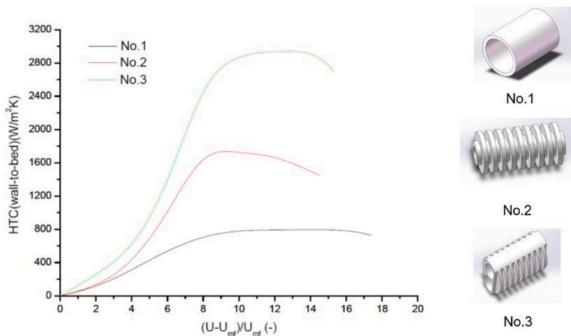


Fig. 25. Fluidized bed-to-wall heat transfer coefficient for different tube geometries.

confirmed. This is expected since the pressure balance indicates that the loop will operate in a stable manner provided the external pressure in the dispenser compensates the upflow bubbling fluidized bed pressure drop. At high G -values, acceleration and friction losses, both proportional to G^n ($n = 1-2$) will increase and will finally hamper the system stability. To assess the impact of (U, G) combinations, a non-choking criterion is established when considering that the particle slip velocity must remain positive. With equal to 0.65–0.75, as measured in the single tube experiments, ρ_p is between 910 and 700 kg/m³. For a specific gas velocity in the tube, the choking limit is illustrated in Fig. 26.

To operate the upflow bubbling fluidized bed at G -values in excess of 150 kg/m²s, superficial air velocities should exceed 0.17 m/s, as commonly used in the single and multi-tube set-ups.

9.2.2. Attrition of particles

Since a fluidized bed is the key in operating the solar receiver at a high wall-to-bed heat transfer coefficient, attrition of particles was examined experimentally in order to select the type of Geldart A-powders less prone to attrition. This extensive research was fully reported by Zhang et al. [293] and only essential features are summarized below. Although fast particle motion associates a high degree of mixing, it however causes inter-particle collision and bed-to-wall impacts, both leading to particle attrition. Attrition generates fines that can be lost in the dust collection system, whereas the particle size distribution of the bed will alter during the operation.

Zhang et al. clarified the influence of particle size and nature, bed height, fluidization velocity, action of jets and orifice diameter [293]. An equation was developed and enables to predict attrition rates for different particles at different operating contribution. The total attrition rate combines the bubble-induced and jet-induced effects. It was moreover shown that particles with a high Abrasion Index (AI), as defined by CEMA [294], are less prone to attrition. The higher AI is however an indication of the expected wear of the equipment [295].

Unlike SiC, cristobalite and olivine have a moderate AI and both attrition and erosion will be limited at the superficial gas velocities applied.

9.2.3. Finned receiver tubes

To overcome the high cost of SiC, 58 μm cristobalite of density 2340 kg/m³ was additionally and subsequently tested in a vertical high temperature electrical furnace using tubes of 46 and 50.09 mm O.D., each 0.5 m long. Operating parameters (temperatures of wall, inlet/outlet particles, arid solid flux) were continuously monitored. The absorbed heat was calculated from the heat balance of the particle suspension flow. The tube geometries, including fins in the 50.09 mm O.D., were known, thus enabling the calculation of the heat transfer coefficient. Since using only 4 temperature measurements of the outside wall along the height of the tube, and temperature measurements of the inlet and outlet solids flow, results are less accurate than when using multiple thermocouples as in the PROMES-CNRS on-sun set-ups, but allow a fair determination of an average overall heat transfer coefficient. Bare tubes tested were respectively 46 mm O.D. (wall thickness 2 mm) and 50.09 mm O.D. The 50.09 mm O.D. tube was also manufactured with internal fins, as illustrated in Fig. 27 for wall temperatures up to 685 °C. For comparison and to gather data at higher flux densities at the wall on-sun, single tube experiments (bare and finned tubes) were conducted by CNRS using Group A cristobalite and olivine.

Results were previously detailed in Zhang et al. [153], but repeated in Fig. 28. At higher wall temperatures, radiation heat transfer should be added and will increase the experimental values by about 50 (low G) to 150 W/m²K (high G), to achieve a maximum of ~ 1050 W/m²K for the bare tubes, and ~ 2200 W/m²K for the finned tube. Heat transfer coefficients for the bare tubes are slightly lower than those obtained by CNRS in 29 and 26 mm I.D. tubes [80,89,148,150]. The decrease of the heat transfer coefficient is however largely compensated by the increase in heat exchanger surface area per meter of tube length, being +27.7% for the 46 mm and +38.9% for the 50 mm tube. The exposed surface area of the finned tube was 2.84 times the surface area of the bare tube. Experiments moreover give evidence of the fact that solid circulation fluxes up to ~ 100 kg/m²s are achievable and provide stable operating conditions of the UBFB.

9.2.4. Particle conveying systems

The conveying of hot and cold particles at high capacity (>100 t/h) and for long vertical or horizontal distances needs further investigations. The solar project application poses several challenges. Points to be studied in detail as part of the equipment selection process include the following.

As the equipment heats up, the metal will expand. Hence, chains and belts that were correctly tensioned when cold will need to self-adjust

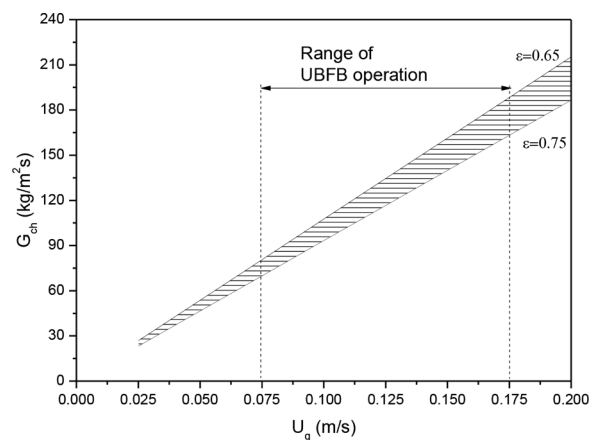


Fig. 26. Predicted choking limit at different superficial gas velocities and bed voidages between 0.65 and 0.75.

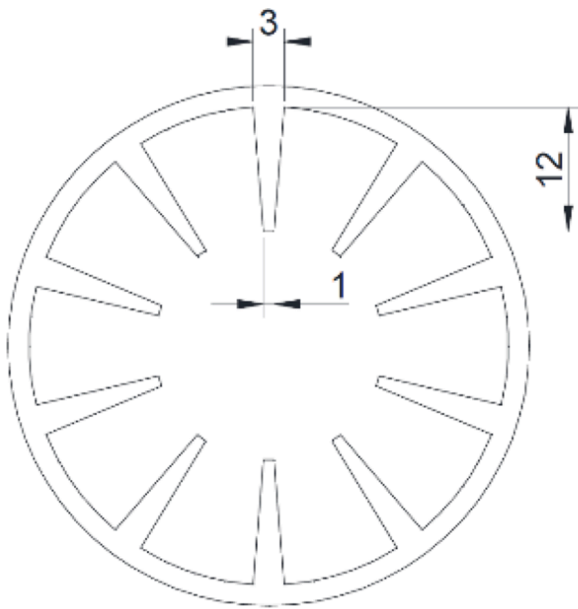


Fig. 27. Top view of the 50.09 mm O.D. finned tube.

when operating at temperature. The measures adopted at lower temperatures may not be applicable for the enclosed high-temperature designs under consideration.

To achieve the required high reliability, in addition to selecting equipment with such a potential, some preventative maintenance and inspection schedule will be required. Ways of achieving this need to be clearly established.

The conveyor carries certain standard monitoring instrumentation to ensure reliable operation and help reduce component wear and deterioration. All such instrumentation should function reliably at elevated operating temperatures.

The solids feed rate to the various equipment items, especially the solar receiver and the fluidized-bed heat exchanger, need to be accurately measured. How this is to be achieved needs to be established.

10. Tentative economics and LCOE for potential medium- and large-scale applications

The objective of this section is to assess the Levelized Cost of Electricity (LCOE) generated by (i) a ~ 25 MW_e medium-scale plant using a high-temperature subcritical steam cycle (ii) a 150 MW_e utility-scale plant using an externally heated combined cycle, to be built around

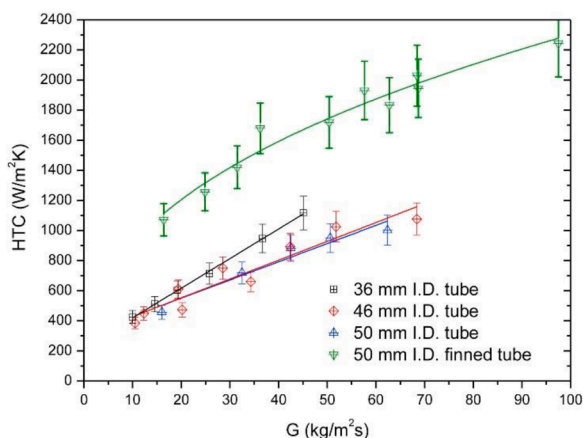


Fig. 28. Experimental heat transfer coefficient versus solids circulation flux G for different tube geometries [153].

2030 and using the same individual field layout. Their design is based on the UBFB solar receiver. The following calculations correspond to a plant located in Ouarzazate, Morocco: yearly DNI 2635 kW/m²year, latitude 31.06°, 1150 m above sea level. The general design is first outlined for each scale; then, Capital and Operation Expenditures (CAPEX and OPEX) are assessed for both plants in parallel; eventually, each Levelized Cost of Electricity (LCOE) is calculated according to given financial hypotheses. The CAPEX, OPEX and LCOE of the plants studied are compared to the benchmark CSP plant: a 150 MW_e molten salt tower using the current state-of-the-art technology built in the same site, also in 2030.

Let us notice that in the case of the two particle-based plants assessed in the present section, specific solutions were selected for a detailed example. Other options (e.g., using different cycles) could however be assessed similarly.

As already explained in Section 8, the best use of CSP consists in concentrating its generation during peak hours: evening and possibly early morning. Both plants are designed as peakers that generate five hours of full-load equivalent power during the evening: linear ramp-up from zero (a little before sunset) to full load in 40 min, then 4 h and 20 min at nominal load, then linear load decrease in 40 min until shutdown. The ramp-up rate is a reasonable hypothesis provided the plant is properly designed to that end [214].

The design of a utility-scale plant (150 MW) is described first. As the thermal input to a particle receiver is limited, that design involves several towers; therefore the assessment of a smaller, single-tower plant is also presented.

10.1. Design of the large-scale particle-based plant (150 MW_e)

The solar island includes the solar receiver(s), the tower(s) and the heliostat field. Factoring in foreseeable improvements to be performed by 2030, an average net solar flux impacting the particle solar receiver tube panel of about 550 kW/m² was considered; it is similar to that of current molten salt receivers. Given this moderate flux and the tubes' external wall temperature (~ 950 to ~ 1100 °C versus ~ 525 to ~ 650 °C in a molten salt receiver), a cavity receiver is mandatory to mitigate heat losses (most of them radiant and proportional to T^4). A maximum irradiated height of the receiver tubes of 8 m was considered to ensure stable hydrodynamic behavior of the fluidized bed within the tubes (no slugging). A width/height ratio of 1.63 allows a well-controlled flux map on the panel whilst avoiding excessive spillage. Given these three figures (8 m, 1.63, and ~ 550 kW/m²), the maximum thermal power of the receiver is approx. 57 MW_{th}.

Considering the aforementioned dispatch requirement and the cycle efficiency (48.6% in nominal conditions, less during transients) as well as 5% thermal losses overall from the receiver output to the power cycle (those losses are discussed further below), at least 1.68 GWh of heat must be collected daily by the solar island in order to meet the dispatch requirement. In Ouarzazate, it is achieved during 60% of the days of a typical year by six receivers of 56.2 MW_{th} each. In practice, since the heat from good days can be stored and used several days later, the dispatch requirements will be fully met during at least 280 days per year. Except for a very small overlap between generation ramp-up and sunset, no heat is spent during daytime; therefore, the storage is sized for a full day of heat collection. As a compromise between oversizing the storage and having to defocus heliostats during too many good days, the storage is sized for the 90th best day of the year, i.e., a thermal capacity of 2.0 GWh. Given the temperature difference (200 K) and the specific heat of olivine (1.22 kJ/kgK), 30,000 t (15,000 m³) of olivine are needed. Four hoppers (two hot, two cold) are used: their outer diameter is 31 m (accounting for wall and thermal insulation thickness: 0.50 m max.) and their storage height (including the V-shaped bottom) is 16 m.

In order to maximize the optical efficiency, each tower has only one receiver and a north field. Its optical height (i.e., from heliostat mirror level to panel mid-height) is 126 m. Each individual solar field is shown

in Fig. 11a; each of the 1879 dots represents a high performance Stello® heliostats developed by sbp [296]. The cost and thermal losses of the horizontal conveying network that links the storage system to the six towers are proportional to its total length that must therefore be minimized. To this end, various arrangements were considered and the total lengths of the six corresponding conveying networks were compared. The lengths with double and triple particle mass flow were multiplied respectively by 1.8 and 2.8. With a “wide” solar field such as this one (see Fig. 29a below: length/width = 640 m / 890 m = 0.73), the layout shown in Fig. 29b below allows for the lowest total length.

Besides, once this layout is chosen, the length/width ratio of each individual solar field minimizes the total conveying length. Therefore, the arrangement of solar island can be considered optimal. The total length of the horizontal conveying network is 4.0 km.

The critical issues affecting hot particle conveying sections are described in Section 4, and the required developments regarding the particle circulation loops between the solar towers and the power block are discussed in Section 10. This paragraph is dedicated to outline the main characteristics of the particle handling system with sufficient accuracy to then assess its cost.

About 220 kg/s of particles must be conveyed between the storage system and each receiver: horizontally as described above, and vertically: from ground level to the receivers and to the discharge height of the particle hoppers. To lift the particles from ground level to the receivers, skip hoists have their merits [173]; however, bucket elevators were eventually chosen because they work almost continuously, thereby reducing the buffer storage required at the top of the tower. Due to limitations of lift height and mass flow, four elevators are required for each tower (two in parallel x two in series). As for the horizontal conveying of the particles between the storage and the towers, railway wagons and apron conveyors were first considered but continuous-flow conveyors were eventually chosen. Some manufacturers can build equipment that withstand the particle temperatures (resp. 620 and 820 °C to and from the receivers). The power consumption of the particle handling system, about 3.5 MW_e, is supplied by a PV farm and a buffer battery. The thermal losses along the conveyors can be limited to max. 2.5% through proper engineering practices, but that is still a significant penalty.

In order to make efficient use of the particle temperature (about 800 °C), an externally heated combined cycle gas turbine was chosen (supercritical steam and CO₂ Brayton cycles are also good candidates, as discussed in Section 6). The bottoming steam cycle is standard: three pressure with reheat and air-cooled condenser. Due to the low Turbine Inlet Temperature (TIT) compared to that of an internal combustion gas turbine (780 °C vs. up to ~1600 °C), a double reheat configuration is required to reach an efficiency of 48.6% [17,218]. The general architecture of the turbine is shown in Fig. 30. The electric output of the gas and steam turbines are 81 and 74 MW_e respectively. Pressure drops –

highly detrimental to the performances of Brayton cycles – as well as temperature differences of the particle-air heat exchangers (HEXs) must be limited. Due to the moderate pressures, air densities are low; therefore, these two combined requirements translate into bulky and costly HEXs. In practice, two HP HEXs, three IP HEXs and five LP HEXs are arranged in parallel; single HEXs would be too wide relative to their length. A tentative arrangement of the powerhouse (gas and steam turbines with common generator, HEXs, air piping, and particle paths) is shown in Fig. 30.

The heat recovery steam generator, the powerhouse and the air-cooled condenser are aligned (in that order) on the N-S axis of symmetry of the solar island. Two hoppers (one cold and one hot) are located on the west side of the powerhouse, the two other hoppers being symmetrically located on the east side. This layout is shown in Fig. 31.

10.2. Design of the medium-scale particle-based plant (25.3 MW_e)

As shown in Section 6, the only cycle that can be considered relevant for a ~25 MW_e scale while being industrially mature is a small subcritical steam cycle with no reheat. As particles do not suffer from the same temperature limitations as molten salts, the main parameters of the steam cycle can be improved in order to increase the conversion efficiency. The cycle studied here therefore has a main steam temperature and pressure of 600 °C/180 bar. The simulation of such a cycle using the thermal engineering software SteamPRO 29 gives a gross efficiency of 39.6% for a net efficiency of 36.6%. That relatively low efficiency, compared to those given in Section 6, is mainly due to the lower turbine efficiencies that can be expected in smaller power cycles.

The particle temperatures required to heat the steam Rankine cycle are more moderate than at full-scale: particles cycling between 400 and 700 °C allow for a comfortable temperature difference in the steam generator, while leading to efficiency gains at the receiver. With a field similar to that of Fig. 29a and the same receiver geometry as for the large-scale plant, the receiver’s thermal losses (essentially due to radiative heat transfer) are halved thanks to the substantially lower working temperatures, which leads to a higher thermal power of 66.5 MW_{th}. Given the specific heat of olivine (1.22 kJ/kgK) and the temperature range envisioned, that leads to a nominal particle flowrate of 182 kg/s in the receiver and the conveyors feeding it. Considering the same solar resource (i.e., that of Ouarzazate, Morocco), the solar loop can accumulate 333 MWh_{th} in the thermal energy storage 60% of the time in a typical year. Sizing it for the 90th best day leads to a 400 MWh_{th} thermal energy storage, that is 3900 t (1950 m³) of particles. Two hoppers (one hot, one cold, height: 16 m, external diameter: 16 m) are enough to store that volume of particles.

Thanks to the collection of heat by only one tower, the total length of conveyors is drastically reduced (estimated to around 100 m of horizontal conveyors, essentially between the power block and the hoppers).

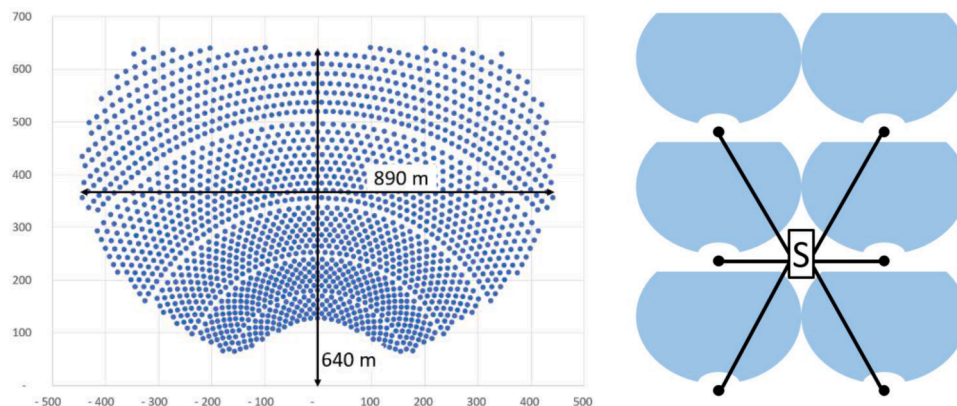


Fig. 29. (a-left) Individual solar field | (b-right) Layout envisioned for the solar island.

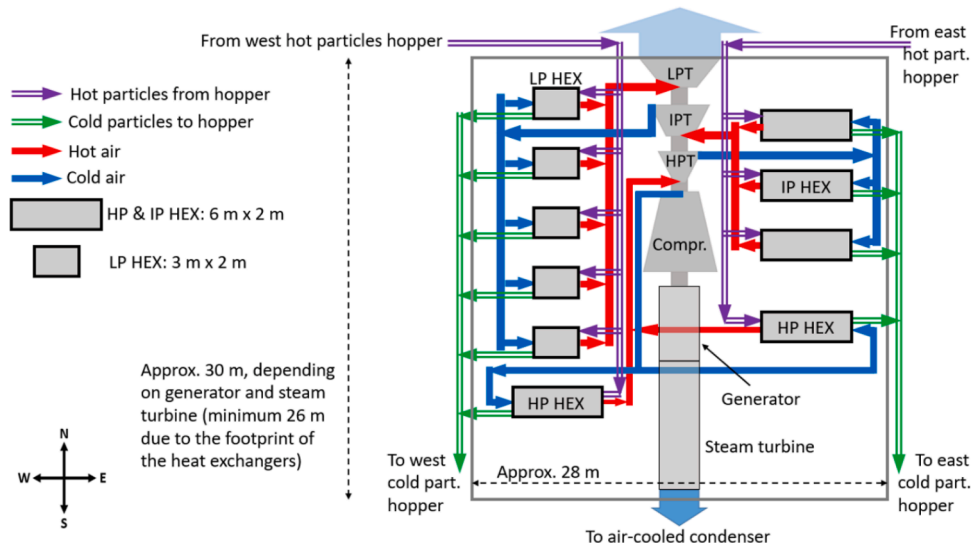


Fig. 30. Arrangement of the powerhouse including its approximate dimensions.

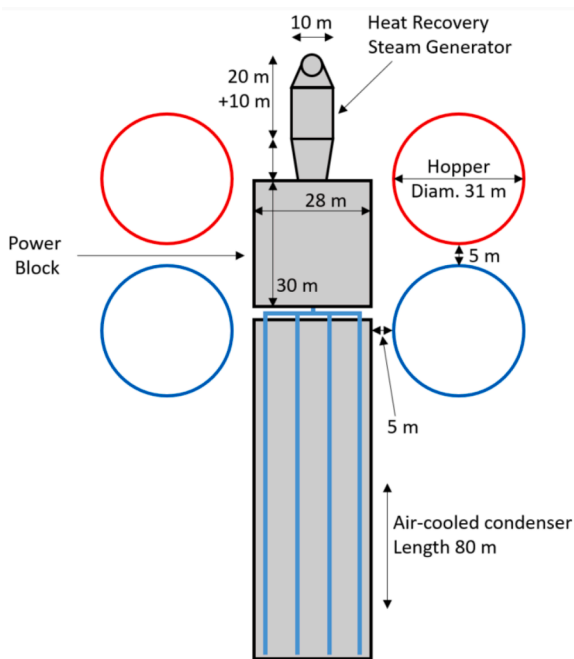


Fig. 31. Layout of the whole power island plus the four particle hoppers.

The thermal losses due to conveying, fluidization in the exchangers are therefore themselves reduced: a conservative value of 1% is assumed, which results in 329 MWh_{th} available for the power block if 333 MWh_{th} are collected. The dispatch strategy assumed for the large-scale plant can be used with the same reliability (that is 4h20 at full load, on at least 280 days in a typical year) if the cycle's nominal thermal input is 69.4 MW_{th}. Given the abovementioned conversion efficiency, the cycle's net power output is 25.3 MW_e, taking into account the power consumption of the condenser fan, feedwater pump, condensate pump and all the auxiliary consumption linked to particle handling during power production. Similarly to the large-scale plant, a small photovoltaic farm (320 kW) including buffer batteries is dedicated to the particle elevators that work only by day.

10.3. Levelized cost of electricity generated by the plant

10.3.1. EPC cost of the solar island

According to [284], the cost of heliostats were expected to decrease from US\$ 143/m² in 2015 to US\$ 103/m² in 2020. An exponential extrapolation gives US\$ 87.4/m² in 2030. As indicated in [297], up-to-date heliostat costs are difficult to find, so that optimistic trend cannot be verified. It has however a limited impact on the present comparison as the same assumption is used for both the particle plants and the benchmark plant. With 1879 heliostats of 48.5 m² each, the cost of the medium-scale heliostat field is US\$ 8M. With six modules, and assuming no scale effect, the cost for the large-scale plant is US\$ 47.8M.

Due to the architecture of the receiver system, the tower's top is 6.5 m above the center of the solar panel; moreover, the heliostat mirrors are 4.5 m above ground. Therefore, a 126 m height difference from heliostat mirrors to receiver panel mid-height corresponds to a tower height of 126 + 6.5 + 4.5 = 137 m. The weight of the receiver in operational conditions (i.e., particles included) is about 90 tons. Given these parameters, one tower costs US\$ 3.9M; since building six identical towers on the same site only allows for a 10% cost saving, the six towers cost US\$ 21.0M.

In [284], the 2015 total costs for a state-of-the-art molten salt receiver is estimated at 125 US\$/kW_{th} and potentially at US\$ 100/kW_{th} by 2025. Let us compare the UBFB receiver with a molten salt receiver: since the average fluxes are similar, so are the size of the tube panels; in both receivers, the receiver tubes are the only components made of Nickel-based superalloys; therefore, they contain approximately the same mass of superalloy (about 8 to 10 times costlier than austenitic stainless steel [298]). The UBFB receiver does not require heat tracing or emergency drainage process (requiring pressurized buffer tanks), but handling a fluidized bed raises more challenges than a circulating a liquid. Overall, it is assumed that in 2030 the cost of a UBFB receiver will be similar to that of the 2025 cost of a molten salt receiver or US\$ 100 /kW_{th}, which means US\$ 6.7 M for the medium-scale plant's receiver, US\$ 33.7 M for the six receivers of 56.2 MW_{th} each in the large-scale plant. Considering the above, the cost of the solar island is US\$ 8.0M + 3.9M + 6.7M ≈ 18.6M for the medium-scale plant, US\$ 47.8M + 21.0M + 33.7M ≈ US\$ 102.5M.

Thoroughly comparing the cost of the large-scale, multi-tower solar island with that of a molten salt single tower of equivalent capacity would be out of the scope of this study. The multiple tower architecture allows for higher towers relative to the size of each individual solar field, thereby increasing optical efficiency and reducing the heliostat area; on

the other hand, six towers should be somewhat costlier than a single tower. For the sake of simplicity, it is considered that these two impacts compensate each other; taking into account the downsizing of the receiver and heliostat field in inverse proportion with the net cycle efficiencies (~43% vs. 48.6%), the solar island is about US\$ 10.6M cheaper than that of a molten salt tower of similar power output.

10.3.2. EPC cost of the particle handling system

The four bucket elevators required in the medium-scale plant (each with a 180 kg/s capacity and a 70 m lift) cost ~US\$ 1.2M plus US\$ 0.3M for supporting / access structure and thermal insulation. An additional elevator towards the cold hopper is necessary, with a capacity of 190 kg/s and an 18 m lift. Its cost is estimated to US\$ 60k. Adding ~10% for electric cabinets and cabling, the cost of the vertical handling for the medium-scale plant is: US\$ 1.8M.

Due to their higher capacity (220 kg/s), the large-scale plant's bucket elevators are slightly more expensive: ~US\$ 1.3M for each tower, plus US\$ 0.3M for supporting/access structure and thermal insulation. With the same ~10% extra cost for electric cabinets and cabling the cost of the vertical handling for the 6 towers is US\$ 10.6M.

Regarding the horizontal conveying: the conveyors cost US\$ 900/m (one-way) or US\$ 1400/m (round trip) plus US\$ 500/m for thermal insulation and underground concrete trench. In the medium-scale plant, this amounts to US\$ 150k, plus US\$ 30k for the electric motors and an additional 10% for electrical equipment and instrumentation. The overall cost of the conveying system can be rounded to US\$ 200k.

Regarding the large-scale plant, the total 4 km of roundtrip conveyors amount to US\$ 7.6M, plus US\$ 1.3M for the electric motors, then 10% for electrical and instrumentation equipment, that is about US\$ 9.8M for the horizontal conveying between the hoppers and the towers. The conveying system that links the hoppers to the particle-air heat exchangers located in the power house has short horizontal distances but is quite complex, as shown in Fig. 6–2: it costs about US\$ 1.0M. The overall cost of the conveying system is therefore US\$ 21.4M.

Besides, the medium-scale system is powered with a 320 kW PV farm and a 320 kWh/330 kW battery with a rounded overall cost of US\$ 300k (2030 costs: ~US\$ 350/kW for PV and ~US\$ 120/kWh + ~US\$ 380/kW for storage [282]). The overall cost of the conveying system is therefore US\$ 2.3M.

At the larger scale, they become a 3.5 MW_e PV farm and a 3.5 MWh/3.6 MW battery with an overall cost of US\$ 3.0M. The cost of the whole particle handling system is therefore US\$ 24.4M.

In comparison, the set of molten salt pumps (including the variable frequency drives and the piping) of a tower of similar power output is about US\$ 4.0M. The thermal power of the particle CSP plant without accounting for the thermal losses of the particle handling is 320 MW_{th}; given its net conversion efficiency (~43.0% instead of 48.6%), the molten salt tower needs 363 MW_{th}. Given the average specific heat of solar salt (~1.52 kJ/kgK at 430 °C) and considering a 270 K temperature difference, a tower height of 200 m, and 80% for the combined efficiencies of the molten salt pump and motor, one determines the mass flow of solar salt is (885 kg/s) and the consumption of the molten salt pumps: ~2.2 MW_e. A 2.5 MWh/2.5 MW PV + battery farm is required; it would cost US\$ 2.2 M. The overall cost is therefore US\$ 4.0 + 2.2M = US\$ 6.2M. This is US\$ 23.6 M cheaper than that of the particle handling system.

10.3.3. EPC cost of the storage system

According to [284], the 2025 cost of the 2 GWh_{th} storage system of a typical molten salt tower can be broken down as shown in the second row in Table 15 (it should not decrease much further by 2030). The cost of the particle storage is broken down in the last row and was determined as follows:

- Storage medium: with the amount needed in an industrial context, it is reasonable to estimate the cost of olivine at about US\$ 120/t.

- Hoppers: an external quotation was used for the large-scale hoppers. Despite the need for higher mass (+75%) and volume (+57%) of olivine for the same storage capacity, our hoppers being slightly cheaper than molten salt tanks should come as no surprise since they have no corrosion and tightness issues. A conservative exponent 0.5 (applied to the volume of particles stored in each hopper) was assumed for the extrapolation to medium scale
- Balance of plant: the costs are considered identical between molten salt and particle plants at large scale, and extrapolated proportionally to the storage capacity for the medium size.

Eventually, as shown in Table 15 above, the particle storage system costs US\$ 23.2M at large-scale, US\$ 5.2M at medium scale.

10.3.4. EPC cost of the steam generator / particle-air heat exchangers

Further to initial market consultations within the European Union at the common and average costs of AISI 347H (high temperature applications) and AISI 316 L (cladding, reinforcements, supports), raw materials (as pipes, sheets, L-profiles), current manufacturing costs (including drilling, welding, pressure testing among others) can be estimated at 165 k€ for the medium-scale plant's economizer (383 tubes, outer / inner diameters 38.1 mm / 32 mm, length 6 m), 150 k€ for an evaporator (175 tubes, outer / inner diameters 50.8 mm / 42.4 mm, length 6 m) and 375k€ for a superheater (564 tubes, outer / inner diameters 50.8 mm / 41.2 mm, length 6 m).

Similarly, the large-scale plant's costs are 485 k€ for a HP/IP heat exchanger (3400 tubes, outer / inner diameters 29 mm / 25 mm, length 6 m), and 240 k€ for a LP heat exchanger (2160 tubes, outer / inner diameters 44 mm / 40 mm, length 3 m).

The fluidized beds themselves, with internal AISI 347H shell, ceramic insulation and outer AISI 316 L cladding, and the multi-tubular multi-orifice distributors represent an added cost of approx. 200,000 € for the medium-scale steam generators, 1 M€ for the large-scale plant's combined cycle.

The total manufactured costs of the medium-scale steam generator will hence approximate 900 k€, while the large-scale plant's 5 + 5 heat exchangers are estimated to 4.6 M€.

According to [10] and [11], additional costs will relate to the instrumentation and controls, wiring of the instrumentation and controls, blank testing, fluidization blowers and exhaust gas filtration at respectively 15%, 5%, 5%, 12 and 10 % respectively (or 47% in total). The total not-installed investment is hence estimated at about 1.3 M€ at medium scale, 7.0 M€ at large scale. Considering a long-term power purchase parity €/US\$ exchange rate of 1.30, the cost of the particle-air heat exchangers (complete with its air fluidization equipment) costs approx. US\$ 1.7M for the medium-scale steam cycle, US\$ 9.1M for the large-scale, externally heated combined cycle.

In comparison, the steam generator of a molten salt tower of similar power output is about US\$ 7.0M.

10.3.5. EPC cost of the power cycle

The cost of the medium-scale plant's steam cycle (excluding the steam generator estimated above) is estimated with the specialized engineering software Steam PRO developed by Thermoflow Inc, based on a

Table 15

Cost breakdown of 2 GWh_{th} molten salt (MS), 2 GWh_{th} olivine particle and 400 MWh_{th} olivine particle storages.

	Storage medium	Tanks / Hoppers	Balance of plant	Total
2 GWh _{th} MS storage system (US\$ M)	18.8	18.0	3.6	40.4
2 GWh _{th} particle storage system (US\$ M)	3.6	16.0	3.6	23.2
400 MWh _{th} particle storage system (US\$ M)	0.5	4.0	0.7	5.2

complete list of main and auxiliary equipment. It amounts to US\$ 46M.

As for the large-scale plant's combined cycle, such a cycle does not exist to date; its estimation is therefore performed by comparing the gas turbine with a conventional, internal combustion turbine rated at sea level with an ambient temperature of 15 °C (ISO conditions): 1/ combustion – one of the most challenging issues on modern gas turbines – disappears, hence a ~20% cost reduction; 2/ the double reheat (first-of-a-kind, but single reheat Ansaldo GT24/26 gas turbines are well-proven) should increase the cost by ~10%; 3/ no internal cooling, thermal barrier or top-grade superalloys are required, hence a ~15% cost reduction; 4/ the ISO rating of the gas turbine (but not that of the generator) must be increased by about 20% to deliver the required power output in Ouarzazate (barometric pressure 882 mbar, average temperature during operation ~25 °C), which increases its cost by about 10%. Overall, the cost of the gas turbine is 0.82 times that of a conventional one with the same power output rated at ISO conditions.

The impact of the dry cooling on the steam cycle is ~5% less power output and 7% more Capex; therefore, the 70 MW_e steam cycle corresponds to an ISO-rated 73.7 MW_e (70.0/0.95) steam cycle whose cost is multiplied by 1.07. This steam cycle is an ISO-rated 221 MW_e regular combined cycle (2/3 gas turbine, 1/3 steam cycle) minus its conventional 147 MW_e gas turbine.

The cost of the combined cycle can therefore be determined as follows:

$$\text{Cost PowerCycle} = 1.07 (\text{Cost}_{221\text{MW CombCycle}} - \text{Cost}_{147\text{MW GasTurbine}}) + 0.82 \text{Cost}_{80\text{MW GasTurbine}}$$

Using interpolation curves from [217] for ISO-rated combined cycles and simple cycle gas turbines as a function of the power output, one determines the cost of the power cycle: US\$ 171M. This cost (US\$ 1140/kW_e) is very similar to that of the steam Rankine cycle of a molten salt tower with the same power output t [18,284]. The higher cost of the medium-scale steam Rankine cycle (US\$ 1820/kW_e) is essentially due to its smaller size (25 vs. 150 MW_e) and lower efficiency .

10.3.6. Capex of the turnkey plant

All the costs determined above as well as the corresponding

references (if applicable) are summarized in Table 16 below. The sum of the abovementioned costs respective to the medium-scale particle plant's subsystems is US\$ 72.1M. For the large-scale particle plant it is US\$ 330.2M. Adding 2% for balance of plant and interconnection as well as instrumentation and control, then 2% again for site preparation, one obtains the direct Engineering, Procurement and Construction (EPC) cost of each plant: US\$ 75.0M (medium-scale) US\$ 343.4M (large-scale). In a manner consistent with various sources such as [x], the following must be added to the EPC cost of the plant: 10% for indirect EPC costs (Engineering, management, contingencies, etc.) and 10% for owner's costs (land, infrastructure, etc.). The Capex of each turnkey plant are therefore US\$ 90M (medium scale) and US\$ 412.1M (large scale). That corresponds to US\$ 3560/kW_e and US\$ 2750/kW_e respectively.

Table 16 also summarizes the cost deviations between the large-scale plant studied and a similar molten salt tower, both being built in 2030 with the same dispatch strategy under similar site conditions. The turnkey Capex of the plant is US\$ 9.3M or 2.2% lower than that of the molten salt tower (US\$ 421.4M).

10.3.7. Levelized cost of energy (LCOE)

A 5% real (i.e., nominal minus inflation) discount rate and a 25-year lifetime are considered, which corresponds to a discounted lifetime of 14.5 years. Assuming that 1500 full load hours of power generation are performed per year, the discounted generation during the plant's discounted lifetime is therefore 550 GWh (medium scale) / 3.26 TWh (large scale). The LCOEs corresponding to the amortization of the turnkey Capex of each plant are therefore US\$ 90.0 × 10⁶ / 0.55 × 10⁶ MWh = US\$ 163.6/MWh (medium scale) US\$ 412.1 × 10⁶ / 3.26 × 10⁶ MWh = US\$ 126.4/MWh. It is US\$ 129.3/MWh for the comparable molten salt tower if one considers that the discount rate is the same for both plants. This is a rather strong assumption: in practice, investors ask for higher interest rates (on both equity and debt) for less mature technologies, which has a major impact on the LCOE. However, this assumption was retained in order to compare the two technologies based on their respective techno-economic merits, independently of any financial considerations.

According to [301], the O&M costs for molten salt towers range from

Table 16
Breakdown of the plants' Capex into subsystems' and other costs (in US\$ M).

Subsystem	Medium-scale particle plant	Large-scale particle plant	Benchmark	Difference between large-scale particle and molten salt plants	References
Solar Island	18.6	102.5	113.1	- US\$ 10.6M	
Heliostat field	8.0	47.8	54.0		[284]
Towers	3.9	21.0	21.0		Engineering company
Solar receivers	6.7	33.7	38.1		[284]
Particle handling	2.3	24.4	6.2	+ US\$ 18.2M	
Vertical hoppers-towers	1.8	10.6	Molten salt pumps 4.0		Various manufacturers
Horiz. hoppers-towers	-	9.8			Various manufacturers
Hoppers-Power house	0.2	1.0			
PV farm + battery	0.3	3.0	2.4		
Storage system	5.2	23.2	40.4	- US\$ 17.2M	
Particles	0.5	3.6	MS 18.8		Supplier
Hoppers	4.0	16.0	Tanks 18.0		Construction company
Balance of plant	0.7	3.6	3.6		[284]
Cycle hot source	1.7	9.1	7.0	+ US\$ 2.1M	[299]
Power cycle	46.0	171.0	171.0	~ 0	Large scale : [217] Medium scale : Steam PRO (ThermoFlow)
Sum of the above (1)	72.1	330.2	337.7		
BOP/I&C/Site preparat.	+4%				
EPC cost	75.0	343.4	351.2	-2.2%	
Indirect EPC costs	+10%				
Owner's costs	+10%				
Capex of turnkey plant	90.0	412.1	421.4	-2.2%	[217,275,300]

US\$ 11/MWh to US\$ 27/MWh, with US\$ 21/MWh for the US and US\$ 12/MWh for Morocco. The O&M costs given by various other sources such as [275,284,300] for a molten salt tower built in the US need some treatment to be reconciled, but US\$ 19–21/MWh and US\$ 12/MWh are good estimates of the O&M costs of a typical molten salt tower built in 2020, respectively in the US and in Morocco. This US\$ 12/MWh figure is adjusted to US\$ 12.5/MWh as follows:

- It corresponds to a mid-peaker with a capacity factor of 50–55% vs. 17.1% for the plant studied that is a peaker: its power cycle is about three times bigger for the same yearly power generation. It adds ~US\$ 4/MWh to the O&M cost. This cost adjustment is about the plant being a peaker, not about particles vs. molten salt technologies. It does not affect the comparison between the particle tower and the molten salt tower.
- It is assumed that future improvements of O&M practices will lower this figure by 22% between 2020 and 2030 [272].
- The O&M costs of the particle handling system would be about 8% of its Capex per year if it were operating round the clock throughout the year: Systems dealing with particles are costlier to operate and maintain than systems circulating fluids. However, the particle handling works when the solar island is in operation, that is, no more than 12 h per day. The handling devices connected to the power cycle works ~6 h/day, but is a minor part of the whole system. Therefore, the 8% mentioned above can be reduced to 4%. This is US\$ 92k per year (US\$ 2.42/MWh) at medium scale, US\$ 0.976M per year (US\$ 4.34/MWh) at large scale. The O&M costs of the molten salt pumping system that is replaced by the particle handling system is about 1% of the Capex, which results in an avoided O&M cost of US\$ 0.28/MWh. Eventually, the extra O&M costs corresponding to replacing the molten salt pumps with the particle handling system is US\$ 2.14/MWh (medium scale) to US\$ 4.06/MWh (large scale). Once again, the difference between medium and large scale plants arises from the multi-tower architecture of the large-scale plant, that makes long-distance horizontal conveying necessary.

The resulting O&M costs of the particle plants studied are US\$ 14.64/MWh (medium-scale) and US\$ 16.56/MWh (large-scale), vs. US\$ 12.5/MWh for the benchmark molten salt tower.

By adding the Capex amortization and the O&M costs above, one eventually obtains the estimated LCOE of each plant: US\$ 178.24/MWh (medium scale) / US\$ 143.0/MWh (large scale). In comparison, the LCOE of the benchmark large-scale molten salt tower is US\$ 141.8/MWh.

10.4. Final considerations

In the previous estimates, the plants using fluidized particles and the benchmark molten salt tower are peakers whilst the LCOE of CSP is typically given in the literature for plants with much higher capacity factors: generally above 50%, in [272] for example. Since peaker CSP plants have bigger power cycles for the same yearly power generation, the fact that the LCOEs assessed in this study are higher should come as no surprise. Regarding LCOE comparisons, what really matters is:

- Peaker CSP plants vs. non-CSP alternatives fulfilling the same service to the electrical networks. This is dealt with in Section 8.
- The CSP plants studied here, using fluidized particles, vs. the benchmark that is a molten salt tower with a subcritical Rankine steam power cycle.

The main takeaways are as follows:

- The LCOEs of both large-scale power plants can be considered equal: the difference, less than 1%, is well below the uncertainty margin.

- The Capex of the large-scale plant studied is only 2.2% lower than that of the benchmark: the solar island is cheaper thanks to the improved conversion efficiency of the power cycle, the storage is much cheaper, but all this is significantly offset by the cost of the particle handling system. The multi-tower architecture is necessary with this receiver technology, hence the multi-kilometer horizontal conveying system. Lifting the particle at receiver level is no easy task either. The thermal losses are another penalty.
- Despite the considerable limitation of the particle handling issue at medium scale, thanks to a single tower architecture, the 25 MW_e version of the particle plant has both higher Capex and LCOE, essentially due to the modest performance and high specific cost of its small power block.
- The O&M costs of the particle handling system are high, which offsets the limited gain in Capex at utility scale, compared to the benchmark.

To summarize, the individual receiver size limitation prevents the concept studied to allow for a lower LCOE than the benchmark: in a medium-scale, single tower architecture, the power block is typically too small to reach acceptable technical and economic performances. At utility scale, the particle handling system has to be considerably expanded and becomes penalizing. The latter issue can be mitigated by replacing the externally heated combined cycle envisioned here by a high-performance supercritical steam cycle (see Section 4), that would allow for approx. doubling the temperature range of the particles and lowering their temperature by about 100–150 K. The mass flow rate and the relative thermal losses of the particle handling system would be divided by two and its cost approx. by four. The cost of the storage system would be further reduced. The efficiency of the receiver would be higher, thereby compensating (and possibly beyond) for the somewhat lower efficiency of the power cycle. The extra cost of the power cycle should be limited to 5–7% maximum (~US\$ 10M). Overall, such a change is expected to lower significantly the plant's LCOE. Any improvement aiming at downsizing or removing some particle handling subsystems should be considered a way to decrease both thermal losses and investment costs.

11. Conclusions

Section 1 introduced the reader into the field of Concentrated Solar Power (CSP). In favourable regions with direct normal irradiation (DNI) equal to or exceeding about 2000 kWh/m² year. The built-in thermal storage capabilities of CSP plants are a decisive asset that distinguishes these plants from highly variable renewable electricity production technologies like PV or wind power. In this context, concentrated solar power plants with 7–14 h storage capacity offer the opportunity to install a base-load power generation facility with a capacity factor of approximately 70 % and a cost of heat storage in the range of 40–50 €/kWh_e (for solar towers), i.e., much cheaper than battery storage. CSP can also be envisioned as a peaker power facility operating only with thermal storage as a complement to PV plants. Such CSP facilities deliver electricity during 5 to 6 h at the end of the afternoon and after sunset when PV production without storage declines to zero. The two strategies are discussed in Section 7 of this paper.

Currently, molten salts are widely used as HTF in CSP applications. The main reasons for the enhanced development of novel heat transfer media are related to overcoming the specific and overall drawbacks of molten salts, relating to their solidification temperature (~220 °C) and temperature of decomposition (>600 °C). The use of gas/solid suspensions, i.e., powders, as heat transfer media has hence attracted an increasing interest for CSP applications, since moving into higher temperatures has significant effects on the applicable thermal storage and on the used thermodynamic cycles in the power block.

Section 2 provided a review of the fundamentals of particle technology in view of its CSP application. Essential gas/solid parameters,

including the Geldart powder classification, were summarized and the gross behavior of particle/gas systems was reviewed. Available literature on heat transfer was summarized through empirical correlations. Vertical upflow systems were evaluated, with a special attention to previous experiments of such upflow system toward solar tower applications. The survey of the current particle-driven solar receivers classified them according to the characteristics of direct or indirect heating of particles; continuous particle flow or batch processes; and types of solid-gas contacting and mixing modes. In addition, inert or reactive particles may be added to the previous list since many developments have been achieved in the field of solar thermo-chemistry for solid-gas reaction processing. The various developments were illustrated and discussed.

Direct absorption solar receivers can accept a higher flux density than indirect absorption concept due to the limited value of the wall-to-particle heat transfer coefficient and of the operating temperature of the absorber tube walls. Typical values are 1 MW/m^2 for the former and 0.5 MW/m^2 for the latter. Construction material issues are identified for the three most-developed solar receivers: back wall for the falling particles, kiln wall for the CentRec and tube wall for the UBFB concept. The falling particle receiver is the most sensitive to particle attrition due to the high impact velocity of the particles at the end of their fall. CentRec and UBFB are sensitive because of the low particle velocity involved. Particle loss is a critical issue for open direct absorption particle receivers due to temperature and wind effects on particle flow stability. Scaling up ability to large scale, typically some $100 \text{ MW}_{\text{th}}$, is examined in Sections 7 and 10.

Section 3 selected the most appropriate conveying and storage systems. The solids heated in the solar receiver are transferred to the thermal power block and stored before their use. In turn, the cooled solids leaving the power block are stored before being transferred back to the solar receiver to be reheated. The typical solar tower will be between 100 and 200 m high, and the power block is at ground level. Consequently, in addition to moving the solids horizontally, they also have to be moved vertically. As a result of the assessment apron and side-pulled mass conveyors were proposed for the long-distance horizontal conveying, whereas apron conveyors, bucket elevators, and dense-phase pneumatic conveying seem the most appropriate candidates for vertical conveying. Screw conveyers are applicable for short-length transfer of the powders.

For the storage of the hot and cooled powders the construction requirements were discussed, together with its auxiliaries (valving, and dust control). The conveying and storage part of the CSP plant are crucial items and the operation at high temperatures and transferring large quantities of powders around the loop certainly need further mechanical, thermal, and particle flow research, that is a recommended as a priority development topic.

Section 4 examined the particle-to-working fluid heat exchanger as a key component of the particle CSP concept. Being the equipment that usually withstands the highest pressure and temperature in the thermodynamic cycle, the primary heat exchanger (or set of heat exchangers, depending on the cycle) is of almost importance to the plant's performance and economics. Due to the difficulty to pressurize high quantities of particulate solids and to efficiently separate the particles from a fluid, the heat transfer from particles to the working fluid is not considered feasible via direct contact, despite the typically high efficiency of such a solution. Particle-to-working fluid heat exchangers are therefore selected to be of an indirect mode and can be divided into fluidized-bed heat exchangers and moving bed heat exchangers. While fluidized-bed exchangers are generally the preferred solution thanks to their higher heat transfer coefficient, moving packed beds can be used for bigger or denser particles whose fluidization would be heavily penalized in terms of thermal losses and auxiliary consumptions.

Considering the high complexity of the phenomena involved, their importance in the overall plant's reliability and economics, and the lack of predictive models consolidated with experiments and industrial experience, particle heat exchangers should remain a key R&D subject in

the years to come.

Section 5 presents a detailed review of the advanced cycle technologies candidates for integration with particle-CSP, including supercritical steam cycles, combined cycles and sCO_2 cycles. Thermodynamic cycle characteristics, efficiency, operational flexibility, material issues and technology readiness level are discussed. The efficiency of the three technologies is similar, $\sim 48\%$. On the one hand, the combined cycle needs a higher TIT than the steam and CO_2 cycles to achieve interesting efficiencies and, on the other hand supercritical cycles need very high pressures. Ultra-supercritical steam cycles offer the opportunity to a better use of the thermal storage by an increase of approximately two-fold the temperature difference between the hot and the cold storage with respect to combined and sCO_2 cycles.

The steam generator of the benchmark/subcritical steam cycle and the high-pressure stage of the bottoming cycle of the combined cycle should be once-through for higher flexibility. The steam generators of the supercritical steam cycles are ipso facto once-through. Therefore, the operational flexibilities should not be very different; probably slightly higher for the combined cycle and slightly lower for the supercritical steam cycles. The supercritical CO_2 cycle should be the most flexible of all, although this remains to be proven. In the tentative techno-economic assessment presented in Section 10, specific cycles were selected for a detailed example. Other options (e.g., supercritical steam or CO_2) could however be assessed similarly.

Section 6 deals with the scale-up procedures in the particle-driven CSP systems, upscaling the three most mature technologies of falling film, centrifugal and UBFB receivers. For particle-driven CSP systems, the three most developed technologies (falling film, centrifugal particle receiver and fluidized particle-in-tube) have reached TRL5, in particular concerning the solar receiver that is the most critical component. In addition to the particle solar receiver, the particle handling system and the particle heat exchanger are the two other sub-systems for which scaling up issues must be examined carefully. They are discussed in Section 4 and 5. Consequently, this section addresses mainly the scaling-up of the solar receiver and the integration issues. Concerning the solar receiver, typical thermal powers are 10–100 kW for step 1 (TRL4), 100–1000 kW for step 2 (TRL5&6), 5–10 MW for the demo-unit and approximately 50 MW for a FOK unit.

Among the thermodynamic cycles discussed in Section 5, only steam Rankine cycles and supercritical CO_2 Brayton cycles are realistically applicable at a scale relevant for a $\sim 50 \text{ MW}_{\text{th}}$ receiver as the technical and economic performance of combined cycles is too degraded at that scale. CO_2 cycles show very promising performance at small scale ($< 30 \text{ MW}_e$) but their techno-economic performance is to date much more uncertain than that of steam cycles. At utility scale (100 MW_e and more) the multi-tower concept with N solar tower modules (or solar islands) sharing the same particle storage and power block was examined by the authors.

As thermodynamic cycles typically draw significant benefits from scale efforts (both in terms of efficiency and specific Capex), the thermal energy storage and the power block are centralized. Considering the high Capex and thermal losses expected from long distance high-temperature conveying (discussed in Section 3), the positioning of each individual field and of the power block + thermal energy storage island has to be optimized in order to minimize the total length of conveyors. All the auxiliary power of the solar loop is considered to be provided by a small PV farm with a buffer battery, whose production is typically synchronized with the working time of the solar loop.

Section 7 looks at the enhanced potential of CSP plants used as peaker, rather than as baseload plants. Even though base-load CSP plant are regularly mentioned as viable options, it will usually be optimal for the electrical systems to use CSP plants as peakers (or perhaps mid-peakers in some contexts) that typically generate power during four to six nighttime hours per day. It was shown that, (1) utility-scale batteries charged mainly by photovoltaic power is the only alternative to CSP; (2) today, its LCOE is similar to that of CSP for four hour per day of peak

shifted generation, but is higher for mid-merit (i.e., more hours per day) generation; (3) CSP will remain competitive in 2040 provided it benefits from substantial improvements; (4) It is more expensive today and will still probably remain so in 2040.

A cost analysis of renewable power shifted with batteries and the economic comparison of electrochemical storage and CSP thermal storage demonstrate that the future will be challenging for CSP.

The LCOE of a PV + batteries plant that shift all its generation during four nighttime hours is US\$ 208/MWh, vs. US\$ 201/MWh for a molten salt tower – the current benchmark of CSP plants – with the same dispatch strategy. However, CSP has probably a more significant advantage in developing countries. This comparison indeed applies to the US whose local costs (labor, regulations) are among the highest in a developing country. The CSP solution would benefit significantly more from cheaper local labor costs: local construction and O&M costs of a CSP plant proportionally are much higher than those of a PV + battery power plant.

The future will be challenging for CSP: its LCOE must decrease to remain competitive with that of PV farms equipped with batteries:

- CSP will most certainly remain competitive if the “high” battery cost scenario prevails,
- With the “medium” battery cost scenario, which is also the most likely, CSP will remain competitive provided significant improvements are performed: incremental ones and, if possible, technological breakthroughs. In the light of the recent past, it seems perfectly feasible.
- If the “low” battery cost scenario prevails, the competitiveness of CSP will be an uphill battle: significant technological breakthroughs (such as using particle circulation loops for CSP) are the only option.

It is however important to stress that the techno-economic comparison of the CSP versus PV with batteries concepts, with the same power supply capacity and the same environmental footprint, is tentative and open for further consideration. From an environmental point of view, these two technologies are far from being equivalent, especially regarding the impacts of their manufacturing processes.

Section 8 develops the use of alternative fuel-based resources as back up fuel in the CSP plants for non-sun periods. Biomass and other alternative fuels are widely available in some countries. Biomass, its pyrolysis/gasification or its bio-methanation derivatives can be readily applied in a hybrid CSP. Literature data are complemented by current operation data of a 22.5 MW_e hybrid CSP plant, called Thermo Borges (Spain).

Although the described examples illustrate the potential of hybridizing CSP and alternative fuels, it is obvious that the solution is viable only in geographic regions with high solar irradiance when the CSP can provide a considerable share of the total power, and provided alternative fuels are available. If these conditions are not met, a hybrid concept should not be envisaged.

Section 9 discussed the authors' views concerning some important and required future research and development topics. Enhancing the particle-to-tube heat transfer coefficient in the particle-to-working fluid heat exchanger, so as to reduce the particle-related heat transfer resistance is of primary importance. Finned tubes considerably increase the heat transfer coefficient ($>> 2 \text{ kW/m}^2\text{K}$). The overall heat transfer is determined by the wall-to-in-tube working fluid flow.

Considering the maximum achievable solids flux in the vertical upflow systems, operation of the upflow bubbling fluidized bed at G -values in excess of $150 \text{ kg/m}^2\text{s}$, requires superficial air velocities to exceed 0.17 m/s . Particle attrition and equipment erosion by moving particles must be avoided or limited.

Extended surface finned receiver tubes should be investigated. Although experimental evidence in short tubes provides a possible gain of heat transfer coefficient, this needs to be confirmed in long tubes in view of different gas/solid conveying modes.

In general, the particle conveying within the CSP loop needs

additional R&D. Conveying particles at very high temperature and flow rates in the hot part of the loop needs to be fully investigated, although the preliminary selection of mechanical conveying systems offers potential solutions. The application of dense-phase pneumatic conveying of the hot particles merits an in-depth assessment in view of its non-mechanical and scalable nature, and of its expected operational flexibility and investment economics.

Section 10 concluded the review with providing scale-up data, with a preliminary view into the prospects and the overall economy of the system and with recommendations for additional research. In particular, a LCOE analysis is presented for a peaker CSP plant that identifies the critical elements governing the cost of a commercial scale fluidized particle solar power plant by comparison with molten salt technology. For the fluidized-particle CSP a multi-tower concept sharing the same power block (with an innovative combined cycle) is selected. The particle technology has a much cheaper storage cost than molten salt technology but is handicapped by the cost of particle handling (CAPEX and OPEX). This drawback is reduced by a sH₂O cycle that twice reduces the particle mass flow rate and consequently, the conveying cost. All the cost were estimated. The sum of the above-mentioned costs respective to the medium-scale particle plant's subsystems is US\$ 75M. For the large-scale particle plant it is US\$ 343.4M. Adding the indirect EPC costs (engineering, management, contingencies, etc.) and the owner's costs (land, infrastructure, etc.), the Capex of each turnkey plant is US\$ 90M (medium scale) and US\$ 412.1M (large scale). That corresponds to US\$ 3560/kW_e and US\$ 2750/kW_e, respectively.

The O&M costs of the particle plants studied are US\$ 14.64/MWh (medium scale) and US\$ 16.56/MWh (large scale). For a benchmark molten salt tower, they would be reduced to US\$ 12.5/MWh. Through adding O&M costs and CAPEX amortization, the estimated LCOE of the peaker plant concepts is calculated at US\$ 178.24/MWh (medium scale), or US\$ 143/MWh (large scale). In comparison, it will be approximately US\$ 141.8/MWh for the benchmark large-scale molten salt tower.

CRediT authorship contribution statement

Gilles Flamant: Investigation, Data curation, Visualization, Writing – original draft, Writing – review & editing, Validation, Supervision, Project administration, Methodology, Funding acquisition. **Benjamin Grange:** Methodology, Data curation, Writing – original draft, Project administration. **John Wheeldon:** Methodology, Data curation, Writing – original draft, Project administration. **Frédéric Siros:** Methodology, Data curation, Writing – original draft, Project administration. **Benoit Valentin:** Data curation, Visualization, Writing – original draft, Writing – review & editing. **Françoise Bataille:** Data curation, Visualization, Writing – original draft, Writing – review & editing. **Huili Zhang:** Data curation, Visualization, Writing – original draft, Writing – review & editing. **Yimin Deng:** Investigation, Data curation, Visualization, Writing – original draft, Writing – review & editing, Validation, Supervision, Project administration. **Jan Baeyens:** Investigation, Data curation, Visualization, Writing – original draft, Writing – review & editing, Validation, Supervision, Project administration.

Declaration of competing interest

The authors declare that they have no known competing financial interests or personal relationships that could have appeared to influence the work reported in this paper.

Data availability

No data was used for the research described in the article.

Acknowledgements

This work has received funding from the European Union's Horizon 2020 research and innovation program under grant agreement No 727762, Next-CSP project. It was moreover supported by the French "Investments for the future" ("Investissements d'Avenir") program managed by the National Agency for Research (ANR) under contract ANR-10-LABX-22-01 (labex SOLSTICE) and ANR-10-EQPX-49-SOCRATE.

Supplementary materials

Supplementary material associated with this article can be found, in the online version, at doi:[10.1016/j.peccs.2022.101056](https://doi.org/10.1016/j.peccs.2022.101056).

References

- [1] IEA. Renewables 2021. Analysis and forecast to 2026. 2021.
- [2] IRENA. Renewable capacity statistics 2020. 2021.
- [3] SolarPACES. Potential for Solar Thermal Energy By Country 2008. <https://www.solarpaces.org/csp-technologies/csp-potential-solar-thermal-energy-by-member-nation/>.
- [4] ESTELA. The value of thermal storage 2016. <https://www.estelasolar.org/>.
- [5] Jorgenson J, Denholm P, Mehos M. Estimating the Value of utility-scale solar technologies in California under a 40% renewable portfolio standard. 2014.
- [6] Price H, Kearney D, Redell F, Charles R, Morse F. Dispatchable solar power plant. 2018, 040032. <https://doi.org/10.1063/1.5067068>.
- [7] Lovegrove K, James G, Leitch D, Ngo A, Milczarek A, Rutovitz J, et al. Comparison of dispatchable renewable electricity options. 2018.
- [8] Feldman D, Margolis R, Denholm P. Exploring the potential competitiveness of utility-scale photovoltaics plus batteries with concentrating solar power, 2015–2030. 2016.
- [9] Pamponet MC, Maranduba HL, Almeida Neto JA, Rodrigues LB. Energy balance and carbon footprint of very large-scale photovoltaic power plant. Int J Energy Res 2022;46:6901–18. <https://doi.org/10.1002/er.7529>.
- [10] Ahmad Ludin N, Ahmad Affandi NA, Purvis-Roberts K, Ahmad A, Ibrahim MA, Sopian K, et al. Environmental impact and levelised cost of energy analysis of solar photovoltaic systems in selected asia pacific region: a cradle-to-grave approach. Sustainability 2021;13:396. <https://doi.org/10.3390/su13010396>.
- [11] Carvalho ML, Temporelli A, Girardi P. Life cycle assessment of stationary storage systems within the italian electric network. Energies 2021;14:2047. <https://doi.org/10.3390/en14082047>.
- [12] Porzio J, Scown CD. Life-cycle assessment considerations for batteries and battery materials. Adv Energy Mater 2021;11:2100771. <https://doi.org/10.1002/aenm.202100771>.
- [13] IRENA. Renewable power generation costs in 2019. 2019.
- [14] Lilliestam J, Pitz-Paal R. Concentrating solar power for less than USD 0.07 per kWh: finally the breakthrough? Renew Energy Focus 2018;26:17–21. <https://doi.org/10.1016/j.ref.2018.06.002>.
- [15] Hack H. Small-scale flexible advanced ultra-supercritical coal-fired power plant with integrated carbon capture. 2020.
- [16] Iverson BD, Conboy TM, Pasch JJ, Krutzenga AM. Supercritical CO2 Brayton cycles for solar-thermal energy. Appl Energy 2013;111:957–70. <https://doi.org/10.1016/j.apenergy.2013.06.020>.
- [17] Valentin B, Siros F, Brau J-F. Optimization of a decoupled combined cycle gas turbine integrated in a particle receiver solar power plant. 2019, 140007. <https://doi.org/10.1063/1.5117655>.
- [18] Mehos M, Turchi C, Vidal J, Wagner M, Ma Z, Ho C, et al. Concentrating solar power – Gen3 demonstration roadmap. 2017.
- [19] Benoit H, Spreafico L, Gauthier D, Flamant G. Review of heat transfer fluids in tube-receivers used in concentrating solar thermal systems: Properties and heat transfer coefficients. Renew Sustain Energy Rev 2016;55:298–315. <https://doi.org/10.1016/j.rser.2015.10.059>.
- [20] Torresol Energy. Gemasolar 2015. <http://www.torresolenergy.com/TORRESOL/gemasolar-plant/en>.
- [21] Ivanpah Solar Electric Generating Station 2015.
- [22] International Energy Agency. Renewables 2020. OECD. 2020. <https://doi.org/10.1787/c74616c1-en>.
- [23] Zhang HL, Baeyens J, Degreve J, Caçeres G. Concentrated solar power plants: Review and design methodology. Renew Sustain Energy Rev 2013;22:466–81. <https://doi.org/10.1016/j.rser.2013.01.032>.
- [24] solarpaces n.d. www.solarpaces.org.
- [25] NREL. Dhursar CSP Project. Inst Adv Sustain Stud Others 2021. <https://solarpaces.nrel.gov/project/dhursar>.
- [26] Zhang HL, Baeyens J, Degreve J. The potential of a hybrid power plant for the Dubrovnik - Neretva County (Southern Croatia). J Sustain Dev Energy Water Environ Syst 2015;3:174–82. <https://doi.org/10.13044/j.sdewes.2015.03.0014>.
- [27] Zhang HL, Degreve J, Baeyens J, Lv YQ. Biomass as back-up fuel in hybrid solar power plants. In: 2nd Sino-German Symp Biobased Chem Biorefinery; 2015.
- [28] Flamant G. Theoretical and experimental study of radiant heat transfer in a solar fluidized-bed receiver. AIChE J 1982;28:529–35. <https://doi.org/10.1002/aic.690280402>.
- [29] Mahmoudi S, Chan CW, Brems A, Seville J, Baeyens J. Solids flow diagram of a CFB riser using Geldart B-type powders. Particuology 2012;10:51–61. <https://doi.org/10.1016/j.partic.2011.09.002>.
- [30] Van de Velden M, Baeyens J, Seville JPK, Fan X. The solids flow in the riser of a Circulating Fluidised Bed (CFB) viewed by Positron Emission Particle Tracking (PEPT). Powder Technol 2008;183:290–6. <https://doi.org/10.1016/j.powtec.2007.07.027>.
- [31] Rafique MM, Nathan G, Saw W. A mathematical model to assess the influence of transients on a refractory-lined solar receiver. Renew Energy 2021;167:217–35. <https://doi.org/10.1016/j.renene.2020.11.077>.
- [32] Rafique MM. Start-up time and thermal losses of a particle solar receiver under transient operating conditions. 2022, 110009. <https://doi.org/10.1063/5.0086798>.
- [33] Dunham MT, Iverson BD. High-efficiency thermodynamic power cycles for concentrated solar power systems. Renew Sustain Energy Rev 2014;30:758–70. <https://doi.org/10.1016/j.rser.2013.11.010>.
- [34] Cziesla F, Kremer H, Much U, Riemschneider J-E, Quinkertz R. Advanced 800+ MW steam power plants and future CCS options. Siemens Ind Turbomach 2009: 1–21.
- [35] Siemens. Steam turbines for CSP plants. 2010. Erlangen, Germany.
- [36] Romero M, González-Aguilar J. Solar thermal CSP technology. Wiley Interdiscip Rev Energy Environ 2014;3:42–59. <https://doi.org/10.1002/wene.79>.
- [37] Spelling J, Gallo A, Romero M, González-Aguilar J. A high efficiency solar thermal power plant using a dense particle suspension as heat transfer fluid. In: Int Conf Conc Sol Power Chem Energy Syst; 2014.
- [38] Reyes-Belmonte MA, Sebastián A, González-Aguilar J, Romero M. Performance comparison of different thermodynamic cycles for an innovative central receiver solar power plant. 2017, 160024. <https://doi.org/10.1063/1.4984558>.
- [39] Singer C, Buck R, Pitz-Paal R, Müller-Steinhagen H. Assessment of solar power tower driven ultrasupercritical steam cycles applying tubular central receivers with varied heat transfer media. J Sol Energy Eng 2010;132:041010. <https://doi.org/10.1115/1.4002137>.
- [40] Caposio JP, Fabani MP, Reyes-Urrutia A, Torres-Sciancalepore R, Deng Y, Baeyens J, et al. Sustainable solar drying of Brewer's spent grains: a comparison with conventional electric convective drying. Processes 2022;10:339. <https://doi.org/10.3390/pr10020339>.
- [41] Deng Y, Webin K, Zhang H, Dewil R, Baeyens J. Solar tower continuous saturated steam generation. 2022. p. 3–13. https://doi.org/10.1007/978-981-19-4360-7_1.
- [42] Zhang H, Baeyens J, Dewil R, Li S, Deng Y, Reyes-Urrutia A, et al. Solar biomass pyrolysis with latent heat ballast. In: 2021 5th Int Conf Power Energy Eng. IEEE; 2021. p. 85–90. <https://doi.org/10.1109/ICPEES4380.2021.9662469>.
- [43] Baeyens J, Zhang H, Kong W, Dumont P, Flamant G. Solar thermal treatment of non-metallic minerals: the potential application of the SOLPART technology. AIP Conf Proc 2019:180002. <https://doi.org/10.1063/1.5117682>.
- [44] Deng Y, Liu J, Li S, Dewil R, Zhang H, Baeyens J, et al. The steam-assisted calcination of limestone and dolomite for energy savings and to foster solar calcination processes. J Clean Prod 2022;132640. <https://doi.org/10.1016/j.jclepro.2022.132640>.
- [45] Volume WH. Shape, and roundness of quartz particles. J Geol 1935;43:250–80. <https://doi.org/10.1086/624298>.
- [46] Geldart D. Single particles, fixed and quiescent beds. Gas Fluid Technol 1986: 11–32.
- [47] Kong W, Tan T, Baeyens J, Flamant G, Zhang H. Bubbling and slugging of Geldart Group A powders in small diameter columns. Ind Eng Chem Res 2017;56: 4136–44. <https://doi.org/10.1021/acs.iecr.6b04798>.
- [48] Ergun S. Fluid flow through packed columns. Chem Eng Prog 1952. citeulike-article-id:7797897.
- [49] Akgiray Ö, Saatçı AM. A new look at filter backwash hydraulics. Water Sci Technol Water Supply 2001;1:65–72.
- [50] Geldart D. Types of gas fluidization. Powder Technol 1973;7:285–92. [https://doi.org/10.1016/0032-5910\(73\)80037-3](https://doi.org/10.1016/0032-5910(73)80037-3).
- [51] Baeyens J, Geldart D. Predictive calculations of flow parameters in gas fluidized beds and fluidization behaviour of various powders. In: Cepadues, editor. Proceeding Int. Symp. Fluid. its Appl., Toulouse, France; 1974. p. 263–73.
- [52] Wu SY, Baeyens J. Effect of operating temperature on minimum fluidization velocity. Powder Technol 1991;67:217–20. [https://doi.org/10.1016/0032-5910\(91\)80158-F](https://doi.org/10.1016/0032-5910(91)80158-F).
- [53] Rabinovich E, Kalman H. Flow regime diagram for vertical pneumatic conveying and fluidized bed systems. Powder Technol 2011;207:119–33. <https://doi.org/10.1016/j.powtec.2010.10.017>.
- [54] Avidan AA, Yerushalmi J. Bed expansion in high velocity fluidization. Powder Technol 1982;32:223–32. [https://doi.org/10.1016/0032-5910\(82\)85024-9](https://doi.org/10.1016/0032-5910(82)85024-9).
- [55] Yerushalmi J, Cankurt NT. Further studies of the regimes of fluidization. Powder Technol 1979;24:187–205. [https://doi.org/10.1016/0032-5910\(79\)87036-9](https://doi.org/10.1016/0032-5910(79)87036-9).
- [56] Baeyens J, Geldart D. An investigation into slugging fluidized beds. Chem Eng Sci 1974;29:255–65. [https://doi.org/10.1016/0009-2509\(74\)85051-7](https://doi.org/10.1016/0009-2509(74)85051-7).
- [57] Abrahamsen AR, Geldart D. Behaviour of gas-fluidized beds of fine powders Part I. Homogeneous expansion. Powder Technol 1980;26:35–46. [https://doi.org/10.1016/0032-5910\(80\)85005-4](https://doi.org/10.1016/0032-5910(80)85005-4).
- [58] Deng Y, Sabatier F, Dewil R, Flamant G, Le Gal A, Gueguen R, et al. Dense upflow fluidized bed (DUF) solar receivers of high aspect ratio: different fluidization modes through inserting bubble rupture promoters. Chem Eng J 2021;418: 129376. <https://doi.org/10.1016/j.cej.2021.129376>.

- [59] Zhang H, Degrève J, Baeyens J, Dewil R. The voidage in a CFB riser as function of solids flux and gas velocity. *Procedia Eng* 2015;102:1112–22. <https://doi.org/10.1016/j.proeng.2015.01.234>.
- [60] Yagi S, Muchi I, Aochi T. On the conditions of fluidization of bed. *Chem Mach* 1952;16:307–12.
- [61] Gutfinger C, Abuaf N. *Advances in heat transfer* Volume 10. Elsevier; 1974. [https://doi.org/10.1016/S0065-2717\(08\)70111-4](https://doi.org/10.1016/S0065-2717(08)70111-4).
- [62] Botterill JSM. *Fluid bed heat transfer*. New York: Academic Press; 1975.
- [63] Saxena SC, Grewal NS, Gabor JD, Zabrodsky SS, Galershtein DM. Heat transfer between a gas fluidized bed and immersed tubes. *Adv Heat Transf* 1978;14: 149–247.
- [64] Grace JR. Fluidization. In: Hetsroni G, editor. *Handb Multiph Syst*. New York: Hemisphere Pub. Corp.; 1982.
- [65] Baeyens J, Geldart D. Modelling approach to the effect of equipment scale on fluidised bed heat transfer data. *J Powder Bulk Solids Technol* 1980;4:1.
- [66] Xavier AM, Davidson JF. Heat transfer in fluidized beds: Convective heat transfer in fluidized beds. In: Davidson JF, Clift R, Harrison D, editors. *Fluidization*. 2nd ed. Academic Press; 1984. p. 437.
- [67] Mazza GD, Bressa SP, Barreto GF. On the validity of the addition of independent contributions for evaluating heat transfer rates in gas fluidized beds. *Powder Technol* 1997;90:1–11. [https://doi.org/10.1016/S0032-5910\(96\)03189-0](https://doi.org/10.1016/S0032-5910(96)03189-0).
- [68] Denloye AOO, Botterill JSM. Bed to surface heat transfer in a fluidized bed of large particles. *Powder Technol* 1978;19:197–203. [https://doi.org/10.1016/0032-5910\(78\)80028-X](https://doi.org/10.1016/0032-5910(78)80028-X).
- [69] Xavier AM, Davidson JF. Heat transfer to surfaces immersed in fluidised beds, particularly tube arrays. In: Davidson JF, Keairns DL, editors. *Fluid Proceeding Second Eng Found Conf*. Cambridge, England: Cambridge University Press; 1978. p. 333–8.
- [70] Baskakov AP, Vitt OK, Kirakosyan VA, Maskayev VK, Filipovsky NF. Investigation of heat transfer coefficient pulsations and of the mechanism of heat transfer from a surface immersed into a fluidized bed. 1974. p. 293–302.
- [71] Flamant G, Lu JD, Variot B. Towards a generalized model for vertical walls to gas—solid fluidized beds heat transfer—II. Radiative transfer and temperature effects. *Chem Eng Sci* 1993;48:2493–503. [https://doi.org/10.1016/0009-2509\(93\)81070-C](https://doi.org/10.1016/0009-2509(93)81070-C).
- [72] Zabrodsky SS, Antonishin NV, Parnas AL. On fluidized bed-to-surface heat transfer. *Can J Chem Eng* 1976;54:52–8. <https://doi.org/10.1002/cjce.5450540107>.
- [73] H WR, T WJ. Bubble behavior around immersed tubes in a fluidized bed. *AIChE Symp Ser* 1973;69:68–77.
- [74] Genetti WE, Schmall RA, Grimmett ES. The effect of tube orientation on heat transfer with bare and finned tubes in a fluidized bed. *Chem Eng Progr Symp Ser* 1971;67:90.
- [75] Bartel WJ, Genetti WE. Heat transfer from a horizontal bundle of bare and finned tubes in an air fluidized bed. *AIChE Symp Ser* 1973;69:85–93.
- [76] Priebe SJ, Genetti WE. Heat transfer from a horizontal bundle of extended surface tubes to an air fluidized bed. *AIChE Symp Ser* 1977;161:38.
- [77] Staub PW, Canada GS. Effect of tube bank and gas density on flow behavior and heat transfer in fluidized beds. In: Davidson JF, Keairns DL, editors. *Fluid Proceeding Second Eng Found Conf*; 1978. p. 339–43.
- [78] Zabrodsky SS, Tamarin AF, Dolidovich GI, Epanov YG. Heat Transfer of Single horizontal finned tubes and their bundles in a fluidized bed of large particles. In: Grace JR, Matsen JM, editors. *Fluidization*; 1980. p. 195–200.
- [79] Bartel WH, Genetti WE, Grimmett ES. Heat transfer from a horizontal discontinuous finned tube in a fluidized bed. *Chem Eng Progr Symp Ser* 1971;116: 85–9.
- [80] Zhang H, Benoit H, Gauthier D, Degrève J, Baeyens J, López IP, et al. Particle circulation loops in solar energy capture and storage: gas–solid flow and heat transfer considerations. *Appl Energy* 2016;161:206–24. <https://doi.org/10.1016/j.apenergy.2015.10.005>.
- [81] Berg Clyde HO. Conveyance of granular solids. 1954. Patent US2684867.
- [82] Aoki R, Tsunakawa H, Nishizawa T, Koizumi M. High density and low velocity pneumatic transportation of powders and granular materials. *J Res Assoc Powder Technol Japan* 1973;10:616–21. <https://doi.org/10.4164/sptj1964.10.616>.
- [83] Li H, Kwauk M. Vertical pneumatic moving-bed transport—II. Experimental findings. *Chem Eng Sci* 1989;44:261–71. [https://doi.org/10.1016/0009-2509\(89\)85063-8](https://doi.org/10.1016/0009-2509(89)85063-8).
- [84] Hiramata T, Takeuchi H, Chiba T. Regime classification of macroscopic gas—solid flow in a circulating fluidized bed riser. *Powder Technol* 1992;70:215–22. [https://doi.org/10.1016/0032-5910\(92\)80056-3](https://doi.org/10.1016/0032-5910(92)80056-3).
- [85] Zhu H, Zhu J. Gas-solids flow structures in a novel circulating-turbulent fluidized bed. *AIChE J* 2008;54:1213–23. <https://doi.org/10.1002/aic.11432>.
- [86] Watson RJ, Thorpe RB, Davidson JF. Vertical plug-flow pneumatic conveying from a fluidised bed. *Powder Technol* 2012;224:155–61. <https://doi.org/10.1016/j.powtec.2012.02.045>.
- [87] Flamant G, Gauthier D, Benoit H, Sans J-L, Garcia R, Boissière B, et al. Dense suspension of solid particles as a new heat transfer fluid for concentrated solar thermal plants: On-sun proof of concept. *Chem Eng Sci* 2013;102:567–76. <https://doi.org/10.1016/j.ces.2013.08.051>.
- [88] Turzo G. *Transport par fluidisation en phase hyperdense : amélioration technologique, modélisation et dimensionnement*. 2013. Toulouse, INPT.
- [89] Boissière B, Ansart R, Gauthier D, Flamant G, Hemati M. Experimental hydrodynamic study of gas-particle dense suspension upward flow for application as new heat transfer and storage fluid. *Can J Chem Eng* 2015;93:317–30. <https://doi.org/10.1002/cjce.22087>.
- [90] Tomita Y, Yutani S, Jotaki T. Pressure drop in vertical pneumatic transport lines of powdery material at high solids loading. *Powder Technol* 1980;25:101–7. [https://doi.org/10.1016/0032-5910\(80\)87015-X](https://doi.org/10.1016/0032-5910(80)87015-X).
- [91] Flamant G, Hemati M. Dispositif collecteur d'énergie solaire. 2010. French Patent No.1058565.
- [92] Pitié F, Zhao CY, Baeyens J, Degrève J, Zhang HL. Circulating fluidized bed heat recovery/storage and its potential to use coated phase-change-material (PCM) particles. *Appl Energy* 2013;109:505–13. <https://doi.org/10.1016/j.apenergy.2012.12.048>.
- [93] Zhang HL, Baeyens J, Degrève J, Brems A, Dewil R. The convection heat transfer coefficient in a Circulating Fluidized Bed (CFB). *Adv Powder Technol* 2014;25: 710–5. <https://doi.org/10.1016/j.apt.2013.10.018>.
- [94] Kodama T, Bellan S, Gokon N, Cho HS. Particle reactors for solar thermochemical processes. *Sol Energy* 2017;156:113–32. <https://doi.org/10.1016/j.solener.2017.05.084>.
- [95] Liu J, Baeyens J, Deng Y, Wang X, Zhang H. High temperature Mn₂O₃/Mn₃O₄ and Co₃O₄/CoO systems for thermo-chemical energy storage. *J Environ Manage* 2020;267:110582. <https://doi.org/10.1016/j.jenvman.2020.110582>.
- [96] Deng Y, Dewil R, Appels L, Li S, Baeyens J, Degrève J, et al. Thermo-chemical water splitting: selection of priority reversible redox reactions by multi-attribute decision making. *Renew Energy* 2021;170:800–10. <https://doi.org/10.1016/j.renene.2021.02.009>.
- [97] Alonso E, Romero M. Review of experimental investigation on directly irradiated particles solar reactors. *Renew Sustain Energy Rev* 2015;41:53–67. <https://doi.org/10.1016/j.rser.2014.08.027>.
- [98] Flamant G, Hernandez D, Bonet C, Traverse J-P. Experimental aspects of the thermochemical conversion of solar energy: Decarbonation of CaCO₃. *Sol Energy* 1980;24:385–95. [https://doi.org/10.1016/0038-092X\(80\)90301-1](https://doi.org/10.1016/0038-092X(80)90301-1).
- [99] Tregambi C, Chirone R, Montagnaro F, Salatino P, Solimene R. Heat transfer in directly irradiated fluidized beds. *Sol Energy* 2016;129:85–100. <https://doi.org/10.1016/j.solener.2016.01.057>.
- [100] Migliozzi S, Paulillo A, Chirone R, Salatino P, Solimene R. Hydrodynamics of compartmented fluidized beds under uneven fluidization conditions. *Powder Technol* 2017;316:476–91. <https://doi.org/10.1016/j.powtec.2016.12.052>.
- [101] Solimene R, Chirone R, Chirone R, Salatino P. Dynamic modeling of a solar receiver/thermal energy storage system based on a compartmented dense gas fluidized bed. 2017, 080026. <https://doi.org/10.1063/1.4984447>.
- [102] Tregambi C, Salatino P, Solimene R, Montagnaro F. An experimental characterization of Calcium Looping integrated with concentrated solar power. *Chem Eng J* 2018;331:794–802. <https://doi.org/10.1016/j.cej.2017.08.068>.
- [103] Tregambi C, Bevilacqua C, Troiano M, Solimene R, Salatino P. A novel autothermal fluidized bed reactor for concentrated solar thermal applications. *Chem Eng J* 2020;398:125702. <https://doi.org/10.1016/j.cej.2020.125702>.
- [104] STEM®. Thermal energy storage. Magaldi. 2020. <https://www.magaldi.com/en/expertise/solar-energy>.
- [105] Kodama T, Enomoto S, Hatamachi T, Gokon N. Application of an internally circulating fluidized bed for windowed solar chemical reactor with direct irradiation of reacting particles. *J Sol Energy Eng* 2008;130. <https://doi.org/10.1115/1.2807213>.
- [106] Gokon N, Takahashi S, Yamamoto H, Kodama T. Thermochemical two-step water-splitting reactor with internally circulating fluidized bed for thermal reduction of ferrite particles. *Int J Hydrogen Energy* 2008;33:2189–99. <https://doi.org/10.1016/j.ijhydene.2008.02.044>.
- [107] Gokon N, Ono R, Hatamachi T, Liuyun L, Kim H-J, Kodama T. CO₂ gasification of coal cokes using internally circulating fluidized bed reactor by concentrated Xe-light irradiation for solar gasification. *Int J Hydrogen Energy* 2012;37:12128–37. <https://doi.org/10.1016/j.ijhydene.2012.05.133>.
- [108] Bellan S, Kodama T, Matsubara K, Gokon N, Cho HS, Inoue K. Heat transfer and particulate flow analysis of a 30kW directly irradiated solar fluidized bed reactor for thermochemical cycling. *Chem Eng Sci* 2019;203:511–25. <https://doi.org/10.1016/j.ces.2018.09.012>.
- [109] Kodama T, Gokon N, Cho HS, Matsubara K, Kaneko H, Senuma K, et al. Particles fluidized bed receiver/reactor tests with quartz sand particles using a 100-kWth beam-down solar concentrating system at Miyazaki. 2017, 100012. <https://doi.org/10.1063/1.4984469>.
- [110] Boujjat H, Rodat S, Chuayboon S, Abanades S. Experimental and numerical study of a directly irradiated hybrid solar/combustion spouted bed reactor for continuous steam gasification of biomass. *Energy* 2019;189:116118. <https://doi.org/10.1016/j.energy.2019.116118>.
- [111] Zraggen A, Haueter P, Maag G, Vidal A, Romero M, Steinfeld A. Hydrogen production by steam-gasification of petroleum coke using concentrated solar power—III. Reactor experimentation with slurry feeding. *Int J Hydrogen Energy* 2007;32:992–6. <https://doi.org/10.1016/j.ijhydene.2006.10.001>.
- [112] Ermanoski I. Cascading pressure thermal reduction for efficient solar fuel production. *Int J Hydrogen Energy* 2014;39:13114–7. <https://doi.org/10.1016/j.ijhydene.2014.06.143>.
- [113] Moumin G, Tescari S, Sundarraj P, de Oliveira L, Roeb M, Sattler C. Solar treatment of cohesive particles in a directly irradiated rotary kiln. *Sol Energy* 2019;182:480–90. <https://doi.org/10.1016/j.solener.2019.01.093>.
- [114] Melchior T, Perkins C, Lichty P, Weimer AW, Steinfeld A. Solar-driven biochar gasification in a particle-flow reactor. *Chem Eng Process Intensif* 2009;48: 1279–87. <https://doi.org/10.1016/j.cep.2009.05.006>.
- [115] Müller F, Pozivil P, van Eyk PJ, Villarazo A, Haueter P, Wieckert C, et al. A pressurized high-flux solar reactor for the efficient thermochemical gasification of carbonaceous feedstock. *Fuel* 2017;193:432–43. <https://doi.org/10.1016/j.fuel.2016.12.036>.

- [116] Meier A, Bonaldi E, Cella GM, Lipinski W, Wullemain D. Solar chemical reactor technology for industrial production of lime. *Sol Energy* 2006;80:1355–62. <https://doi.org/10.1016/j.solener.2005.05.017>.
- [117] Esence T, Guillot E, Tessonnaud M, Sans J-L, Flamant G. Solar calcination at pilot scale in a continuous flow multistage horizontal fluidized bed. *Sol Energy* 2020; 207:367–78. <https://doi.org/10.1016/j.solener.2020.06.098>.
- [118] Abdelrahman M, Fumeaux P, Suter P. Study of solid-gas-suspensions used for direct absorption of concentrated solar radiation. *Sol Energy* 1979;22:45–8. [https://doi.org/10.1016/0038-092X\(79\)90058-6](https://doi.org/10.1016/0038-092X(79)90058-6).
- [119] Miller F, Koenigsdorff R. Theoretical analysis of a high-temperature small-particle solar receiver. *Sol Energy Mater* 1991;24:210–21. [https://doi.org/10.1016/0165-1633\(91\)90061-0](https://doi.org/10.1016/0165-1633(91)90061-0).
- [120] Bertocchi R, Karni J, Kribus A. Experimental evaluation of a non-isothermal high temperature solar particle receiver. *Energy* 2004;29:687–700. <https://doi.org/10.1016/j.energy.2003.07.001>.
- [121] Fernández P, Müller F. Assessment of the overall efficiency of gas turbine-driven CSP plants using small particle solar receivers. *Energy Procedia* 2014;49:334–43. <https://doi.org/10.1016/j.egypro.2014.03.036>.
- [122] Xiao G, Guo K, Luo Z, Ni M, Zhang Y, Wang C. Simulation and experimental study on a spiral solid particle solar receiver. *Appl Energy* 2014;113:178–88. <https://doi.org/10.1016/j.apenergy.2013.06.045>.
- [123] Xiao G, Guo K, Ni M, Luo Z, Cen K. Optical and thermal performance of a high-temperature spiral solar particle receiver. *Sol Energy* 2014;109:200–13. <https://doi.org/10.1016/j.solener.2014.08.037>.
- [124] Xie X, Xiao G, Ni M, Yan J, Dong H, Cen K. Optical and thermal performance of a novel solar particle receiver. 2019, 030065. <https://doi.org/10.1063/1.5117577>.
- [125] Wang T, Bai F, Chu S, Zhang X, Wang Z. Experiment study of a quartz tube falling particle receiver. *Front Energy* 2017;11:472–9. <https://doi.org/10.1007/s11708-017-0502-6>.
- [126] Nie F, Bai F, Cui Z, Zhao Z, Wang Z. Cold-state experimental study on discharge characteristics of solid particles in a single-tube gravity driven moving bed solar receiver. 2020, 050003. <https://doi.org/10.1063/5.0028506>.
- [127] Nie F, Yu Y, Bai F, Wang Z. Experimental and numerical investigation on thermal performance of a quartz tube solid particle solar receiver. *Sol Energy* 2020;207: 1055–69. <https://doi.org/10.1016/j.solener.2020.07.013>.
- [128] Nie F, Bai F, Wang Z, Yang R. A CPFD simulation on the particle flow characteristics in a packed moving bed solar receiver with an added insert. *Sol Energy* 2021;224:1144–59. <https://doi.org/10.1016/j.solener.2021.06.078>.
- [129] Flamant G. Thermochimie solaire à hautes températures, résultats expérimentaux. Quelques perspectives d'application. *Rev Phys Appliquée* 1980;15:503–11. <https://doi.org/10.1051/rphysap:01980001503050300>.
- [130] Ho CK. A review of high-temperature particle receivers for concentrating solar power. *Appl Therm Eng* 2016;109:958–69. <https://doi.org/10.1016/j.applthermaleng.2016.04.103>.
- [131] Martin J, Jr V. ASCUAS: a solar central receiver utilizing a solid thermal carrier. 1982. <https://doi.org/10.2172/5663779>. Albuquerque, NM, and Livermore, CA (United States).
- [132] Hruby J, Steeper R, Evans G, Crowe C. An Experimental and numerical study of flow and convective heat transfer in a freely falling curtain of particles. 1986. <https://doi.org/10.2172/1616232>. Albuquerque, NM, and Livermore, CA (United States).
- [133] Hruby JM. Technical feasibility study of a solid particle solar central receiver for high temperature applications. 1986. United States.
- [134] Christian J, Ho C. Alternative designs of a high efficiency, north-facing, solid particle receiver. *Energy Procedia* 2014;49:314–23. <https://doi.org/10.1016/j.egypro.2014.03.034>.
- [135] Mills B, Ho CK. Annualized thermal performance of intermediate-scale falling particle receivers. 2018, 040026. <https://doi.org/10.1063/1.5067062>.
- [136] Ho CK, Christian JM, Romano D, Yellowhair J, Siegel N, Savoldi L, et al. Characterization of particle flow in a free-falling solar particle receiver. *J Sol Energy Eng* 2017;139. <https://doi.org/10.1115/1.4035258>.
- [137] Kim K, Moujaes SF, Kolb GJ. Experimental and simulation study on wind affecting particle flow in a solar receiver. *Sol Energy* 2010;84:263–70. <https://doi.org/10.1016/j.solener.2009.11.005>.
- [138] Siegel NP, Ho CK, Khalsa SS, Kolb GJ. Development and evaluation of a prototype solid particle receiver: on-sun testing and model validation. *J Sol Energy Eng* 2010;132. <https://doi.org/10.1115/1.4001146>.
- [139] Ho CK, Christian JM, Yellowhair J, Armijo K, Kolb WJ, Jeter S, et al. Performance evaluation of a high-temperature falling particle receiver. In: Vol 1 Biofuels, Hydrog Syngas, Altern Fuels; CHP Hybrid Power Energy Syst Conc Sol Power; Energy Storage; Environ Econ Policy Considerations Adv Energy Syst Geothermal, Ocean Emerg E. American Society of Mechanical Engineers; 2016. <https://doi.org/10.1115/ES2016-59238>.
- [140] Ho CK, Peacock G, Christian JM, Albrecht K, Yellowhair JE, Ray D. On-sun testing of a 1 MWt particle receiver with automated particle mass-flow and temperature control. 2019, 030027. <https://doi.org/10.1063/1.5117539>.
- [141] Wu W, Amsbeck L, Buck R, Uhlrig R, Ritz-Paal R. Proof of concept test of a centrifugal particle receiver. *Energy Procedia* 2014;49:560–8. <https://doi.org/10.1016/j.egypro.2014.03.060>.
- [142] Wu W, Trebing D, Amsbeck L, Buck R, Pitz-Paal R. Prototype testing of a centrifugal particle receiver for high-temperature concentrating solar applications. *J Sol Energy Eng* 2015;137. <https://doi.org/10.1115/1.4030657>.
- [143] Amsbeck L, Buck R, Ebert M, Gobreit B, Hertel J, Jensch A, et al. First tests of a centrifugal particle receiver with a 1m2 aperture. 2018, 040004. <https://doi.org/10.1063/1.5067040>.
- [144] Ebert M, Amsbeck L, Rheinländer J, Schlögl-Knothe B, Schmitz S, Sibum M, et al. Operational experience of a centrifugal particle receiver prototype. 2019, 030018. <https://doi.org/10.1063/1.5117530>.
- [145] Flamant G, Hemati M. Dispositif collecteur d'énergie solaire (Device for collecting solar energy). PCT extension WO/2012/052661. 2010.
- [146] Benoit H, Ansart R, García-Triñanes P, Gauthier D, Flamant G, Simonin O. 3D numerical simulation of upflow bubbling fluidized bed in opaque tube under high flux solar heating. In: 9th Int Conf Multiph Flow (ICMF 2016); 2016. p. 1–6.
- [147] Flamant G, Gauthier D, Benoit H, Sans J-L, Boissière B, Ansart R, et al. A new heat transfer fluid for concentrating solar systems: particle flow in tubes. *Energy Procedia* 2014;49:617–26. <https://doi.org/10.1016/j.egypro.2014.03.067>.
- [148] Benoit H, Pérez López I, Gauthier D, Sans J-L, Flamant G. On-sun demonstration of a 750°C heat transfer fluid for concentrating solar systems: dense particle suspension in tube. *Sol Energy* 2015;118:622–33. <https://doi.org/10.1016/j.solener.2015.06.007>.
- [149] Le Gal A, Grange B, Tessonnaud M, Perez A, Escape C, Sans J-L, et al. Thermal analysis of fluidized particle flows in a finned tube solar receiver. *Sol Energy* 2019;191:19–33. <https://doi.org/10.1016/j.solener.2019.08.062>.
- [150] López IP, Benoit H, Gauthier D, Sans J-L, Guillot E, Cavaillé R, et al. On-sun first operation of a 150 kWth pilot solar receiver using dense particle suspension as heat transfer fluid. 2016, 030028. <https://doi.org/10.1063/1.4949080>.
- [151] H2020 Next-CSP project n.d.
- [152] Zhang H, Li S, Kong W, Flamant G, Baeyens J. Scale-up considerations of the UBFB solar receiver. In: AIP Conf Proc; 2019, 030067. <https://doi.org/10.1063/1.5117579>.
- [153] Zhang H, Benoit H, Perez-Lopez I, Flamant G, Tan T, Baeyens J. High-efficiency solar power towers using particle suspensions as heat carrier in the receiver and in the thermal energy storage. *Renew Energy* 2017;111:438–46. <https://doi.org/10.1016/j.renene.2017.03.101>.
- [154] Perez Lopez I, Benoit H, Gauthier D, Sans JL, Guillot E, Mazza G, et al. On-sun operation of a 150kW th pilot solar receiver using dense particle suspension as heat transfer fluid. *Sol Energy* 2016;137:463–76. <https://doi.org/10.1016/j.solener.2016.08.034>.
- [155] Kang Q, Flamant G, Dewil R, Baeyens J, Zhang HL, Deng YM. Particles in a circulation loop for solar energy capture and storage. *Particuology* 2019;43: 149–56. <https://doi.org/10.1016/j.partic.2018.01.009>.
- [156] MHC Engineering Fordertechnik GmbH. Chain Conveyors. n.d.
- [157] GmbH H & E. HAZEMAG Minerals: chain conveyors HHC. 2020. <http://minerals.hazemag-group.com/en/products/screening-conveying/chain-conveyor%0As-hhc/>.
- [158] Molnár V, Fedorko G, Andrejčová M, Grinčová A, Tomašková M. Analysis of influence of conveyor belt overhang and cranking on pipe conveyor operational characteristics. *Measurement* 2015;63:168–75. <https://doi.org/10.1016/j.measurement.2014.12.013>.
- [159] Beumer Group. Pipe conveyor. 2020. <https://www.beumergroup.com/i/pipe-conveyor-15220/>.
- [160] Bombardier. Bombardier rail vehicles production site-bruges. 2021. <http://www.bombardier.com/en/country.belgium.html>.
- [161] Corporation SC. Catalog and engineering manual. 2010.
- [162] Manufacturing CE&. Standard screw conveyors. 2019. <https://www.conveyoreng.com/standard-screw-conveyors/>.
- [163] Continental Conveyor & Machine Works Ltd. Screw conveyor catalogue and engineering manual. 2010.
- [164] Thomas Conveyor Company. High Temperature Screw Conveyors n.d. <http://cmtnc.com/html/screw-conveyor-systems.html>.
- [165] Gamberotta - Gschwendt. Bulk solids mechanical handling. 2016.
- [166] S. Howes. Screw conveyors n.d. https://showes.com/equipment_category/screw-conveyors/ (accessed April 21, 2021).
- [167] Bernd Munstermann GmbH & Co. KG. Conveying Technology, Material Handling Systems and Special Machines. n.d.
- [168] Perry. Perry's chemical engineers' handbook. Choice Rev Online 1998;35. <https://doi.org/10.5860/CHOICE.35-3079>. 35-3079-35-3079.
- [169] Beumer Technology. Beumer materials handling: economical transport of bulk goods-Belt conveyor product range. Germany: n.d.
- [170] AUMUND. Conveying and cooling in the iron and steel industry. 2019.
- [171] Metso Minerals. Conveyor Belt Product Range n.d. <https://www.mogroup.com/products-and-services/parts/conveyor-parts/conveyor-belts/>.
- [172] Lauyans & Company. High Temperature Conveyor n.d.:1. <http://www.lauyans.com/custom-conveyors/custom-conveyor/high-temperature-conveyor/>.
- [173] Repole KKD, Jeter SM. Design and analysis of a high temperature particulate hoist for proposed particle heating concentrator solar power systems. In: Vol 1 Biofuels, Hydrog Syngas, Altern Fuels; CHP Hybrid Power Energy Syst Conc Sol Power; Energy Storage; Environ Econ Policy Considerations Adv Energy Syst Geothermal, Ocean Emerg E. American Society of Mechanical Engineers; 2016. <https://doi.org/10.1115/ES2016-59619>.
- [174] Koepe and Partners. Patentanwalt. 2005. <http://innovopat.de/eng/index.php>.
- [175] Guo P, Ly QH, Saw WL, Lim K-S, Ashman PJ, Nathan GJ. A technical assessment of pneumatic conveying of solids for a high temperature particle receiver. 2019, 030025. <https://doi.org/10.1063/1.5117537>.
- [176] Cheng Z, Guo Z, Tan Z, Yang J, Wang Q. Waste heat recovery from high-temperature solid granular materials: energy challenges and opportunities. *Renew Sustain Energy Rev* 2019;116:109428. <https://doi.org/10.1016/j.rser.2019.109428>.
- [177] Baumann T, Schmitz S, Dabrowski J, Zunft S, Göttsche J, Hoffschmidt B, et al. Properties of bulk materials for high-temperature air-sand heat exchangers. In:

- Proc ISES Sol World Congr 2011. International Solar Energy Society; 2011. p. 1–9. <https://doi.org/10.18086/swc.2011.09.01>.
- [178] Baumann T, Zunft S. Theoretical and experimental investigation of a moving bed heat exchanger for solar central receiver power plants. *J Phys Conf Ser* 2012;395: 012055. <https://doi.org/10.1088/1742-6596/395/1/012055>.
- [179] Baumann T, Zunft S, Tamme R. Moving bed heat exchangers for use with heat storage in concentrating solar plants: a multiphase model. *Heat Transf Eng* 2014; 35:224–31. <https://doi.org/10.1080/01457632.2013.825154>.
- [180] Baumann T, Zunft S. Development and performance assessment of a moving bed heat exchanger for solar central receiver power plants. *Energy Procedia* 2015;69: 748–57. <https://doi.org/10.1016/j.egypro.2015.03.085>.
- [181] Albrecht KJ, Ho CK. Heat transfer models of moving packed-bed particle-to-sCO₂ heat exchangers. *J Sol Energy Eng* 2019;141. <https://doi.org/10.1115/1.4041546>.
- [182] Albrecht KJ, Ho CK. Design and operating considerations for a shell-and-plate, moving packed-bed, particle-to-sCO₂ heat exchanger. *Sol Energy* 2019;178: 331–40. <https://doi.org/10.1016/j.solener.2018.11.065>.
- [183] Fernández-Torrijos M, Albrecht KJ, Ho CK. Dynamic modeling of a particle/supercritical CO₂ heat exchanger for transient analysis and control. *Appl Energy* 2018;226:595–606. <https://doi.org/10.1016/j.apenergy.2018.06.016>.
- [184] Ho CK, Carlson M, Albrecht KJ, Ma Z, Jeter S, Nguyen CM. Evaluation of alternative designs for a high temperature particle-to-sCO₂ heat exchanger. *J Sol Energy Eng* 2019;141. <https://doi.org/10.1115/1.4042225>.
- [185] Albrecht KJ, Carlson MD, Ho CK. Integration, control, and testing of a high-temperature particle-to-sCO₂ heat exchanger. 2019, 030001. <https://doi.org/10.1063/1.5117513>.
- [186] Moawed MA, Berbish NS, Allam AA, El-Shamy AR, El-Shazly KM. Heat transfer between fluidized bed and horizontal bundle of tubes in a vertical channel. *Int J Chem React Eng* 2010;8. <https://doi.org/10.2202/1542-6580.2123>.
- [187] Botterill JSM, Teoman Y, Yüregir KR. Factors affecting heat transfer between gas-fluidized beds and immersed surfaces. *Powder Technol* 1984;39:177–89. [https://doi.org/10.1016/0032-5910\(84\)85035-4](https://doi.org/10.1016/0032-5910(84)85035-4).
- [188] Martyushin IG, Varyagin IA. *Fluid-bed heat transfer*. London, UK: Academic Press; 1975.
- [189] Stenberg V, Sköldbberg V, Öhrby L, Rydén M. Evaluation of bed-to-tube surface heat transfer coefficient for a horizontal tube in bubbling fluidized bed at high temperature. *Powder Technol* 2019;352:488–500. <https://doi.org/10.1016/j.powtec.2019.04.073>.
- [190] Kim SW, Ahn JY, Kim SD, Hyun Lee D. Heat transfer and bubble characteristics in a fluidized bed with immersed horizontal tube bundle. *Int J Heat Mass Transf* 2003;46:399–409. [https://doi.org/10.1016/S0017-9310\(02\)00296-X](https://doi.org/10.1016/S0017-9310(02)00296-X).
- [191] Schwaiger K, Haider M, Hämmerle M, Wünsch D, Obermaier M, Beck M, et al. sandTES – an active thermal energy storage system based on the fluidization of powders. *Energy Procedia* 2014;49:983–92. <https://doi.org/10.1016/j.egypro.2014.03.106>.
- [192] Ma Z, Mehos M, Glatzmaier G, Sakadjian BB. Development of a concentrating solar power system using fluidized-bed technology for thermal energy conversion and solid particles for thermal energy storage. *Energy Procedia* 2015;69:1349–59. <https://doi.org/10.1016/j.egypro.2015.03.136>.
- [193] Gomez-Garcia F, Gauthier D, Flamant G. Design and performance of a multistage fluidized bed heat exchanger for particle-receiver solar power plants with storage. *Appl Energy* 2017;190:510–23. <https://doi.org/10.1016/j.apenergy.2016.12.140>.
- [194] Li S, Kong W, Zhang H, Sabatier F, Ansart R, Flamant G, et al. The fluidized bed air heat exchanger in a hybrid Brayton-cycle solar power plant. 2019, 140002. <https://doi.org/10.1063/1.5117650>.
- [195] Kuni D, Levenspiel O. *Fluidization engineering*. Elsevier; 1991. <https://doi.org/10.1016/B978-0-08-050664-7.50003-2>.
- [196] Sakadjian B, Hu S, Maryamchik M, Flynn T, Santelmann K, Ma Z. Fluidized-bed technology enabling the integration of high temperature solar receiver CSP systems with steam and advanced power cycles. *Energy Procedia* 2015;69: 1404–11. <https://doi.org/10.1016/j.egypro.2015.03.126>.
- [197] Peters MS, Timmerhaus KD, West RE. *Plant design and economics for chemical engineers*. New York: McGraw-Hill; 2003. vol. 4.
- [198] Brun K, Friedman P. Fundamentals and applications of supercritical carbon dioxide (sCO₂) based power cycles. *Fundam. appl. supercrit. carbon dioxide based power cycles*. Elsevier; 2017. p. 1–22. <https://doi.org/10.1016/B978-0-08-100804-1.00001-3>.
- [199] Saravanamuttoo HIH, Rogers GFC, Cohen H. *Gas turbine theory*. Pearson Education; 2001.
- [200] Shackelford JF, Han Y-H, Kim S, Kwon S-H. *CRC materials science and engineering handbook*. CRC Press; 2016.
- [201] Sloss L. *Technology readiness of advanced coal-based power generation systems*, CCC/292. 2019. ISBN 978-92-9029-615-7.
- [202] Zhang D. *Ultra-supercritical coal power plants Materials, technologies and optimization*. 2013.
- [203] Nicol K. *Status of advanced ultra-supercritical pulverized coal technology*, ISBN 978-92-9029-549-5. 2013.
- [204] Tanuma T. *Advances in steam turbines for modern power plants*. Woodhead Publishing; 2016.
- [205] Weiland N, Shelton W. *Systems analyses of direct power extraction (DPE) and advanced ultra-supercritical (AUSC) power plants, crosscutting research & rare earth elements portfolios review*. 2016. Pittsburgh, PA.
- [206] Nair A, Kumanan S. *Newer materials for supercritical power plant components—a manufacturability study*. In: *Proc Int Conf Adv Prod Ind Eng*; 2015. p. 326.
- [207] Kerouille M. *GE Steam power product catalog*. 2019. US.
- [208] Achter T, Quinkert R, Baca M. *Increased efficiency and flexibility of large coal-fired power plants applied to 350-MW-class units*. 2016. Germany.
- [209] Pacheco J, Wolf T, Muley N. *Incorporating supercritical steam turbines into advanced molten-salt power tower plants: feasibility and performance*. 2013.
- [210] Spencer RC, Cotton KC, Cannon CN. A method for predicting the performance of steam turbine-generators....: 16,500 kw and larger. *J Eng Power* 1963;85:249–98. <https://doi.org/10.1115/1.3677341>.
- [211] Gonzalez-Salazar MA, Kirsten T, Prchlik L. Review of the operational flexibility and emissions of gas- and coal-fired power plants in a future with growing renewables. *Renew Sustain Energy Rev* 2018;82:1497–513. <https://doi.org/10.1016/j.rser.2017.05.278>.
- [212] Henderson C. *Increasing the flexibility of coal-fired power plants*. 2014.
- [213] Stefano B. D1.2 – Report on flexibility constraints, load scenarios definition. 2018.
- [214] Price H. *The future of CSP: dispatchable solar power*. 2018.
- [215] Purgert R, Hack H. *Materials for advanced ultrasupercritical steam turbines - advanced ultra-supercritical component demonstration*. 2019.
- [216] Shibli A. *Coal power plant materials and life assessment*. Woodhead Publishing; 2014. <https://doi.org/10.1016/C2013-0-16254-X>.
- [217] 2020 Performance Specs. *Gas turbine world*. 36th Ed. Fairfield, CT (USA): Pequot Publishing; 2020.
- [218] Siros F, Fernández Campos G. Optimisation of a low-TIT combined cycle gas turbine with application to new generation solar thermal power plants. In: *Vol 3 Coal, Biomass Altern Fuels; Cycle Innov Electr Power; Ind Cogener Appl Org Rank Cycle Power Syst*. American Society of Mechanical Engineers; 2017. <https://doi.org/10.1115/GT2017-65227>.
- [219] Barigozzi G, Bonetti G, Franchini G, Perdichizzi A, Ravelli S. Thermal performance prediction of a solar hybrid gas turbine. *Sol Energy* 2012;86: 2116–27. <https://doi.org/10.1016/j.solener.2012.04.014>.
- [220] Sánchez-Ortiz S, Medina A, Calvo Hernández A. *Recuperative solar-driven multi-step gas turbine power plants*. *Energy Convers Manag* 2013;67:171–8. <https://doi.org/10.1016/j.enconman.2012.11.006>.
- [221] Andreades C, Dempsey L, Peterson PF. Reheat air-brayton combined cycle power conversion off-nominal and transient performance. *J Eng Gas Turbines Power* 2014;136. <https://doi.org/10.1115/1.4026612>.
- [222] Andreades C, Scarlat RO, Dempsey L, Peterson P. Reheat-air Brayton combined cycle power conversion design and performance under nominal ambient conditions. *J Eng Gas Turbines Power* 2014;136. <https://doi.org/10.1115/1.4026506>.
- [223] Al-attab KA, Zainal ZA. Externally fired gas turbine technology: a review. *Appl Energy* 2015;138:474–87. <https://doi.org/10.1016/j.apenergy.2014.10.049>.
- [224] Al-attab KA, Zainal ZA. Performance of high-temperature heat exchangers in biomass fuel powered externally fired gas turbine systems. *Renew Energy* 2010; 35:913–20. <https://doi.org/10.1016/j.renene.2009.11.038>.
- [225] Zaversky F, Les I, Sorbet P, Sánchez M, Valentin B, Brau J-F, et al. The challenge of solar powered combined cycles – providing dispatchability and increasing efficiency by integrating the open volumetric air receiver technology. *Energy* 2020;194:116796. <https://doi.org/10.1016/j.energy.2019.116796>.
- [226] Zaversky F, Les I, Sánchez M, Valentin B, Brau J-F, Siros F, et al. Techno-economic optimization and benchmarking of a solar-only powered combined cycle with high-temperature TES upstream the gas turbine. *Green energy environ. IntechOpen*; 2020. <https://doi.org/10.5772/intechopen.90410>.
- [227] Alobaid F, Pfeiffer S, Epple B, Seon C-Y, Kim H-G. Fast start-up analyses for Benson heat recovery steam generator. *Energy* 2012;46:295–309. <https://doi.org/10.1016/j.energy.2012.08.020>.
- [228] ALSTOM. *GT24/GT26 gas turbine*. 2021.
- [229] Angelino G. Carbon dioxide condensation cycles for power production. *J Eng Power* 1968;90:287–95. <https://doi.org/10.1115/1.3609190>.
- [230] Feher EG. The supercritical thermodynamic power cycle. *Energy Convers* 1968;8: 85–90. [https://doi.org/10.1016/0013-7480\(68\)90105-8](https://doi.org/10.1016/0013-7480(68)90105-8).
- [231] Dostal V, Driscoll MJ, Hejzlar P. *A super critical carbon dioxide cycle for next generation nuclear reactors*. Massachusetts Institute of Technology; 2004.
- [232] Ahn Y, Bae SJ, Kim M, Cho SK, Baik S, Lee JI, et al. Review of supercritical CO₂ power cycle technology and current status of research and development. *Nucl Eng Technol* 2015;47:647–61. <https://doi.org/10.1016/j.net.2015.06.009>.
- [233] Crespi F, Gavagnin G, Sánchez D, Martínez GS. Supercritical carbon dioxide cycles for power generation: a review. *Appl Energy* 2017;195:152–83. <https://doi.org/10.1016/j.apenergy.2017.02.048>.
- [234] Yin J, Zheng Q, Peng Z, Zhang X. Review of supercritical CO₂ power cycles integrated with CSP. *Int J Energy Res* 2020;44:1337–69. <https://doi.org/10.1002/er.4909>.
- [235] Neises T, Turchi C. A comparison of supercritical carbon dioxide power cycle configurations with an emphasis on CSP applications. *Energy Procedia* 2014;49: 1187–96. <https://doi.org/10.1016/j.egypro.2014.03.128>.
- [236] Neises T, Turchi C. Supercritical carbon dioxide power cycle design and configuration optimization to minimize leveled cost of energy of molten salt power towers operating at 650°C. *Sol Energy* 2019;181:27–36. <https://doi.org/10.1016/j.solener.2019.01.078>.
- [237] Binotti M, Astolfi M, Campanari S, Manzolini G, Silva P. Preliminary assessment of sCO₂ cycles for power generation in CSP solar tower plants. *Appl Energy* 2017; 204:1007–17. <https://doi.org/10.1016/j.apenergy.2017.07.001>.
- [238] Mecheri M, Le Moullec Y. Supercritical CO₂ Brayton cycles for coal-fired power plants. *Energy* 2016;103:758–71. <https://doi.org/10.1016/j.energy.2016.02.111>.
- [239] Carlson MD. *Progress toward commercial deployment of sCO₂ Brayton power cycles*. 2019.
- [240] Marion J, Kutin M, McClung A, Mortzheim J, Ames R. The step 10 MWe sCO₂ pilot plant demonstration. vol. 9 oil gas appl. supercrit. CO₂ Power Cycles; Wind

- Energy, American Society of Mechanical Engineers; 2019. <https://doi.org/10.1115/GT2019-91917>.
- [241] White MT, Bianchi G, Chai L, Tassou SA, Sayma AI. Review of supercritical CO2 technologies and systems for power generation. *Appl Therm Eng* 2021;185:116447. <https://doi.org/10.1016/j.applthermaleng.2020.116447>.
- [242] Sánchez D, Prieto C, López-Román A, Sánchez T, Aguilar FJJ-E, Blanco AM, et al. Report on Best Available Technologies (BAT) for central receiver systems. 2019.
- [243] Suzuki S, Iwai Y, Itoh M, Morisawa Y, Jain P, Kobayashi Y. High pressure combustion test of gas turbine combustor for 50MWth supercritical CO2 demonstration power plant on Allam cycle. In: *Proc Int Gas Turbine Cong*; 2019.
- [244] Held TJ. Initial test results of a megawatt-class supercritical CO2 heat engine. In: *4th Int Symp CO2 Power Cycles*; 2014. p. 9–10.
- [245] Allison TC, Jeffrey Moore J, Hofer D, Towler MD, Thorp J. Planning for successful transients and trips in a 1 MWe-scale high-temperature sCO2 test loop. *J Eng Gas Turbines Power* 2019;141. <https://doi.org/10.1115/1.4041921>.
- [246] Moore J, Cich S, Day M, Allison T, Wade J, Hofer D. Commissioning of a 1 MWe supercritical CO2 test loop. In: *6th Int Supercrit CO2 Power Cycles Symp*; 2018.
- [247] Walker M, Fleming DD, Pasch JJ. Gas foil bearing coating behavior in environments relevant to S-CO2 power system turbomachinery. Albuquerque, NM (United States): Sandia National Lab.(SNL-NM); 2018.
- [248] Rapp LM. Experimental testing of a 1MW sCO2 turbocompressor. Albuquerque, NM (United States): Sandia National Lab.(SNL-NM); 2019.
- [249] Clementoni EM, Cox TL, King MA. Off-nominal component performance in a supercritical carbon dioxide Brayton cycle. *J Eng Gas Turbines Power* 2016;138. <https://doi.org/10.1115/1.4031182>.
- [250] Cha JE, Bae SW, Lee J, Cho SK, Lee J, Park JH. Operation results of a closed supercritical CO2 simple Brayton cycle. In: *Proc 5th Int Symp CO2 Power Cycles*; 2016. p. 28–31.
- [251] Luu MT, Milani D, McNaughton R, Abbas A. Analysis for flexible operation of supercritical CO2 Brayton cycle integrated with solar thermal systems. *Energy* 2017;124:752–71. <https://doi.org/10.1016/j.energy.2017.02.040>.
- [252] Alfani D, Astolfi M, Binotti M, Campanari S, Casella F, Silva P. Multi objective optimization of flexible supercritical CO2 coal-fired power plants. In: *Vol 3 Coal, Biomass, Hydrog Altern Fuels; Cycle Innov Electr Power; Ind Cogener Org Rank Cycle Power Syst*. American Society of Mechanical Engineers; 2019. <https://doi.org/10.1115/GT2019-91789>.
- [253] Dyreby JJ, Klein SA, Nellis GF, Reindl DT. Modeling off-design and part-load performance of supercritical carbon dioxide power cycles. In: *ASME turbo expo 2013 turbine Tech Conf Expo*. American Society of Mechanical Engineers Digital Collection; 2013.
- [254] Marchionni M, Bianchi G, Tassou SA. Transient analysis and control of a heat to power conversion unit based on a simple regenerative supercritical CO2 Joule-Brayton cycle. *Appl Therm Eng* 2021;183:116214.
- [255] Osorio JD, Hovsopian R, Ordóñez JC. Dynamic analysis of concentrated solar supercritical CO2-based power generation closed-loop cycle. *Appl Therm Eng* 2016;93:920–34.
- [256] Singh R, Miller SA, Rowlands AS, Jacobs PA. Dynamic characteristics of a direct-heated supercritical carbon-dioxide Brayton cycle in a solar thermal power plant. *Energy* 2013;50:194–204.
- [257] Luu MT, Milani D, McNaughton R, Abbas A. Dynamic modelling and start-up operation of a solar-assisted recompression supercritical CO2 Brayton power cycle. *Appl Energy* 2017;199:247–63. <https://doi.org/10.1016/j.apenergy.2017.04.073>.
- [258] European Union's Horizon 2020 research and innovation program. sCO2-Flex, under grant agreement N° 764690. 2021. <https://www.sco2-flex.eu/>.
- [259] Cagnac A, Mecheri M, Bedogni S. Configuration of a flexible and efficient sCO2 cycle for fossil power plant. In: *3rd Eur Conf Supercrit CO2 Power Syst 2019 19th-20th Sept 2019*; 2019. p. 271–80.
- [260] Ho CK, Carlson M, Garg P, Kumar P. Cost and performance tradeoffs of alternative solar-driven S-CO2 Brayton cycle configurations. In: *ASME 2015 9th Int Conf Energy Sustain collocated with ASME 2015 Power Conf ASME 2015 13th Int Conf Fuel Cell Sci Eng Technol ASME 2015 Nucl Forum*. American Society of Mechanical Engineers Digital Collection; 2015.
- [261] Fleming D, Krüzenga A. Identified corrosion and erosion mechanisms in sCO2 Brayton cycles. 2014. SAND2014-15546.
- [262] Wagner MJ, Wendelin T. SolarPILOT: a power tower solar field layout and characterization tool. *Sol Energy* 2018;171:185–96.
- [263] Kim J-S, Kumar A, Gardner W, Lipiński W. Numerical and experimental investigation of a novel multi-stage falling particle receiver. 2019, 030030. <https://doi.org/10.1063/1.5117542>.
- [264] Gobereit B, Amsbeck L, Buck R, Pitz-Paal R, Röger M, Müller-Steinhagen H. Assessment of a falling solid particle receiver with numerical simulation. *Sol Energy* 2015;115:505–17. <https://doi.org/10.1016/j.solener.2015.03.013>.
- [265] Ho CK, Pattyn CA. Investigating environmental impacts of particle emissions from a high-temperature falling particle receiver. 2020, 030019. <https://doi.org/10.1063/5.0029219>.
- [266] Buck R, Giuliano S. Solar tower system temperature range optimization for reduced LCOE. 2019, 030010. <https://doi.org/10.1063/1.5117522>.
- [267] Gueguen R, Grange B, Bataille F, Mer S, Flamant G. Shaping high efficiency, high temperature cavity tubular solar central receivers. *Energies* 2020;13:4803. <https://doi.org/10.3390/en13184803>.
- [268] Behar O, Grange B, Flamant G. Design and performance of a modular combined cycle solar power plant using the fluidized particle solar receiver technology. *Energy Convers Manag* 2020;220:113108. <https://doi.org/10.1016/j.enconman.2020.113108>.
- [269] Chen R, Romero M, González-Aguilar J, Rovense F, Rao Z, Liao S. Optical and thermal integration analysis of supercritical CO2 Brayton cycles with a particle-based solar thermal plant based on annual performance. *SSRN Electron J* 2021. <https://doi.org/10.2139/ssrn.3919711>.
- [270] Rovense F, Reyes-Belmonte MÁ, Romero M, González-Aguilar J. Thermo-economic analysis of a particle-based multi-tower solar power plant using unfired combined cycle for evening peak power generation. *Energy* 2022;240:122798. <https://doi.org/10.1016/j.energy.2021.122798>.
- [271] Albrecht KJ, Bauer ML, Ho CK. Parametric analysis of particle CSP system performance and cost to intrinsic particle properties and operating conditions. In: *ASME 2019 13th Int Conf Energy Sustain*. American Society of Mechanical Engineers; 2019. <https://doi.org/10.1115/ES2019-3893>.
- [272] NREL. Annual technology baseline-atb electricity data overview 2020. <https://atb.nrel.gov/electricity/2020/index.php?t=in>.
- [273] California Independent System Operator. Fast facts - what the Duck curve tells us about managing a green grid. 2016. 250 Outcropping Way, Folsom, CA 95630.
- [274] Burtin A, Silva V. Technical and economic analysis of the European electricity system with 60% RES. 2015. EDF.
- [275] U.S. Energy Information Administration. Capital cost and performance characteristic estimates for utility scale electric power generating technologies. 2020. Washington, DC 20585.
- [276] U.S. Department of Energy's Office of Energy Efficiency and Renewable Energy. Concentrating solar power could provide the flexibility and reliability the U.S. electric grid needs. 2017.
- [277] Brack D. The impacts of the demand for woody biomass for power and heat on climate and forests. 2017.
- [278] Argyrou MC, Christodoulides P, Kalogirou SA. Energy storage for electricity generation and related processes: technologies appraisal and grid scale applications. *Renew Sustain Energy Rev* 2018;94:804–21. <https://doi.org/10.1016/j.rser.2018.06.044>.
- [279] Morgan R, Nelmes S, Gibson E, Brett G. An analysis of a large-scale liquid air energy storage system. *Proc Inst Civ Eng* 2015;168:135–44. <https://doi.org/10.1680/ener.14.00038>.
- [280] Smallbone A, Jülich V, Wardle R, Roskilly AP. Levelised Cost of Storage for Pumped Heat Energy Storage in comparison with other energy storage technologies. *Energy Convers Manag* 2017;152:221–8. <https://doi.org/10.1016/j.enconman.2017.09.047>.
- [281] Fan X, Liu B, Liu J, Ding J, Han X, Deng Y, et al. Battery technologies for grid-level large-scale electrical energy storage. *Trans Tianjin Univ* 2020;26:92–103. <https://doi.org/10.1007/s12209-019-00231-w>.
- [282] Cole W, Frazier AW. Cost projections for utility-scale battery storage. 2019.
- [283] Fu R, Remo T, Margolis R. 2018 U.S. Utility-scale photovoltaics-plus-energy storage system costs benchmark. 2018.
- [284] Dieckmann S, Dersch J, Giuliano S, Puppe M, Lüpfer E, Hennecke K, et al. LCOE reduction potential of parabolic trough and solar tower CSP technology until 2025. 2017, 160004. <https://doi.org/10.1063/1.4984538>.
- [285] Renewable IRENA. Power generation costs in 2019. Abu Dhabi: International Renewable Energy Agency; 2020.
- [286] Nathan GJ, Jafarian M, Dally BB, Saw WL, Ashman PJ, Hu E, et al. Solar thermal hybrids for combustion power plant: a growing opportunity. *Prog Energy Combust Sci* 2018;64:4–28. <https://doi.org/10.1016/j.pecs.2017.08.002>.
- [287] Baeyens J, Li S, Zhang H, Dewil R, Flamant G, Ansart R, et al. Bio-energy carriers as back-up fuel in hybrid solar power plants. (IOP) *Conf Ser Earth Environ Sci* 2020;544:12012. <https://doi.org/10.1088/1755-1315/544/1/012012>.
- [288] Peterseim JH, Hellwig U, Tadros A, White S. Hybridisation optimization of concentrating solar thermal and biomass power generation facilities. *Sol Energy* 2014;99:203–14. <https://doi.org/10.1016/j.solener.2013.10.041>.
- [289] Coelho B, Schwarzbözl P, Oliveira A, Mendes A. Biomass and central receiver system (CRS) hybridization: Volumetric air CRS and integration of a biomass waste direct burning boiler on steam cycle. *Sol Energy* 2012;86:2912–22. <https://doi.org/10.1016/j.solener.2012.06.009>.
- [290] Coelho B, Oliveira A, Schwarzbözl P, Mendes A. Biomass and central receiver system (CRS) hybridization: Integration of syngas/biogas on the atmospheric air volumetric CRS heat recovery steam generator duct burner. *Renew Energy* 2015;75:665–74. <https://doi.org/10.1016/j.renene.2014.10.054>.
- [291] Siemens. Siemens to supply solar field for hybrid CSP plant in Catalonia, Spain. 2011. https://www.siemens.com/press/en/pressrelease/2011/renewable_energy/ere201109107.htm (accessed December 31, 2021).
- [292] Gobin A, Neau H, Simonin O, Llinas J-R, Reiling V, Sélo J-L. Fluid dynamic numerical simulation of a gas phase polymerization reactor. *Int J Numer Methods Fluids* 2003;43:1199–220. <https://doi.org/10.1002/fld.542>.
- [293] Zhang H, Degreve J, Baeyens J, Wu SY. Powder attrition in gas fluidized beds. *Powder Technol* 2016. <https://doi.org/10.1016/j.powtec.2015.08.052>.
- [294] Fayed M, Otten L. CEMA factors. *Handb. powder sci. technol.* 2013:445–50.
- [295] Vandewalle C, Baeyens J, Degreve J. Attrition and wear in powder circulation loops. *Powder Handl Process* 2001;13:77–81.
- [296] Keck T, Balz M, Göcke V, von Reeken F, Gross F, Landman W, et al. Hami – the first Stello solar field. 2019, 030029. <https://doi.org/10.1063/1.5117541>.
- [297] Turchi CS, Boyd M, Kesseli D, Kurup P, Mehos MS, Neises TW, et al. CSP Systems analysis - final project report. 2019. <https://doi.org/10.2172/1513197>. Golden, CO (United States).
- [298] Steel Tubes India n.d.

- [299] Benitez J. *Process engineering and design for air pollution control*. 1993. vol. 8. Prentice Hall Englewood Cliffs, NJ.
- [300] Turchi CS, Heath GA. *Molten salt power tower cost model for the system advisor model (SAM)* 2013.
- [301] IRENE. *Renewable power generation costs in 2014*. 2015.

Gilles Flamant

Gilles Flamant graduated as Chemical Engineer (Paris) and PhD in Process Engineering (Toulouse). He has been working in the field of concentrated solar energy and high temperature processes for about 45 years. He lectures at the University of Perpignan and the Mohammed V University, Rabat (Morocco) on concentrated solar power, radiation heat transfer, fluidization and solar fuels. He is currently Emeritus Senior Scientist at CNRS. He was Director of the PROMES-CNRS Laboratory (150 persons) between 2004 and 2016. He was Principal Investigator of the French Laboratory of Excellence in solar energy "SOLSTICE" (2012–2019) and of the National Infrastructure of Excellence in concentrated solar technologies "SOCRATE" (2011–2021). He coordinated 3 research projects on the application of fluidized beds in concentrated solar energy conversion (CSP2-FP7, SOLPART-H2020, Next-CSP-H2020). He is currently Chair of SolarPACES.

Benjamin Grange

Benjamin Grange studied Process and Chemical Engineering (ENSIC, Nancy, France). He obtained his Ph.D. at the University of Perpignan via Domitia in 2012. After a 2-year postdoc in PROMES-CNRS, he became project leader in the Masdar Institute of the United Arab Emirates working on a new concept of a molten salt receiver. In January 2017, he rejoined PROMES-CNRS as research coordinator for the European Next-CSP project aiming at demonstrating the fluidized particle-in-tube solar receiver concept at pilot scale.

John Wheeldon

John Wheeldon obtained a B Tech. and M Sc. in chemical engineering from the University of Bradford (U.K) and has worked for the National Coal Board and the International Energy Agency in the UK. During a career at the Electric Power Research Institute in Palo Alto (USA), he has played a prominent role in several coal-based pilot and demonstration projects, where he developed expertise in hot gas filtration, solids handling and conveying, heat transfer, power plant technology, and steam cycles.

Frédéric Siros

Frédéric Siros graduated in 1983 from Ecole Nationale Supérieure de l'Aéronautique et de l'Espace. Since then, he has been employed by EDF in the Thermal Engineering Department and subsequently in the R&D Division. After a supervisory period of commissioning and acceptance tests on site for various combined cycle power plants, he turned to power plant design, and focused mainly on plant optimization during the early stages of their design. He then moved from engineering to R&D activities. Since 2009, he has been working mainly on Concentrated Solar Power and innovative power cycles. His main activities involve technological and due diligence tasks on CSP technology providers for upcoming industrial projects as well as participating in European H2020 projects including Next-CSP.

Benoît Valentin

Benoît Valentin graduated in 2013 from Mines ParisTech (energy and nuclear engineering), and obtained a second master's degree in oil processing from IFP School. He then joined the department of Fluid Mechanics, Power Generation & Environment of EDF R&D in 2015. He has been working on the design and techno-economic assessment of various processes, including carbon capture, effluent processing for the nuclear industry as well as thermodynamic cycles for solar and fossil-fueled applications. He has supported the technical coordination of the H2020 project sCO₂-Flex (Supercritical CO₂ cycle for

FLEXible and sustainable support to the electricity system) since 2019, and is a technical contributor in the H2020 projects CAPTure and Next-CSP.

Françoise Bataille

Françoise Bataille graduated as Physical and Chemical Engineer (Ecole Normale Supérieure de Lyon - France) and as PhD in Fluid Mechanics. After having worked for NASA and different universities in the USA, she became Professor in fluid mechanics and heat transfer (National Institute of Applied Sciences, then University of Perpignan - France), where she also occupied positions as Vice-President for research and Chair of the graduate college on science and technology. She is a former Deputy Director both of PROMES-CNRS Laboratory and of the French Research Federation on Solar Energy (FEDESOL, 25 laboratories). She was Vice-President of the French Thermal Society (SFT). She became Vice-President of the French Mechanical Association (AFM), and is since 2020 Director of the French Laboratory of Excellence in Solar Energy "SOLSTICE". She has for 10 years been a member of the French National Council of Universities (CNU) in charge of energetics and process engineering, and is a science delegate to the French National Quality Assurance Agency (HCERES) for engineering sciences.

Zhang Huili

Huili Zhang obtained her Bachelor and Master degree at Beijing University of Chemical Technology, and her Doctoral degree within the research team of Prof. Degève and Prof. Baeyens at University of Leuven (Belgium) in 2016. She is associated professor at Beijing University of Chemical Technology, Beijing China. Her research interests are solar thermal applications, including solar drying, solar-driven chemical reactions, fluidized bed solar reactor design, and biomass conversions. Currently, she supervises research of 2 PhD students and 4 Master students working on solar gasification of biomass, solar thermal water splitting, and the development of a horizontal fluidized bed solar receiver for solar energy capture and applications under funding of the University and Ministry of Science and Technology of China.

Yimin Deng

Yimin Deng studied Chemical Engineering at the Beijing University of Chemical Technology (BUCT, China), where she also performed a one-year research assistance for pilot-scale developments in the field of solar energy capture technology within the Beijing Advanced Innovation center of Soft Matter Science and Engineering. She thereafter obtained her Master degree Master in Fluids Engineering for Industrial Processes at the Institut National des Sciences Appliquées Toulouse (INSA-Toulouse).

In 2020, she joined the PhD research group of Prof. Dewil and Prof. Baeyens at the KU Leuven, for research on concentrated solar energy applications at lab- and pilot scale level. She participated in international conferences and published several papers in peer-reviewed journals of high impact factor.

Jan Baeyens

Jan Baeyens studied Nuclear (Brussels) and Chemical Engineering (Leuven). He obtained his Ph.D. at the University of Bradford-U.K. After 13 years of employment in engineering divisions of various Belgian companies, he became a part-time professor at the Universities of Leuven and Antwerp (BE), and worked as a process and project consultant in Europe and overseas as managing director of European Powder and Process Technology (EPPT), mostly in the fields of powder technology and renewable energy. EPPT was a partner in European research projects (FP7, and H2020). After academic appointments at the University of Birmingham, the University College London and the University of Warwick, he was appointed Principal Investigator at the Beijing University of Chemical Technology and is actively involved in renewable energy research.

He was a 5 times successive nominee of the "Clarivate Top 1% cited researcher".